Ultra-broadband Silicon Waveguides for Terahertz Applications

RATMALGRE ALEX SYLVESTERE DESIRE KOALA

MARCH 2023

Ultra-broadband Silicon Waveguides for Terahertz Applications

A dissertation submitted to

THE GRADUATE SCHOOL OF ENGINEERING SCIENCE

OSAKA UNIVERSITY

In partial fulfillment of the requirements for the degree of

DOCTOR OF PHILOSOPHY IN ENGINEERING

BY

RATMALGRE ALEX SYLVESTERE DESIRE KOALA

MARCH 2023

Abstract

A lot of research effort has been dedicated to the terahertz (THz) range covering frequencies from 0.1 to 10 THz. This is because of the huge available spectral bandwidth that should enable high communication channel capacities. It can be conceivable to bring to daily use various applications for up to 1 Tbit/s in wireless communications links, hidden object detection, and space exploration. These applications are needed for the development of emerging applications and services including virtual immersive experiences, high computational data centers, and advanced connectivity for faster real-time streaming services and more coverage worldwide. For nascent technologies to become commonplace in our daily lives, THz range wave-guiding interconnects are indispensable. Low-loss and broadband silicon (Si) waveguides have reported loss < 0.1 dB/cm and bandwidth of ~ 120 GHz in 0.26 THz – 0.39 THz. The bandwidth can further be enhanced to unlock high-data rates applications. In addition, there is an ever-growing need for short-range low-loss interconnects for inter-/intra-chip/board communication applications.

This dissertation focuses on the development of low-loss Si waveguide platforms that will serve as a canvas for the demonstration of THz imaging and communications. This study explores in detail the development of extremely low-loss and broadband Si waveguides in the WR-1 band (0.75 – 1.1 THz) to target higher frequencies. Previous work has focused on frequencies up to 0.75 THz. Extremely broadband dielectric all-Si waveguides are designed, fabricated, and tested. The performance of two waveguide designs, including effective-medium (EM) waveguides, and unclad waveguides were analyzed. These waveguides have a record-setting 3-dB bandwidth of 350 GHz. The propagation loss is as low as < 0.1 dB/cm and 0.15 dB/cm for EM waveguide and unclad waveguide, respectively.

In addition, fundamental design practices and measurement techniques that can be extended to the design and analysis of dielectric waveguides at high frequencies > 1 THz are established. Compact and packaged waveguide modules are designed and tested, revealing a loss improvement of 8 dB (EM waveguide) and 6 dB (unclad waveguide) compared to the metallic hollow waveguide. The results advocate that all-Si waveguide modules can replace

metallic waveguides for interconnecting with the test equipment. Subsequently, using the waveguide module, THz imaging with a high resolution of 0.28 mm is demonstrated.

All-Si waveguides are employed to double the data rates by implementing orthogonal E_x and E_y dual polarizations. Such dual-polarization operation is not supported by metallic hollow waveguides. Data rates of 24 Gbit/s (E_x) and 22 Gbit/s (E_y) are recorded. In addition to dielectric waveguides, THz hollow-core fiber is investigated for the realization of short-range applications that require some degree of flexibility. The fundamentals of THz hollow-core fibers including the multi-mode operation, the dispersion, and the loss are analyzed. Loses of 10 dB/m and 15 dB/m for 1 mm, and 0.7 mm core fibers, respectively, are confirmed in experiments. An all-Si linear taper interface for coupling with THz fiber is implemented with a coupling efficiency of >60 %. In addition, a rod array interface and semi-hemispherical lens interface were systematically investigated, revealing coupling efficiencies of 80% and 40%, respectively. THz fiber link communication with dual polarization is demonstrated, achieving data rates of 22 Gbit/s, and 18 Gbit/s for the E_x and E_y polarizations, respectively.

The achieved results show that ultra-broadband Si waveguides could lead to the realization of more advanced intra-/inter-chip or board communications using THz waves.

Table of contents

Chapter 1

Background and motivation

This doctoral thesis investigates broadband all-Si waveguides in the THz region. The interest in the THz region arose from the advantages of the frequencies in the sub-THz and THz region because of the increased operational bandwidth. In this section, review previous research on THz range waveguides, to clarify the motivations and goals of this work.

1.1 The THz region and its potential

As the networks and supporting infrastructure are evolving towards more superior configurations to address the ever-growing needs owing to the proliferation of nascent technologies, wireless communications are positioning themselves as prime network configurations for connecting several devices and end-users spread across a much wider geographic range. This is pushing devices and systems to exhibit larger bandwidths and higher directivity for the benefit of faster and more secure communications. Thriving for larger bandwidths will push future networks and systems toward higher operating frequencies in the sub-THz and THz range. The frequencies of the THz range are best suited to meet the requirements of the future networks for 5G and beyond because they leverage both the advantages of the microwave and infrared (IR) regions:

- Huge spectral bandwidth: Faster communications owing to higher channel capacities.
- Short wavelengths: High directivity which allows for more secure communications and higher resilience to eavesdropping; In addition, short wavelengths allow for more

compact components with a much smaller footprint, which reduces component-level interferences.

- Pencil-shape beam: Increases angular resolution and could enable more accurate three-dimensional (3D) positioning estimations for autonomous systems.

For IR communications, the bandwidth tends to be limited compared to the THz range of up to a few hundred Mbit/s with a relatively short range of a few tens of meters. This is because IR waves are not immune to scattering, noise, and reflection.

Although THz waves previously reported high-data rates in wireless communications links, there are still a few challenges to overcome to make the most of the full potential of the THz region (0.1 – 10 THz). Major performance bottlenecks of wireless THz communications include strong dependence on weather conditions. That is, atmospheric absorption is exacerbated by rain, fog, and snow [1]–[4]. In addition, THz links experience strong signal interference and high free-space path loss [5] in ultra-dense wireless networks, which is most likely the configuration of the cities and networks of the future [6]. The nature of the devices employed in THz communications links also impacts the efficiency of THz communications. Specifically, most THz components tend to require very stringent alignment between the transmitting unit and the receiving unit. Such stringent requirements become more crucial when dealing with an all-dielectric type of component that tends to be much smaller in the physical dimension. In most cases, additional external collimating lenses are employed to ease the alignment, but that renders the whole system bulky. Consequently, THz wired communication might alleviate the challenges related to wireless THz communications links, while maintaining the full advantages of the THz spectrum.

1.2 THz waveguides

1.2.1. Review of THz waveguides

For a long time, THz range interconnects have been limited to metal-based transmission lines and wave confining structures, as well as dielectric waveguides. Metallic waveguides are associated with increased ohmic losses at higher frequencies [7]–[9], and dielectric waveguides tend to have higher losses due to the absorption of the dielectric material [10]. Empirical THz range waveguides include metallic hollow waveguides (rectangular and circular cross-sections),

dielectric coated metallic waveguides, planar transmission lines (coplanar, slot line, and stripline), polymer fibers, photonic crystal fibers, substrate integrated image waveguides (SIIG), and ribbon waveguides among others as illustrated in Figure 1.2:

- Metallic waveguides such as hollow waveguides have been a standard for interconnecting with external power sources, testing, and packaging in the THz range [11]–[13]. This is because waveguides in the THz range are built upon well-established waveguides in the microwave region, such as the metallic rectangular and circular waveguides [14]. Like most metallic waveguides, hollow waveguides rely on guided waves by metallic media (GMM). These waveguides yielded good performance in the microwave region, but when extended to the THz region, the physical size of these waveguides is significantly reduced. This renders foundry processing difficult as extreme accuracy is sometimes required for manufacturing. Another difficulty associated with the physical size of the metallic waveguides in the THz range is the difficulty of interconnecting with planar components of a different scale. This led to a modal mismatch at the interface with the hollow waveguide. In most cases, a matching structure that can progressively convert the modes from the large aperture of the metallic waveguide to a much smaller aperture is needed. Besides, the non-planar profile of these waveguides makes it difficult to achieve compact packaging. This is a crucial hindrance for THz integrated circuits (ICs). More design considerations must be taken. In addition, because ohmic losses are increased with metal material, the overall performance of the THz system built using such waveguides can be significantly reduced, knowing that there is a lower available power in the THz region compared to the microwave region. The reported loss for the WR-2.8 waveguide (710 μm × 355 μm) is ~0.2 dB/cm for the lower limit of the WR-2.8 band of 260 GHz and ~0.4 dB/cm for the upper limit of 400 GHz [15].
- Parallel-plate waveguides have been widely used for the generation and transmission of THz waves. They consist of two conducting plates positioned closely together. These waveguides offer single-mode operation. The reported propagation loss was 0.3 dB/cm in 0.1 – 4 THz [16].

- Dielectric-coated waveguides also suffer from increased ohmic losses in the THz range. However, propagation loss has been reduced by employing dielectric coating on the metallic waveguide's inner walls, as reported in [17]–[23][24]. This is because the coating allows the electric fields to vanish at the interface with the metallic wall. This is in contrast with metallic rectangular and circular waveguides, where the THz waves do not vanish at the interface with the metallic walls, but penetrate the walls and absorption occurs. The reported [20] propagation loss of dielectric-coated waveguides of 0.01 dB/cm was achieved. The loss can be further reduced by optimizing the thickness of dielectric cladding. Reducing the thickness of the cladding translates into reducing the inner diameter of the waveguide, modal matching with THz pulses can be achieved, and higher coupling can be achieved between the dominant mode of the waveguide and THz waves [25]. The increase of the coupling efficiency with the dominant mode is associated with a reduced coupling efficiency with higher-order modes. A further reduction of coupling with higher modes eventually leads to the suppression of those modes and further to a single-mode operation that is ideal for a waveguide.
- Polymer fibers physically resemble the dielectric hollow waveguide as they present a circular profile. A noticeable difference is the diameter of the waveguide. In the case of polymer fiber waveguides, the diameter is subwavelength, i.e., the diameter is smaller than the operating wavelength. The waveguiding is analogous to that of the circular metal waveguide, and the losses are a combination of radiation loss and material absorption. The radiation loss originated from non-uniform variations of the diameter, whereas absorption loss results from the polymer material. A propagation loss at 300 GHz was reported as low as 0.01 dB/cm [26]. It is particularly difficult to manufacture fiber with a uniform diameter in the THz range. The diameter for such fiber can be as small as the tens of microns scale for mid to higher THz frequencies.
- Transmission lines with a more planar profile have been of great interest as efficient THz range interconnects. This includes coplanar, microstrip, and stripline transmission lines. The interest in these waveguides for the THz range has not been greatly significant because these transmission lines are associated with high dispersion and attenuation [27]. The electromagnetic waves leak both in the substrate and the air for microstrip and

coplanar transmission lines. Propagation loss for coplanar, microstrip, and stripline waveguides can be quite as high as 10 dB/cm, 15 dB/cm, and 6 dB/cm, respectively [28].

- Photonic crystal waveguides have been prime THz waveguides with also a planar profile. Contrary to the traditional transmission lines, photonic crystal waveguides have no substrate. Therefore, substrate absorption loss is suppressed. In addition, strong in-plane confinement is achieved because of the photonic band gap (PBG) effect, yielding very small leakage into the air. Photonic crystal waveguides with extremely low loss and low propagation have been recently reported [29]–[31]. Photonic crystal waveguides are covered in more detail in the dielectric waveguide section.
- Photonic crystal fibers can be viewed as fibers with a photonic crystal core. As such, the guiding mechanism is the PBG effect. Early reports of such waveguides go back to 1996 with the report of single-mode silica photonic crystal fibers for the light wave region [32] and have since been efficient ways to generate THz waves [33].
- The structure of SIIGs is composed of a dielectric core and two low refractive index porous walls on each side of the core. Consequently, their guiding mechanism is total internal reflection (TIR). SIIG with propagation loss as low as 0.35 dB/cm was reported in [34].
- Ribbon waveguides also rely on TIR as a guiding mechanism. Their structure is simple and only comprises low-index dielectric cores such as graphene cores [35]. Such structures have reported a propagation loss of 0.087 dB/cm when operating 100 – 130 GHz.

The performance of these waveguides is summarized in Table 1.1.

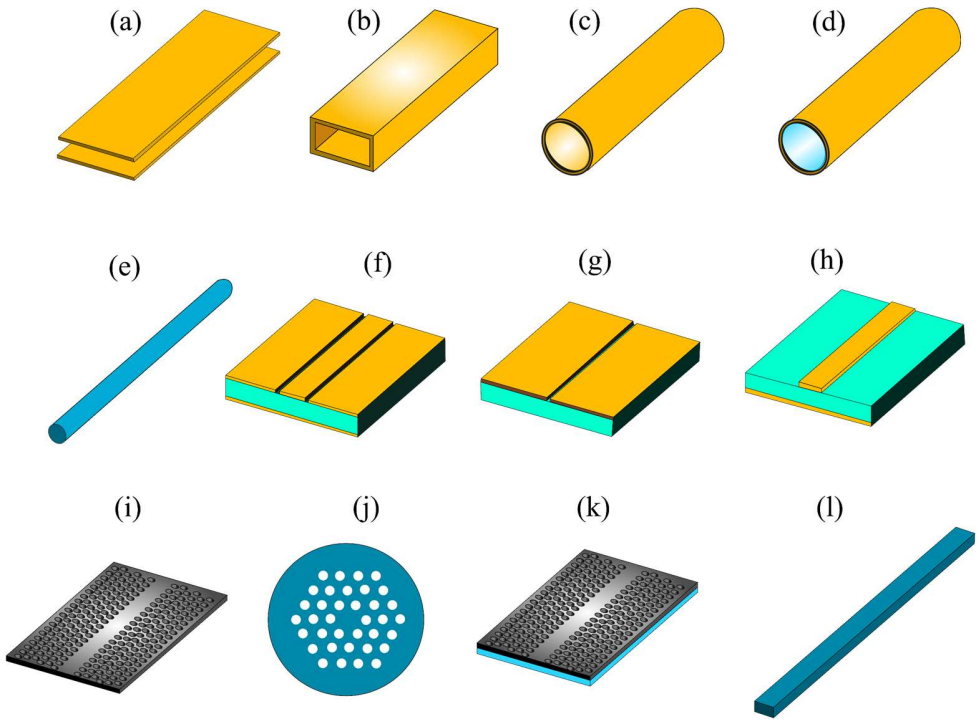

Figure 1.1: Waveguides for THz range, (a) parallel plates waveguide, (b) rectangular metallic waveguide, (c) metallic circular waveguide, (d) circular waveguide with dielectric coating, (e) polymer fiber, (f) coplanar showing substrate in aquamarine color, (g) slot line, (h) stripline, (i) photonic crystal waveguide, (j) photonic crystal fiber, (k) SIIG with a dielectric substrate, (L) ribbon waveguide. The colors gray, yellow, and blue represent Si, metal low-index dielectric material, respectively.

1.2.2. Superior waveguides: The improvements of high-resistivity Si dielectric waveguides

Implementing introducing periodic alterations such as holes into Si slabs has led to the low loss THz dielectric waveguides. In principle, there are various possibilities for hole configurations, and the performance of the resulting waveguides varies extensively.

Table 1.1: Comparison of THz empirical waveguides

Reference	Waveguide	Frequency (GHz)	Propagation Loss (dB/cm)	Confinement principle	Integrability
[16]	Parallel metal plates waveguide	100 – 4000	<0.3	GMM	No
[15]	WR-1.0 rectangular hollow waveguide	750 – 1100	1.92 – 1.35	GMM	No
[20]	Circular coated hollow waveguide	-	0.01	GMM	No
[26]	Polymer fiber	320 – 350	< 0.01	TIR	Yes
[36]	Microstrip line	Up to 1000	43.4	GMM	Yes
[27]	Coplanar waveguide	Up to 1000	65	GMM	Yes
[28]	Slot line	Up to 1200	26	GMM	Yes
[31]	Photonic crystal	324 – 361	< 0.1	PBG	Yes
[37]	Photonic crystal fiber	171 – 352	~18	PBG	Yes
[38]	Ribbon	100 -140	0.087	TIR	No
[34]	SIIG	85-105	0.35	TIR	Yes

GMM: Guided waves by metallic media, TIR: Total internal reflection, PBG: Photonic Bandgap, SIIG: substrate integrated image waveguide.

1.2.2.1. High resistivity Si and slab-modes confinement in planar waveguide structures

Research efforts have been dedicated to making the most out of what appears to be an endless spectral bandwidth. However, challenges related to the generation, manipulation, and transmission of THz waves arose and forced researchers to seek effective methods for controlling THz waves. The response to this problem was found in photonic crystal slabs. Photonic crystal slabs are two-dimensional (2D) structures made of semiconductor material that an array of through-holes has perforated, as illustrated in Figure 1.2. Consequently, the resulting structure exhibits a stopband, also known as PBG, where no transverse-electric (TE) where the electric field is oriented parallel to the slab plane, fields exist because the array of holes created

a periodically varying refractive index in the structure. For the components made of photonic crystals, the wider the bandgap is better for applications requiring larger bandwidth. The size of the bandgap can be controlled by the arrangement of the holes of the array. Indeed, there is quite a degree of freedom in designing photonic crystal waveguides. With the desired bandgap size as a design starting point, different arrangements of the array of holes can be found to meet that criterion. Key design parameters for photonic crystals include the lattice constant *a*, i.e., the distance between the centers or two adjacent holes and the hole diameter *d*. The methods for finding the right values for *a* and *d* vary from simple parameter sweeps to more advanced algorithms [39], [40].

The first occurrences of photonic crystals go back to 1973 when the periodic structures in integrated optics were reported [41]–[43]. Photonic bandgap, as described, provides a degree of control of THz waves, as they can be engineered to block out THz waves for a given frequency range. The PBG can also be used to further the control and manipulation of THz waves. In 2005, Fujita *et al.* demonstrated the concept of simultaneous inhibition and redistribution of spontaneous light emission in photonic crystal slab [44], [45]. Indeed, there are two optical modes in a photonic crystal slab: "slab modes" and "vertical modes". Slab modes are confined in the 2D photonic crystal slab plane by satisfying TIR for the vertical direction. In contrast, vertical modes do not satisfy TIR and leak out of the slab. Manipulating these modes allows control of spontaneous light emission in 2D photonic crystals. Specifically, with a photonic crystal waveguide structure incorporating a single quantum well, that emits light with a TE polarization parallel to the slab plane, the spontaneous rate decreases due to the PBG effect. In contrast, the emission rate into the directional normal to the slab plane increases via energy redistribution. Reduced spontaneous emission is associated with an increase of redistribution by the same amount in the PGB region as reported in [44]. This implies that 2D photonic crystals can effectively be used to control THz waves. Subsequently, Kakimi *et al.* demonstrated that THz waves could be trapped in a photonic crystal slab [46].

Trapping and controlling THz waves in photonic crystals can be achieved by leveraging the resonance state. The resonance state is reached when the lattice constant of the photonic crystal is equal to the wavelength in the medium. THz waves normally incident to the plane of the photonic crystal slab in the resonance state are trapped inside the photonic crystal, and the

in-plane resonant mode is excited. The trapped wave then gradually leaks out of the photonic crystal. However, the degree of wave confinement in the photonic crystal slab depends on the material absorption of the photonic crystal [46]. With the appropriate amount of absorption, THz waves can effectively interact with the absorption and decay in the slab and not leak. This provides another means to control trapped THz waves in photonic crystal slabs.

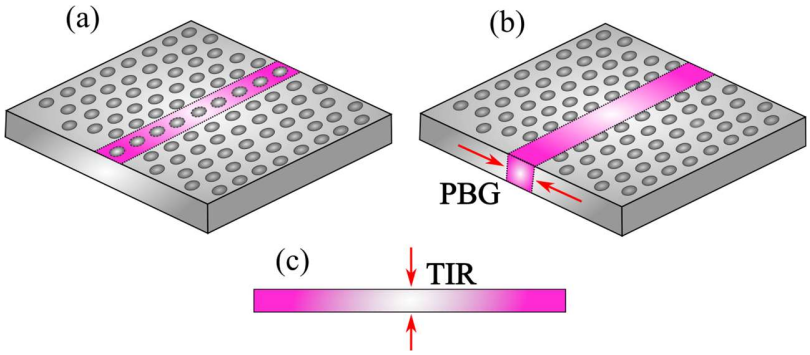

Figure 1.2. THz waves in photonic crystals, (a) Photonic crystal slab showing PGB effect and removable holes (violet region) to create waveguide track, (b) photonic crystal waveguide showing PBG effect and removed holes to create waveguide track, (c) Illustration of TIR for THz waves confinement in the transverse plane.

1.2.2.2. Photonic crystal waveguides

Photonic crystal waveguides are realized by creating a line defect into photonic crystal slabs. Precisely, an entire row of through-holes is filled with semiconductor material to create a path for the waves to propagate, creating a waveguide. The waveguiding principle for photonic crystal waveguides translated into field confinement is dependent upon PBG. In the TE bandgap region, the propagation of THz waves with in-plane polarization is inhibited. Early reports on photonic crystal waveguides go back to 1999 when the observation of light transmission in photonic crystal waveguides at light wave region [47]. Subsequently, linear waveguides and waveguide bends were introduced in [48]–[50] around 2000. Until 2006, the pioneering work on 2D photonic crystal waveguides for fluid sensing by T. Hasek *et al.* demonstrated photonic crystal waveguides for practical applications such as sensing. Indeed, there is extensive literature exploring PBG and its potential for manipulating THz waves but not as much as proof of concept for real-life applications. In their work, T. Hasek *et al.* provided experimental proof

of concept to theories on measurements methods for fluids and deoxyribonucleic acid for sensing application in the healthcare industry [51], [52] using a 2D photonic crystal waveguide implemented in a high-density polyethylene [53]. However, it is noted that other photonic crystal structures, such as the parallel plates photonic crystal waveguides, were also widely used [54]. Such structures are metallic and are bound by parallel plates in the vertical direction and by a square lattice of holes in the horizontal axis. This is because parallel plates have widely been used to demonstrate efficient guiding of THz waves with little distortion. However, parallel plate waveguides are less efficient at a higher level of integration, and given that they are made of metal, the losses are quite significant. In addition, the beam can only travel in one direction, hence giving very little control. Therefore, spatial confinement and directional control can be achieved by combining a 2D photonic crystal waveguide with parallel plates.

In the meantime, as progress on photonic crystal slabs and photonic crystal waveguides was being made, there was still a crucial issue to address, namely the loss of photonic crystal waveguides. In 2009 Juisheng and Xiaoli reported a Si photonic crystal waveguide with the lowest propagation loss of 9.9 dB/cm at 280 GHz in 270 – 330 GHz [55]. In 2013, Tsuruda *et al.* demonstrated a photonic crystal waveguide with reported loss as low as 0.2 dB/cm for both straight waveguides and waveguide bends loss[56] [57] for 0.315 – 0.329 THz. Such low loss was achieved by employing a 200 μm-thick high resistivity (20 kΩ) Si combined with proper lattice constant and hole diameter values. The bending degree is an additional design parameter to consider for low propagation loss. In general, it is preferable to seek a gradual transition of the waves propagating through the bend. Subsequent research on photonic crystal waveguides reported low propagation loss across an improved bandwidth with high resistivity intrinsic Si. In 2015, Otter *et al.* introduced variable attenuators and resonators into the photonic crystal waveguide [58]. By illuminating the waveguide with laser light to generate free carriers in the Si waveguide, the propagation loss of a photonic crystal waveguide can be increased so that it behaves as an attenuator. Other defects, such as L3 defects, i.e., removing three adjacent air holes, can create a compact cavity in photonic crystal slabs. Such cavity resonators are essential for applications such as sensing, which has been a key target application for the THz range [59]–[63]. Although many resonators were realized for millimeter waves, they were mostly made of metal, as reported in [64], [65]. In addition, most millimeter-wave resonators did not have a

planar form factor. For THz integrated systems, resonators made of low-loss materials and having a planar profile are better suited.

1.2.2.3. Effective-medium waveguides

An EM is a composite material with properties inherited from combining all the properties of the different constituents that make up the composite material. For dielectric EM waveguides, there are two constituents, namely the dielectric material, and air. This is because EM structures are created by introducing an array of through-holes into a dielectric slab. All-Si EM structures have gained popularity because of their low transmission loss and wideband operation, as reported in [66]. In their work, Gao *et al.* reported a waveguide core clad with EM. In comparison with photonic crystal waveguides, the in-plane guiding mechanism in EM waveguides is based on TIR, not on PBG. In addition, the diameter of the holes and the perforation period dimensions are extremely small, which ensures that the resulting structure behaves like a homogenous structure [67]. As a consequence, EM waveguides exhibit an enhanced bandwidth and low dispersion. For the design of the EM structures, a hexagonal lattice can be employed with a lattice constant smaller than the guided wavelength. Because the EM structure is composed of intrinsic Si and air, the resulting effective refractive index is between the refractive index of Si and that of air [67], [68]. As such, bigger holes will yield an EM structure with an effective index closer to air, while smaller holes will yield an effective index closer to Si. This creates a 2D index contrast that helps confine the waves within the waveguide core by TIR. The guiding mechanism of EM waveguides is thus solely based on TIR made possible by the high index contrast in both transverse dimensions. However, due to the low cladding index in both planes, i.e., EM cladding and air cladding, EM waveguides typically support two fundamental modes, one parallel to the slab (E_x) and another one perpendicular to the slab (transverse magnetic (E_y) mode). These modes are associated with electric fields having distinct relative permittivities that can be approximated using the Maxwell-Garnett approximations and given by the following equations [69]:

$$\varepsilon_x = \varepsilon_{Si}\frac{(\varepsilon_0 + \varepsilon_{Si}) + (\varepsilon_0 - \varepsilon_{Si})\zeta}{(\varepsilon_0 + \varepsilon_{Si}) - (\varepsilon_0 - \varepsilon_{Si})\zeta} \qquad (1-1)$$

$$\varepsilon_y = \varepsilon_{Si} + (\varepsilon_0 - \varepsilon_{Si})\zeta \qquad (1-2)$$

Where ε_0 and ε_{Si} are respectively the permittivity of air and Si, and ζ represents the filling factor of the air in Si.

The value of the filling factor is dependent upon the pattern of the array of holes. For example, for a square lattice in which the holes are arranged in square patterns, the lattice constant is estimated as $(\pi a)/(4a)$, where *d* is the hole diameter, and *a* is the lattice constant, i.e., the distance between the centers of two adjacent holes. And for a hexagonal lattice, the value of the filling factors can be estimated as $\left(\pi d^2/2a^2\sqrt{3}\right)$. These values for the filling factor can be deducted from algebraic considerations of the lattices. The choice of the lattice, however, can be motivated by robustness. In this case, the isosceles lattice has been preferred compared to other lattices [70]. In the case of EM-clad dielectric waveguides, additional considerations must be made. Notably, careful considerations must be taken for the desired propagation mode and the degree of confinement that will impact the waveguide transmission. For the propagating modes supported by the EM waveguides, it is noted that the relative permittivity must be selected to enable single-mode propagation. Notably, lower relative permittivity generates a smaller propagation constant which causes the cutoff frequencies of the higher modes to be moved up to higher frequencies in the operation band. Therefore, attention must be paid to choosing the right relative permittivity. The realization of broadband THz integrated systems employing EM structures depends on the efficient integration of functional components. Building upon highly broadband EM waveguides, subsequent research reported Bragg filters [71], planar lens [72]–[75] and beam splitters [76], [77] based on EM structures.

1.2.2.4. Unclad waveguides

Despite the performance of EM waveguides, the main hindrance to their use is the difficulty of fabrication associated with the small size of the holes that constitute the EM structure. Indeed, high-precision machining would be required to manufacture subwavelength hole diameters. Unclad waveguides were introduced by Headland *et al.* in 2020 to address this

issue [78]. The term “unclad” refers to the absence of cladding as these waveguides are substrateless and entirely clad by air. The main motivation is to reduce the complexity of the structure by removing the EM structure. Long before unclad structures, Si on insulator technology was used for THz range waveguides in which the waveguide core was laid on top of an insulator substrate in most cases Si dioxide (SiO_2) [79], [80]. However, SiO_2 is typically more absorbent than high-resistivity Si, which increases the loss of the waveguides owing to the absorption loss of the substrate material.

Intuitively, losses should be reduced by removing a portion, even the entire substrate. Such considerations led to suspended waveguides [81], [82]. Suspended waveguides are micro-scale waveguides entirely substrate-less. However, the suspended waveguides are not self-supporting, which is not very practical for physical handling. Photonic crystal structures commonly provide support for suspended waveguides. Photonic crystal structures typically have limited bandwidth and increased dispersion in the PBG region. This renders suspended waveguides narrowband and dispersive. Subsequent research was oriented toward Si on glass waveguides [81], [83]. However, for THz integrated systems, all-Si components are preferred. Such consideration led to the most recent unclad waveguides. Unclad waveguides have been developed as an extension of EM waveguides by removing the in-plane EM cladding structure with a protective Si frame [78]. The resulting waveguide offers more simplicity and greater freedom in choosing crucial design parameters such as waveguide thickness, which translates into faster analysis, simulations, design, and fabrication. Like EM waveguides, unclad waveguides can be fabricated in all intrinsic Si, thus enabling monolithic integration with various functional devices and physical supporting elements entirely made of Si. The appearance of the supporting element can be designed to fit physical packaging and for handling and testing. All-Si unclad waveguides establish a platform for the integration of Y-branches, couplers, and multiplexers. The absence of EM cladding facilitates hybrid integration. Unclad waveguides have reported transmission loss of < 0.1 dB/cm, making it possible to achieve more complex designs requiring higher and more complex bending. 90-degree circular bends Y-branch were realized based on unclad structures as well as evanescent couplers. Structures like resonators were also reported in suspended waveguides using one period of photonic crystal structure [84].

Various all-Si waveguides have reported improved performance in comparison to their metallic counterparts. In addition, these waveguides have positioned themselves as an efficient canvas for the realization of several functional components that are indispensable for the realization of a complete communication system. Table 1.2 below provides a summary of all-Si waveguides and their performance.

Table 1.2: Performance of all-Si dielectric waveguides.

Reference	**Waveguide type**	**Operation frequency range (GHz)**	**Relative bandwidth (%)**	**Reported propagation loss (dB/cm)**	**Demonstrated Applications**
[31], [63]	Photonic crystal	319 – 337	~ 5	0.04	Communications (1.5 Gbit/s), high-definition video transmission Sensing
[60]	Photonic crystal	100	N/A	-	Liquid sensing
[29]	Photonic crystal	324 - 361	~11	< 0.1	Communications (36 Gbit/s)
[66]	EM	260 - 400	> 40	0.05	Communications (30 Gbit/s), 4K video transmission
[85], [86]	Topological	320 - 350	~8	< 0.1	Communications (108 Gbit/s), 4K video transmission
[78]	Unclad	260 - 390	~40	0.059	Communications (30 Gbit/s), Sensing
[87]	Suspended	500 - 750	~40	0.065	-
[88]	EM	500 - 750	~40	-	Communications (10 Gbit/s)

1.3. Purpose and significance of this work

This doctoral thesis expounds on ultra-broadband Si waveguides for advanced applications in the THz region. The goals aimed throughout the research projects undertaken as part of the doctoral studies are summarized as follows:

- Develop low-loss and broadband dielectric waveguides at extremely high frequencies: This research aims to develop all-dielectric low-loss interconnects for frequencies in the WR-1 band (0.75 – 1.1 THz) to increase the operational bandwidth. This is to address

the increasing need for broadband operation of THz components. The methods employed in this project include a parametric study of critical design parameters and their impact on the operation of the devices, the establishment of novel testing techniques for the experimental evaluation of devices with extremely small features operating at extremely high frequencies, and the methods for analyzing the performances of those devices.

- Implement novel dual orthogonal polarization toward achieving higher communication throughput: This research seeks to demonstrate dual polarization for increased aggregate data rates. The methods employed include leveraging low-loss dielectric waveguide interfaces and their aptitude to support multi-mode operation, in addition to the modal analysis of the dielectric unclad waveguide.
- Demonstrate low-loss, low-cost, and efficient flexible THz dielectric waveguides: This research axis aims to provide alternative waveguides for the THz region that are also flexible, to unlock multiple attractive applications for short-range, high-capacity interconnections that are gaining more and more attention for data centers and intra-/inter-chip infrastructures. The methods employed in this project include the analysis and design of a dielectric waveguide coupler interface with a high coupling efficiency.

1.4. Thesis overview

This dissertation thesis is organized as described in Figure 1.3 below.

Chapter 1 explored empirical THz waveguides that are widely employed for various applications including test and measurement, packaging, and the realization of integrated circuits. A brief review of metallic waveguides, planar transmission lines, and dielectric waveguides is given. In addition, we clarify the performance of existing THz waveguides focused on waveguide loss and bandwidth to identify improvement opportunities.

Chapter 2 expounds on broadband silicon waveguides in the WR-1 band (0.75 – 1.1 THz). The design challenges for THz waveguides implementing periodic structures are presented.

Additionally, we introduce novel design strategies for the proposed waveguides. We design, fabricate and test two waveguide designs for comparative analysis of performance.

Chapter 3 Describes dual-polarization operation over THz dielectric waveguides, based on a linear taper interface. This chapter analyzes the multi-mode operation of THz dielectric waveguides and introduces a way of doubling the data rates with simplified waveguide designs.

Chapter 4 Introduces hollow-core THz fibers as alternative low-loss, efficient waveguides. A complete analysis of the fundamental properties of hollow core THz fibers including multi-mode operation and loss is provided. This chapter also explores various coupling structures for hollow core THz fibers based on dielectric waveguides.

Chapter 1: Background and motivation

Chapter 2: Broadband silicon waveguides in WR-1 band (0.75 - 1.1 THz)

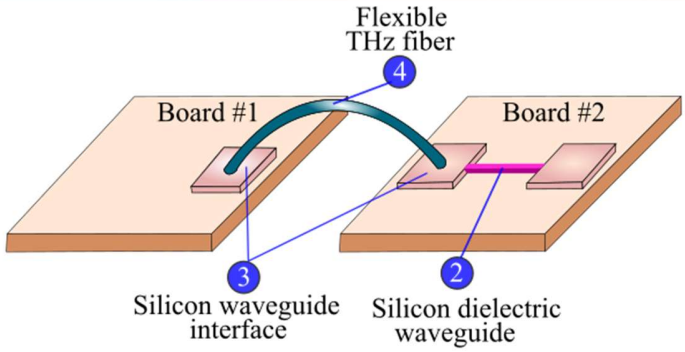

Chapter 3: Dual polarization operation in THz range devices based on silicon waveguides toward higher-data rates communications

Chapter 4: Hollow core THz fibers

Chapter 5: Conclusions and future perspectives

Figure 1.3. Organization of this thesis.

Chapter 2

Broadband silicon waveguides in the WR-1 band (0.75 – 1.1 THz)

The development of more sophisticated and capable THz systems requires current research to focus on higher frequencies targeting the frequencies in the WR-1 band (0.75 – 1.1 THz). These ultrahigh frequencies could contribute to accelerating future applications such as space exploration [89], non-invasive and non-destructive super-resolution imaging [90], [91], sensing [63] and ultrafast wireless communications [92]. In this section, we introduce low-loss and broadband dielectric waveguides in the WR-1 band (0.75 – 1.1 THz).

2.1. Low-loss all-dielectric waveguides

2.1.1. Design challenges in the WR-1 band: EM analysis

As the carrier frequency increases, increased data rates can be achieved, owing to increased bandwidth [9]. Indeed, communication channel capacities increase with frequency because of the increased bandwidth as illustrated in Figure 2.1. Hence, data rates as high as one terabits/s in wireless communications can be achieved [93]. A noticeable advantage of components built in all-Si material and operating in the THz region (0.1 – 10 THz) is the reduction of the propagation loss determined by the absorption loss of the Si material. With an increase in frequency, the absorption loss due to free carriers in Si decreases [14]. This is

different from metallic structures, which show increased absorption loss at higher as shown in Figure 2.1.

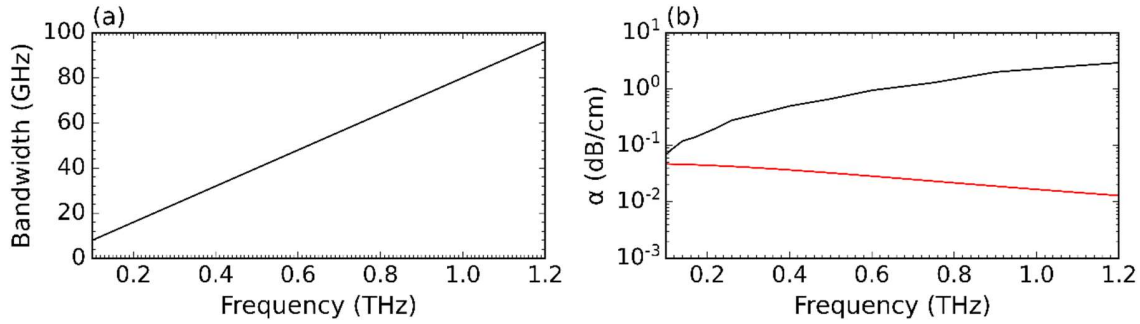

Figure 2.1. Advantages of the THz region: (a) extrapolation of the bandwidth as a function of frequency considering the performance of the dielectric waveguide reported in [66], (b) absorption loss for Si (red) and metal (black) as a function of frequency.

The waveguides proposed in this study rely on EM theory, which allows the engineering of novel materials whose properties are inherited from the constituent composite materials. The waveguides previously reported for the WR-2.8 band (0.26 – 0.39 THz) achieved good performance with hole pitches of 100 µm and 120 µm, as reported in [66] and [78], respectively, while maintaining a minimum manufacturable limitation of 10 µm for hole diameter *d* of 90 µm and 110 µm, respectively. Following a simple scaling of [66] and [78] to (0.75 – 1.1 THz) would render a hole pitch of ~35.7 µm and ~42.8 µm, respectively; and the scaling hole diameter would be 32.1 µm and 39.2 µm. This will lead to 3.2 µm and 3.6 µm clearance between two consecutive holes. However, such small distances are not manufacturable.

The EM theory requires that the hole pitch should be chosen smaller than the quarter wavelength in the EM. Given that the minimum wavelength in WR-1 is ~270 µm, the quarter wavelength in EM is ~20 µm at 1.1 THz with a refractive index of 3.418. Choosing the correct values of *d* and *a* will help in changing the refractive index, as *d* and *a* define the air fill factor, which represents the ratio of air in an all-Si slab. According to Equation (1), the refractive index decreases with the filling factor, as illustrated in Figure 2.1. For example, a refractive index of 2, which corresponds to $d = 35$ µm and $a = 45$ µm, would yield a quarter wavelength in EM ~35 µm. This should satisfy the minimum manufacturability dimension condition of 10 µm. However, considering air cladding in the plane perpendicular to the waveguide, the 3D index

should be further reduced. In addition, the air fill factor for the associated refractive index is ~ 0.73 as illustrated in Figure 2.2. Therefore, additional considerations are required to increase the minimum distance between two adjacent holes to the minimum manufacturable dimension of 10 µm and decrease the refractive index to 0.52. This could be achieved by increasing the waveguide width *W*. A study of the waveguide performance for different values of *W* and the waveguide thickness *T* as shown in Figure 2.4, revealed that the waveguide width *W* has a larger impact on the improvement of the transmittance. Figures 2.4 (a) and 2.4 (b) show that the thickness of the waveguide has no impact on the transmittance, whereas Figure 2.4 (c) reveals that the transmittance is improved by ~1 dB at 0.75 THz when the waveguide width is increased from 80 µm to 100 µm for the unclad waveguide. Figure 2.4 (d) reveals a similar improvement of ~1 dB at 0.75 THz.

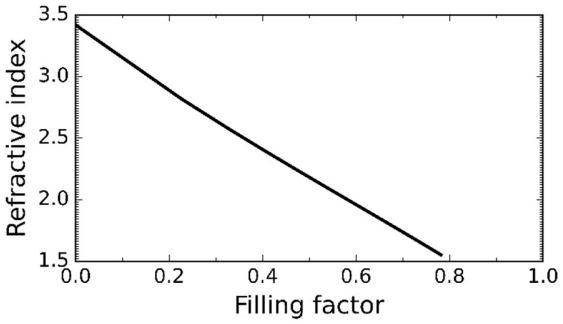

Figure 2.2. The refractive index of EM structure as a function of air filling factor.

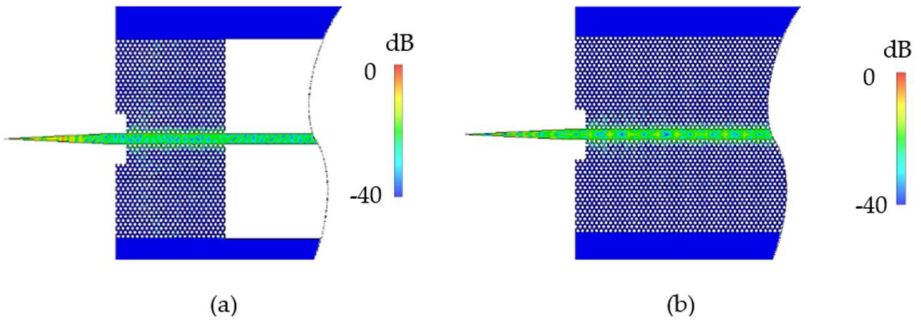

Figure 2.3 Electric field distribution at 0. 925 THz: (a) Filed distributions for the unclad waveguide showing THz waves confined in the Si wire core; (b) Field distributions for EM waveguide showing maximum confinement in the waveguide track and minimum leakage in the cladding.

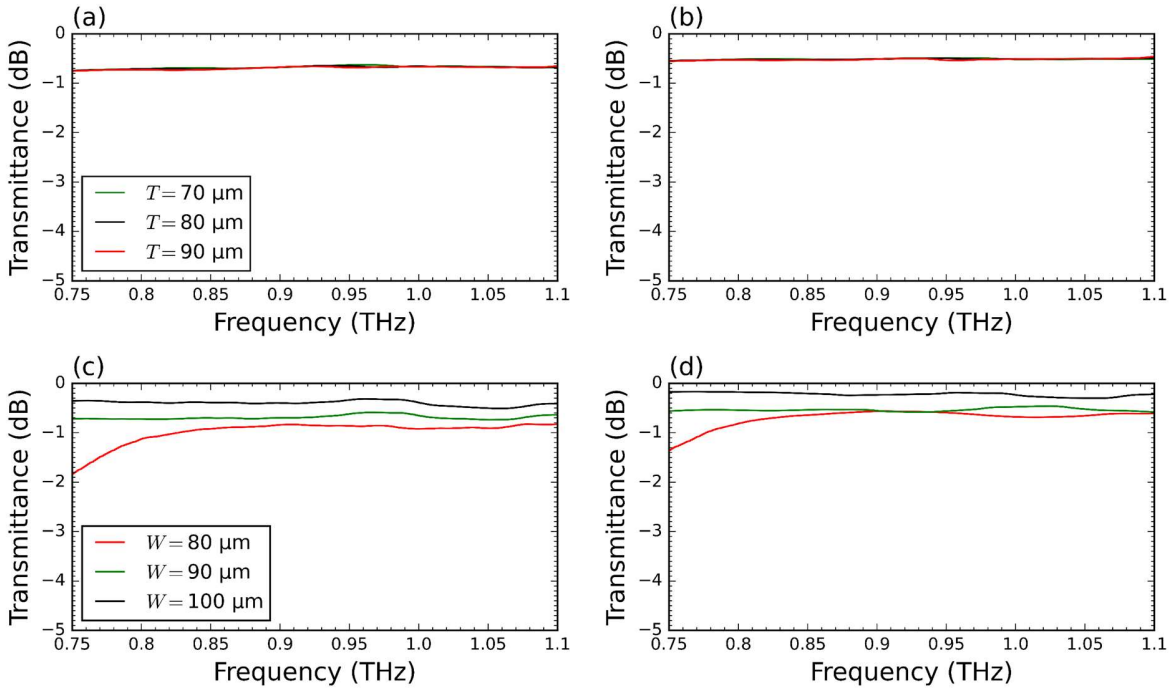

Figure 2.4 Analysis of the impact of T and W on the performance of 1 cm-long unclad waveguide and EM waveguide: (a) Transmittance of unclad waveguide for T = 70 μm (green), T = 80 μm (black), T = 90 μm (red) and W is fixed at 100 μm; (b) Transmittance of EM waveguide for variable T with fixed W = 100 μm; (c) Transmittance of unclad waveguide for W = 80 μm (red), W = 90 μm (green), W = 100 μm (black) and T is fixed at 80 μm; (d) Transmittance of EM waveguide for variable W with fixed T = 80 μm.

2.1.2. Modal analysis

As shown in Figures 2.4 (c) and (d), the transmittance of the waveguide is greatly improved by increasing the waveguide width. This is because the guided modes of the waveguides are confined to the line defect that constitutes the waveguide core. As a result, the performance of the waveguide is greatly impacted by the waveguide core. The performance of waveguides is usually assessed through a few key parameters such as the propagation constant β, the modal index n, the group velocity v_g and index N, and the dispersions parameter D. These parameters are directly related. Equations (2-1), (2-2), (2-3), and (2-4) give the mathematical expressions for β, v_g, N, and D.

$$\beta = n \times \frac{2\pi}{\lambda} = \frac{\omega n}{c} \tag{2-1}$$

$$v_g = \frac{d\omega}{d\beta} \tag{2-2}$$

$$N = n + \omega\frac{dn}{d\omega} = n - \lambda\frac{dn}{d\lambda} \tag{2-3}$$

$$D = -\frac{2\pi c}{\lambda^2}\frac{dn}{d\lambda} \tag{2-4}$$

Where λ represents the wavelength, ω the angular phase, and c the velocity of light in free space. Equation (2-1) represents the propagation constant β as a function of the modal index n. The modal analysis of the proposed EM and unclad waveguides was conducted using the 3D finite integration method of CST studio 2021. For the simulation of the unclad waveguide, a Si wire of width 100 µm and thickness 80 µm of relative dielectric constant 11.68 for intrinsic silicon is surrounded by vacuum air blocks in-plane and in the transverse direction. This is because the unclad waveguide is simply a Si wire in free space. For the EM waveguides, the waveguide core of the same dimensions as the unclad Si wire is surrounded in-plane by an effective medium, which permittivity was calculated using the EM theory shown in Equations (1-1) and (1-2). Considering an EM section with a hole diameter d of 35 µm and lattice constant of 45 µm, the air fill factor $\zeta = 0.54$, which corresponds to a dielectric constant of 4.29.

Simulated propagation constants are shown in Figure 2.5 (a), and it can be deduced that the THz waves are well confined in the waveguide track, as for both the unclad and EM waveguides, the propagation constants are well above the light line in free space shown in black. In comparison, the unclad waveguide shows a propagation constant closer to the light line, as opposed to the EM waveguide. This could be attributed to the additional EM section in the design of the EM waveguide. Indeed, cladding the entire waveguide track with EM can offer better and tighter wave confinement than free space. As a result, the effective modal index of both the unclad waveguide is lower than the EM waveguide as shown in Figure 2.5 (b).

The resulting 3dB dispersion bandwidths for the unclad waveguide and the EM waveguides are presented in Figure 2.6 (a) and Figure 2.6 (b), respectively. Owing to low dispersion, the proposed designs for both waveguides have high dispersion bandwidths, ranging from 50 to 350 GHz. In the case of the unclad waveguide, the maximum dispersion bandwidth

is ~300 GHz at 1.15 THz. For the EM waveguide, the maximum 3dB dispersion bandwidth is ~350 GHz across 0.8 – 1.2 THz.

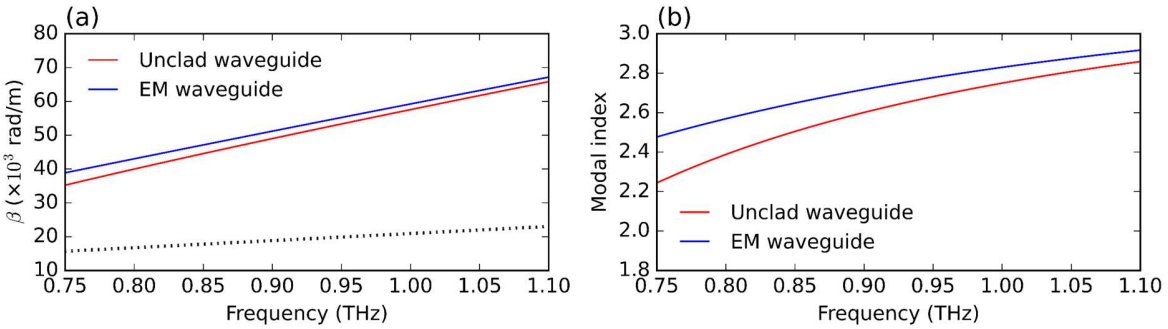

Figure 2.5 Modal analysis of unclad waveguide (red) and EM waveguide (blue): (a) Propagation constant and (b) modal index. The propagation constant of light in free space is shown in black.

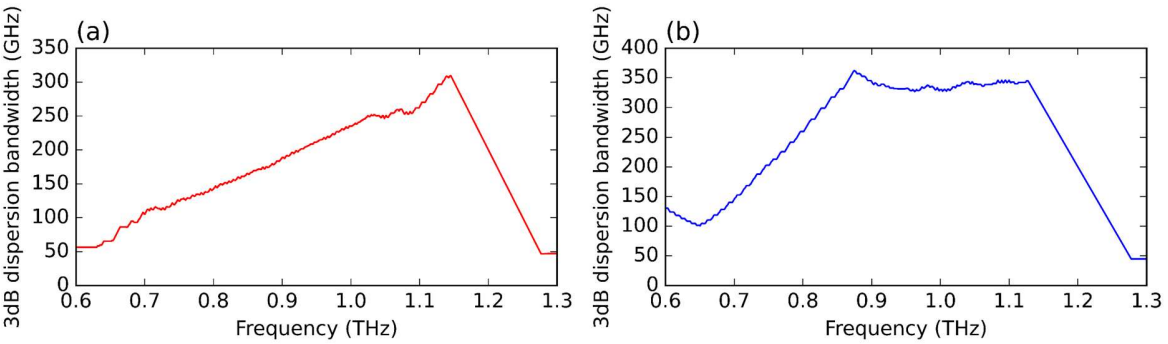

Figure 2.6 Simulated 3dB dispersion of unclad (a) waveguide and EM waveguide (b). In the case of the EM waveguide, the dispersion bandwidth is constant across 0.8 – 1.2 THz, owing to little dispersion disparities of the EM.

Based on the parametric analysis of the impact of the waveguide width on the transmittance, wider width of 100 µm show the best performance. However, because the number of modes supported by waveguides of this sort increases with the cross-sectional size, a multi-mode operation can be expected. To confirm this, the lower order modes of a Si wire waveguide of width 100 µm were simulated using CST studio suite 2021. The results shows are shown in Figure 2.7. A 100 µm wide waveguide would lead to the existence of multiple modes in the waveguides. The modes TE10, TE20, and TE01 are supported by the waveguide. TE11 and TE21 have a higher cutoff frequency of ~0.95 THz. Such multi-mode operation of the

waveguide in the WR-1 band can be exploited for the realization of polarization multiplexing at the higher band of the THz region. The topic of polarization multiplexing is covered in Chapter 3 of this dissertation.

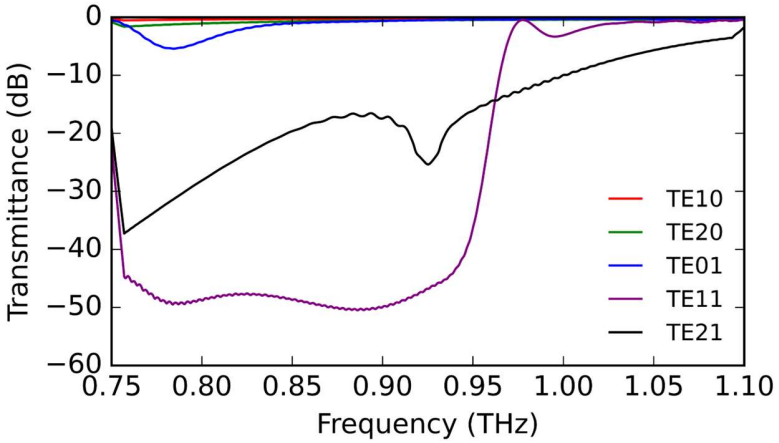

Figure 2.7 Supported modes of a Si wire of width 100 µm. The colors red, green, blue, purple, and black denote the modes TE10, TE20, TE01, TE11, and TE21 respectively.

2.1.3. Optimized waveguide design

The optimized designs for the EM waveguide and unclad waveguides are presented in Figure 2.8 (a), and Figure 2.8 (b), respectively. The EM waveguide has two main sections: the waveguide core consisting of a Si wire waveguide, and the EM section consisting of the cladding with periodic through-holes. The EM section is realized by introducing an array of through-holes in an 80-µm thick silicon slab with a relative permittivity ε_{Si} of 11.68, which corresponds to a refractive index of 3.418 and a resistivity of >10kΩ-cm. The holes have a diameter d = 35 µm and are perforated following an equilateral lattice with a period a = 45 µm. A simpler design with reduced complexity and ease of fabrication is achieved by excavating a portion of the EM section. For ease of handling and practicality, a small portion of EM cladding is maintained to implement all-Si frames. The EM section of the unclad waveguide is identical to that of the EM waveguides, that is, a = 45 µm and d = 35 µm. The waveguides are also built on 80-µm thick high-resistivity intrinsic Si. Both the EM and unclad waveguides have an EM

section that is 1.3 mm long in the case of the unclad waveguide and a length of L that corresponds to the length of the entire waveguide in the case of the EM waveguide. In both cases, the EM section is 2 mm wide. For both waveguides, the waveguide core is 100-µm wide and of thickness 80 µm. Alignment grooves of 0.5 × 0.5 mm^2 are implemented into the frames to help align the waveguides within the metal packaging. Each frame is 1.5 mm wide, which renders the total width of each waveguide 5 mm.

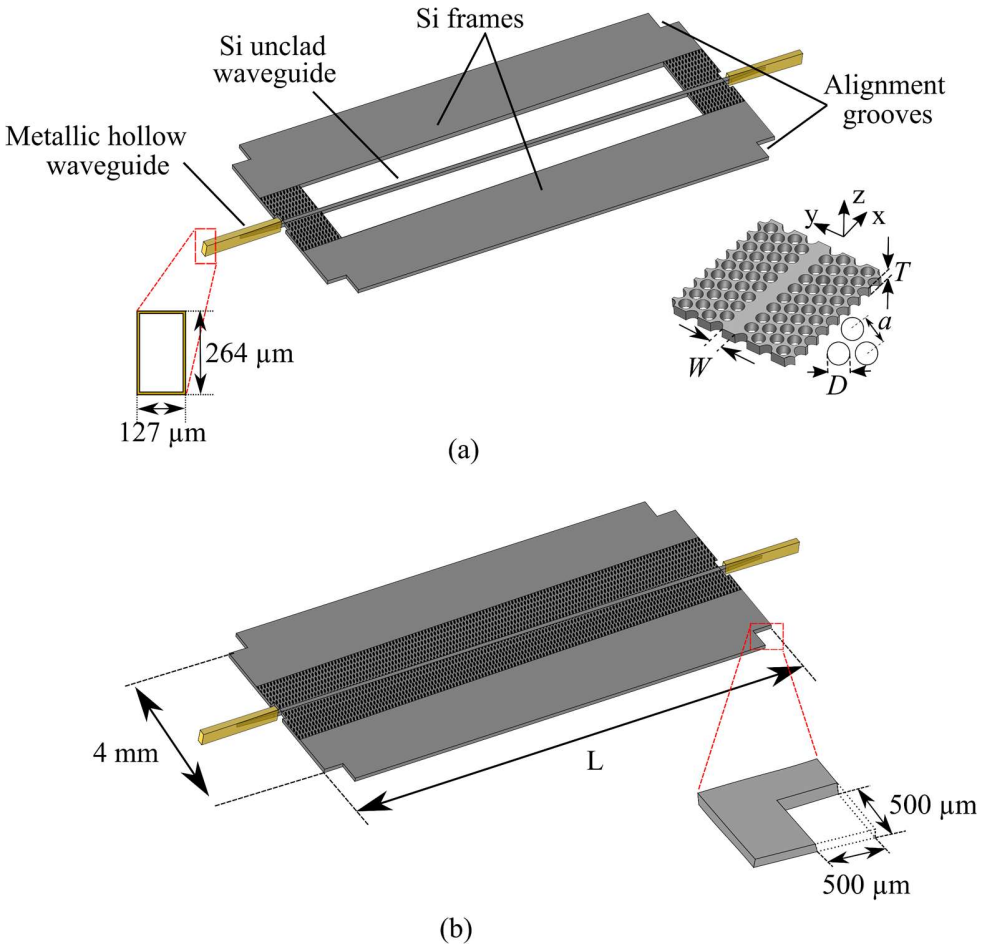

Figure 2.8 Designs of proposed dielectric waveguides: (a) Unclad waveguide; (b) EM waveguide; W = 100 µm, D = 35 µm, a = 45 µm and T = 80 µm.

2.1.4. Fabrication and experimental characterization

We fabricated unclad and EM waveguides with different lengths L (1, 2, 3, 4, and 5 cm). The waveguides were fabricated from high-resistivity float-zone intrinsic Si wafers with a nominal resistivity of >10kΩ-cm using deep reactive ion etching. The resulting unclad and EM waveguides are shown in Figure 2.9 (a) and Figure 2.9 (b), respectively. Micrographs are shown to highlight key sailing features such as EM sections and coupling linear tapers. We have estimated the operation of these waveguides through two measurement sets: The transmittance measurement and the estimation of the loss.

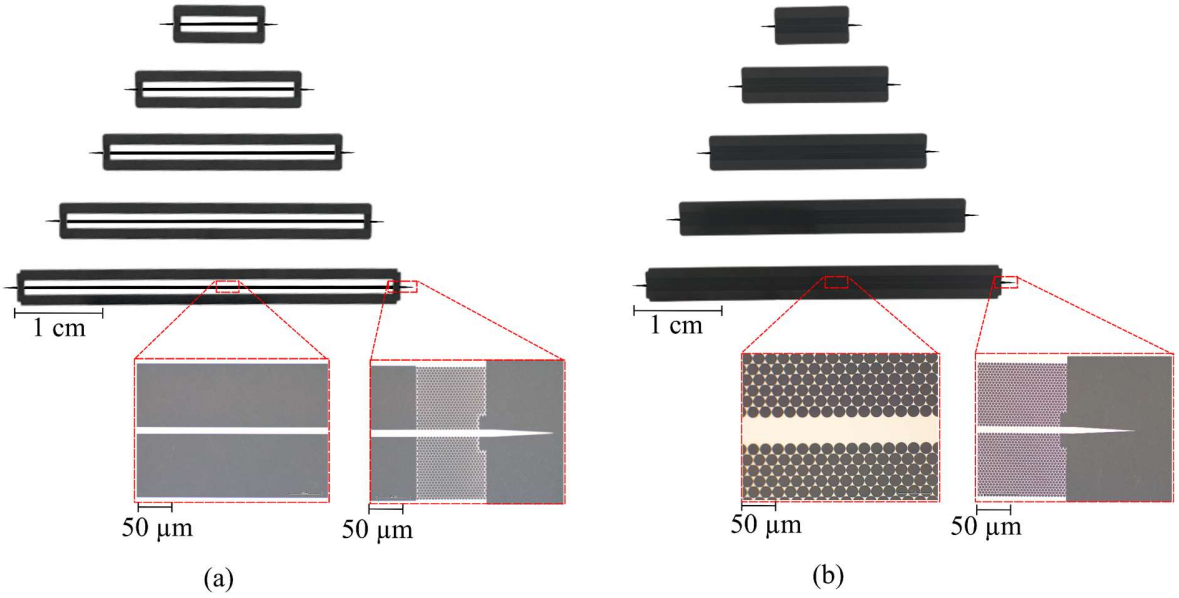

Figure 2.9. Fabricated waveguide samples with micrographs as an inset: (a) Unclad waveguides; (b) EM waveguides

2.1.5. Transmittance measurements

We measured the power transmission of these waveguides using the experimental setup shown in Figure 2.10. As shown in Figure 2.10 (a), the power transmission was probed by inserting linear tapers of the waveguides into metallic hollow waveguides. For the WR-1 band, the physical dimensions of the rectangular hollow waveguide are 127 µm × 254 µm; which targets the frequencies in 0.75 – 1.1 THz. The small dimensions of this waveguide can hinder accurate measurements in experiments and may pose a challenge. To overcome this issue, we

employed commercially available microscopes (DINO Lite), as shown in Figure 2.10 (b), to obtain a better view of the opening of the metallic hollow waveguides for the insertion of Si tapers. In addition, we have devised supporting jigs to help position the waveguide devices, assuring vertical alignment and 0-tilt, which has helped reduce imperfect alignment. The details of the design of the jigs and the assembly process are detailed in Appendix 1. Imperfect alignment between the Si tapers and the metallic hollow waveguide is the main cause of coupling losses. The metallic hollow waveguides interface with commercially available signal generators coupled with a multiplier to deliver THz signals in the 0.75 – 1.1 THz; that is the signal generator delivers millimeter waves into a 27-times multiplier which in turn delivers the THz waves into the waveguides. A THz range mixer was employed at the detection side to perform frequency down-conversion, producing microwave signals that were then processed by a spectrum analyzer.

Figure 2.11 shows the measured transmittances for the unclad (red) and EM (blue) waveguides. Each waveguide was measured five times, and for each measurement, the linear taper of the waveguide was removed from the hollow metallic waveguide on both the transmitter and receiver sides and then re-inserted. The standard deviation is used to derive error bars, which indicate the extent to which each measurement data point differs from the overall average. The error bar suggests minor differences between each measurement, which could be attributed to the positioning jigs that help secure the position of each sample between consecutive measurements. A shift in transmittance can be observed in both designs as the length of the waveguides, L changes. For the unclad waveguides, the transmittance is shifted from a minimum of -5 dB – Figure 2.11 (i) for the longest waveguide (5 cm) to 0 dB – Figure 2.11 (a) for the shortest (1 cm). In the case of EM waveguides, the power transmission was found to be ~ 1 dB better than that of unclad waveguides. Specifically, the transmittance shifted from 4 dB (Figure 2.11 (j)) for the longest waveguide (5 cm) to ~0 dB (Figure 2.11 (b)) for the shortest (1 cm). In some cases, the transmittance was found to be > 0 dB, which means that the power transmission is better when employing all-Si waveguides than when probing the reference measurement employing hollow metallic waveguides. This phenomenon has been observed previously in dielectric waveguides of this type in the WR-2.8 band, and this phenomenon can

be exacerbated in the WR-1 band [78]. However, this phenomenon can be possibly mitigated by averaging the measurements; to derive the propagation and coupling losses.

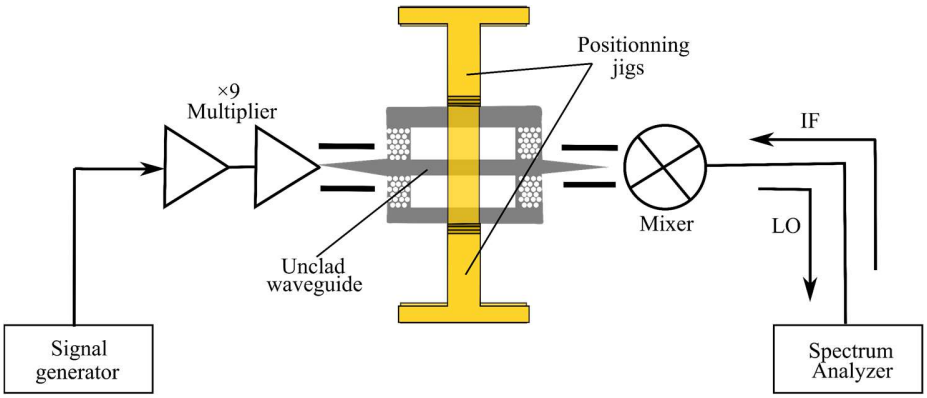

(a)

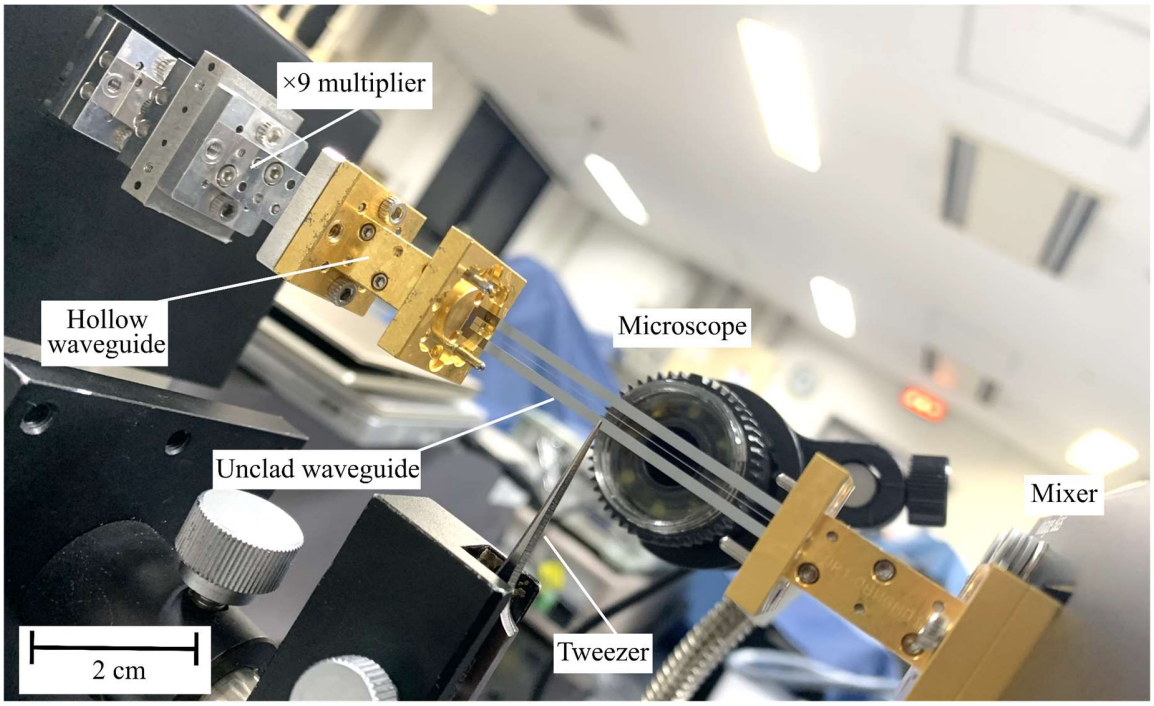

(b)

Figure 2.10. Experimental setup for the measurement of the transmittance: (a) Schematic of the setup; (b) Photograph of the setup.

2.1.6. Loss estimation of the dielectric waveguides

We probed five waveguides of different lengths for both the unclad and EM designs to derive propagation and coupling losses using the difference in power transmission. Specifically, the transmittance for each waveguide length was plotted as a function of the frequency. Thereafter, for each frequency point, the transmittance data points were fitted to a curve using the least squares method. The slope and intercept of the resulting curve are then used to estimate the propagation and coupling losses, that is, the propagation loss per unit length corresponds to the slope of the curve and the coupling loss to the intercept. The deduction of the propagation and coupling losses is illustrated in Figure 2.12 (a) and Figure 2.12 (b) for the unclad and EM waveguides, respectively. Figure 2.10 shows the measured and simulated propagation losses for both the unclad waveguides (red) and EM waveguides (blue). For the unclad waveguides, the simulated and measured propagation losses were in good agreement for the lower frequencies, up to ~0.9 THz. For the frequencies > 0.9 THz, the measured propagation loss is found to be ~ 0.3 dB on average higher than the simulated propagation loss. The results are shown in Figure 2.13 (a). This could be attributed to the difference in Si properties and the limitations of the fabrication foundries. The propagation loss of the EM waveguide is presented in Figure 2.13 (b), and the measured and simulated losses are observed to be in good agreement. The coupling loss of the unclad waveguide is shown in Figure 2.13 (c). The measured coupling loss was greater than the simulated coupling loss. The difference is negligible for lower frequencies up to 0.8 THz: and higher frequencies > 1.05 THz with a difference of ~ 0.2 dB. The difference in coupling is exacerbated around the center frequency of 0.925 THz, reaching ~0.4 dB as opposed to the good agreement for the EM waveguide, as shown in Figure 2.13 (d). This can be ascribed to the losses that occur at different interfaces of the unclad waveguide. Indeed, both the unclad and EM waveguides have linear tapers that serve as coupling interfaces with the metallic hollow waveguides, but the unclad waveguide has additional interfaces at the point where the EM section is interrupted, revealing the waveguide core as a single wire. This transition from EM to air creates reflections as a result of the impedance mismatch between the EM-clad waveguide section and the air-clad Si wire at both ends of the waveguide. These losses caused by the impedance mismatch can be higher for longer waveguides, as confirmed by the results shown in Figure 2.8. With a difference in coupling loss of ~0.4 dB, we can attribute a ~0.2 dB loss to each EM-unclad transition interface. In addition, the results revealed the very broadband

performance of these waveguides, as the 3-dB bandwidth was not encountered in the entire frequency range of interest, suggesting a bandwidth of ~350 GHz.

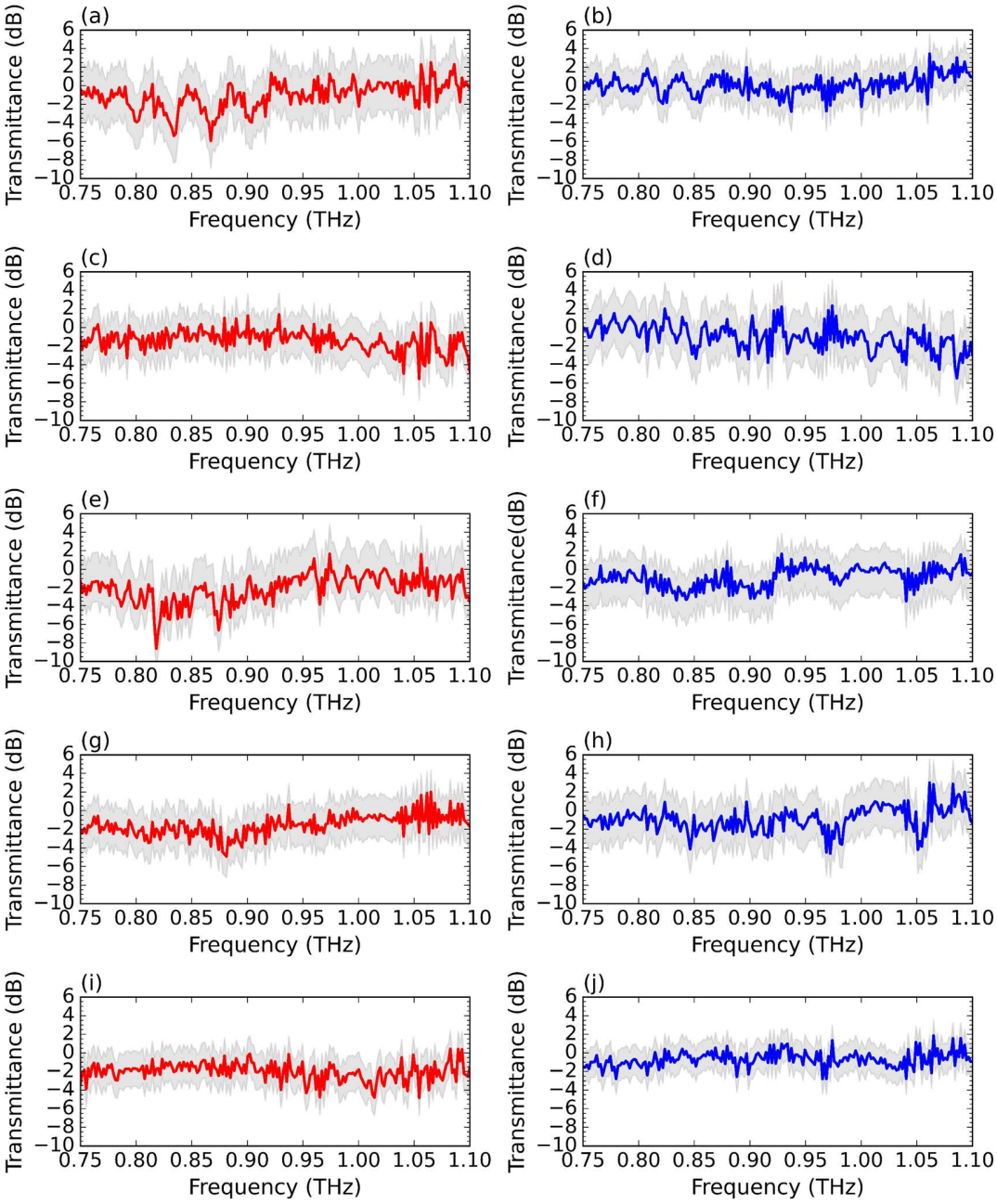

Figure 2.11. Measured transmittance of the fabricated unclad (red) and EM (blue) waveguides: (a-b) 1 cm; (c-d) 2 cm; (e-f) 3 cm; (g-h) 4 cm; (i-j) 5 cm.

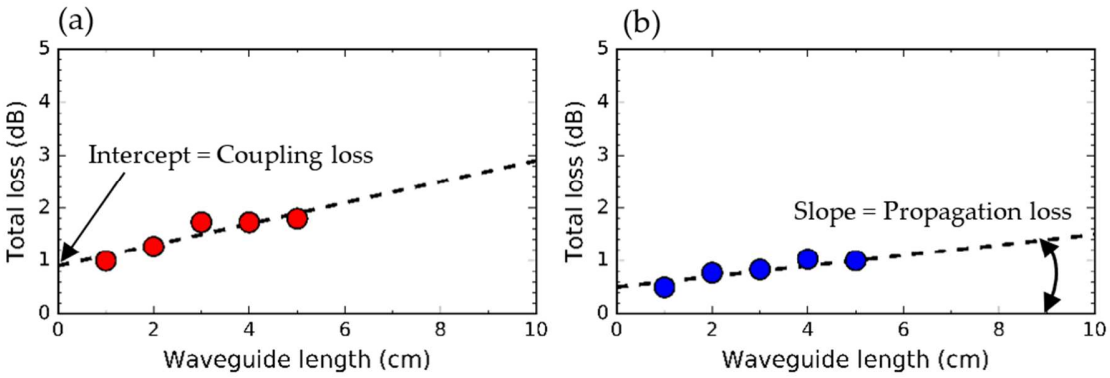

Figure 2.12. Measured total loss at 0.925 THz as a function of waveguide length: (a) Total loss estimation of unclad waveguide with 1.3 mm EM section; (b) Total loss estimation of EM waveguide. The propagation loss is defined using the slope of the fitted curve. The coupling loss is defined using the intercept of the fitted curve.

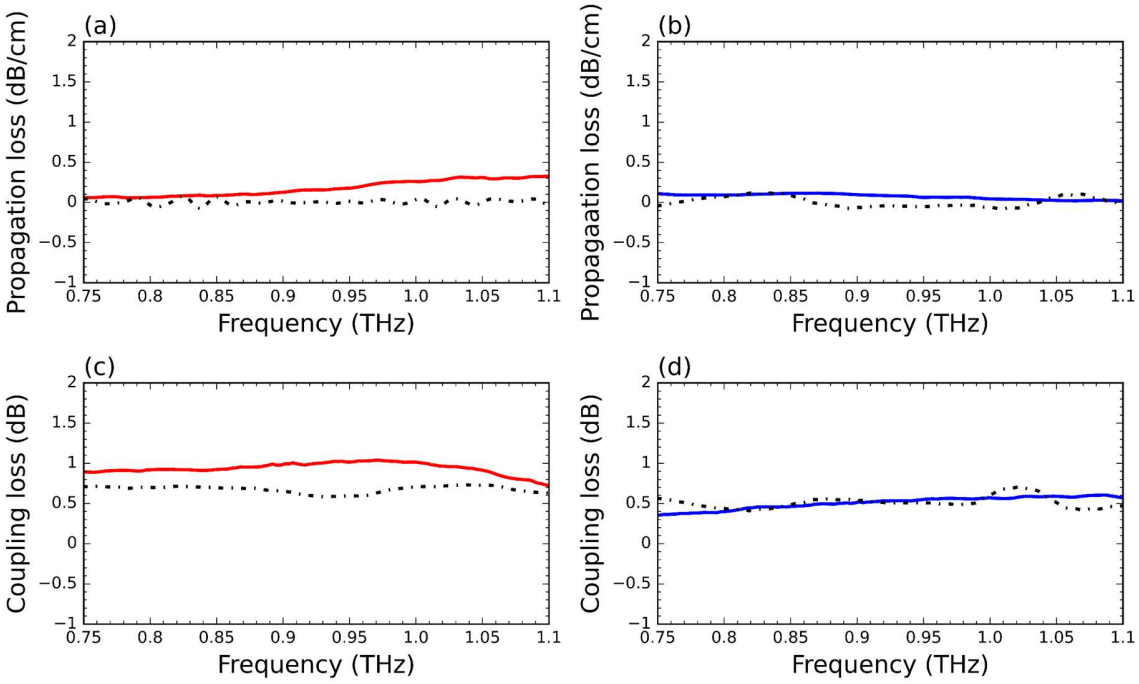

Figure 2.13. Measured (solid) and simulated (dashed) propagation loss and coupling loss: (a) Propagation loss of unclad waveguides; (b) Propagation loss of EM waveguide; (c) Coupling loss of unclad waveguide; (d) coupling loss of EM waveguide. Measured propagation loss and coupling loss for the unclad waveguide are higher than simulated results, which could be ascribed to the side walls roughness of the fabricated unclad waveguides, as opposed to ideal simulation models.

2.2. Comparison between EM waveguide and unclad waveguide

Table 2.1 summarizes the results of the two waveguides. EM waveguides achieved lower loss than unclad waveguides, with similar bandwidth of 350 GHz. The difference in loss performance could be ascribed to the structure of the unclad waveguide that resembles a Si wire. This means that the unclad waveguide is prone to a larger impact from the sidewall roughness of its waveguide core. Sidewall roughness is the source of significant losses in wire waveguides of this sort. These losses can be mitigated by improving the fabrication accuracy, tailored to structures with small dimensions as the waveguides studied in this thesis.

Despite the better performance of the EM waveguides, unclad waveguides are employed throughout this dissertation for the demonstration of THz applications. This is because unclad waveguides offer more flexibility for the realization of devices requiring drastic bending. For functional components such as diplexers and Y-junctions, the unclad waveguide offers more design flexibility than is not possible with a simple EM waveguide. With an EM waveguide, additional considerations for impedance matching would be required, to reduce the loss associated with the bends. This holds for photonic crystal waveguides as well. Indeed, a 60º bend in a photonic crystal waveguide accounts for ~0.5 dB loss [56]. This is higher than the demonstrated propagation loss of <0.1 dB/cm.

Table 2.1: Comparative performance of WR-1 band EM waveguide and unclad waveguide.

	EM	**Unclad**
Propagation loss (dB/cm)	<0.1	0.15 dB
Coupling loss	0.5	0.9
3dB-bandwidth (GHz)	350	350
Fabrication Precision accuracy required	High	Medium

2.3. Application I: Packaged dielectric waveguide modules

Packaging remains a major bottleneck for many electrical and optical systems. This remains true for THz range devices that tend to be fragile. In this section, we propose a packaging methodology for all-dielectric THz waveguides, that provide both protection and efficient interfaces for coupling with measurement equipment.

2.3.1. Principle of waveguide packaged modules

The main concept of the proposed modules is illustrated in Figure 2.14. An all-Si device that operates as the central component was encapsulated in metallic packaging. The Si device is terminated by transition interfaces that serve as interfaces with metallic packaging while ensuring a low insertion loss. The transition interface also serves to secure the device onto the packaging, ensuring safety and perfect alignment.

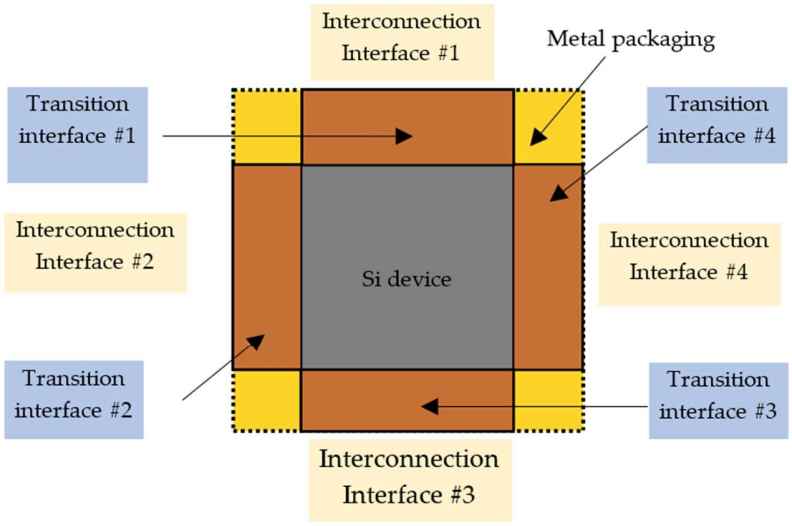

Figure 2.14. Concept of the proposed module, highlighting the transition and connection interfaces

2.3.2. Design and fabrication

Transition interfaces play a crucial role in reducing the impact of metallic packaging on the inherent behavior of the device. In practice, transition interfaces can be realized by employing photonic crystals [94] and EM [66], as well as by gradual hole density [95]. Either

technique can be considered while considering various performance indices of the waveguide, such as reflection, bandwidth, and fabrication limitations on the minimal manufacturable hole size. Transition interfaces usually incorporate all-Si tapered structures for smooth transitions. Among various taper shapes, linear tapers have been proven to allow gradual transmission of THz waves with < 0.2 dB coupling loss [56]. Linear tapers can also be implemented with a specific hole arrangement to improve matching at the interface where the taper contacts other THz-range components [74]. The transition interfaces are, in turn, terminated by interconnection interfaces that serve to interconnect the module with other THz-range components such as THz sources and detectors. In this study, the interconnection interface is an I/O interface compatible with the WR-1 standard flange. The modules are realized by devising metallic packaging to house the unclad and EM waveguides, as shown in Figure 2.5. Metallic packaging has an I/O interface that is compatible with the WR-1 standard hollow waveguide. The design of the module is illustrated in Figure 2.15.

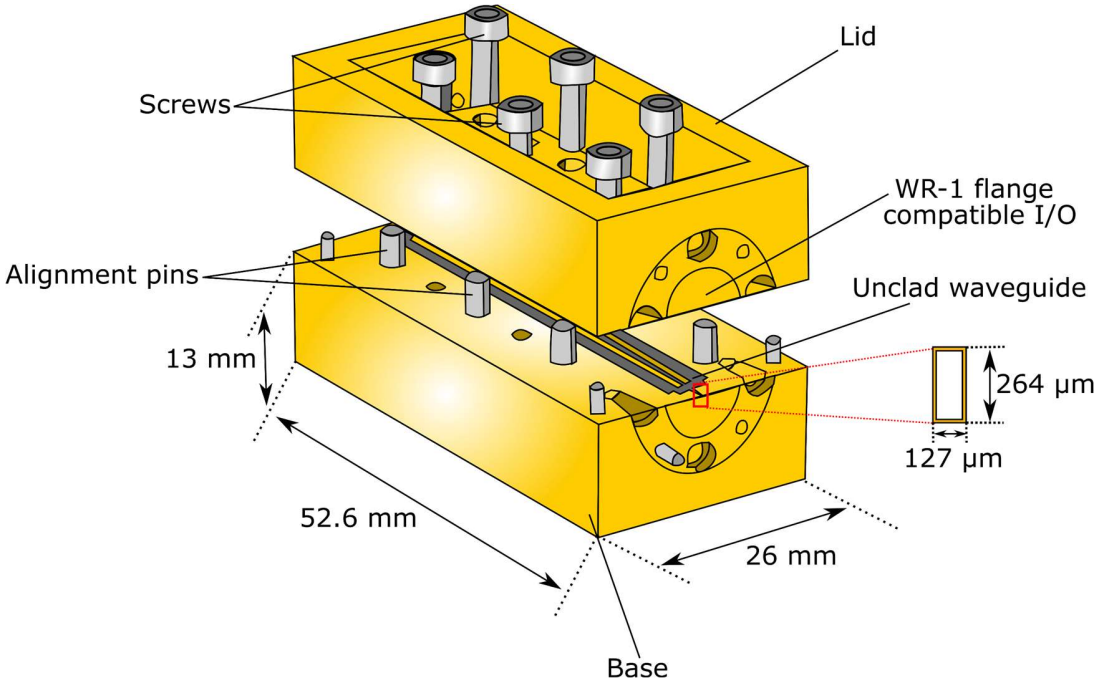

Figure 2.15. Design of metallic packaging for the waveguide modules. The base incorporates pins of different sizes, for tighter assembly of the module.

The packaging is 56.2 mm 26.0 mm × 26.0 mm and is made of copper with gold plating. The module comprises a base and a lid. A 2.3-mm-deep trench is carved out of the base, leaving

a void wide enough to prevent the packing from impacting the inherent function of the waveguide core. The base is also designed to house the waveguide while ensuring perfect alignment with the integrated WR-1 hollow waveguide track. This is achieved by incorporating a shelf into the base on which the waveguide rested. The shelf has a depth of 40 μm, which is half the thickness of the waveguide. This is because the lid is identical to the base; therefore, there is a 40 μm shelf in the lid as well. The width of the shelf matched that of the waveguides, including the frames, which is 5 mm. The modules also incorporate knobs that match the alignment grooves of the waveguide, thereby helping to fix the waveguide inside the module. For the assembly, each waveguide is carefully placed on the base such that the tapers sat in the hollow waveguide section of the metallic packaging. This is achieved by employing high-resolution microscopes to improve alignment accuracy. Employing microscopes is necessary because the dimensions in this band are extremely small. Once the waveguide is secured to the base, the lid is affixed with screws. The resulting module is extremely compact, and lightweight, and can easily be connected to other THz-range components via the WR-1 band I/O interface using screws to ensure perfect alignment, which is crucial for reducing insertion loss.

We designed and fabricated two metallic packagings and assembled an unclad waveguide module and an EM waveguide module, as shown in Figure 2.16 (a) and Figure 2.16 (b), respectively. The modules are made of aluminum, with gold plating. Micrographs are also shown and the knobs of the base fit perfectly into the grooves of the waveguides. Additional micrographs are presented to show the positioning of the linear tapers within WR-1 standard hollow metallic waveguides. We also fabricated a 5-cm long standard hollow metallic waveguide module, as shown in Figure 2.16 (c), to investigate its performance in comparison with the unclad waveguide module and EM waveguide module.

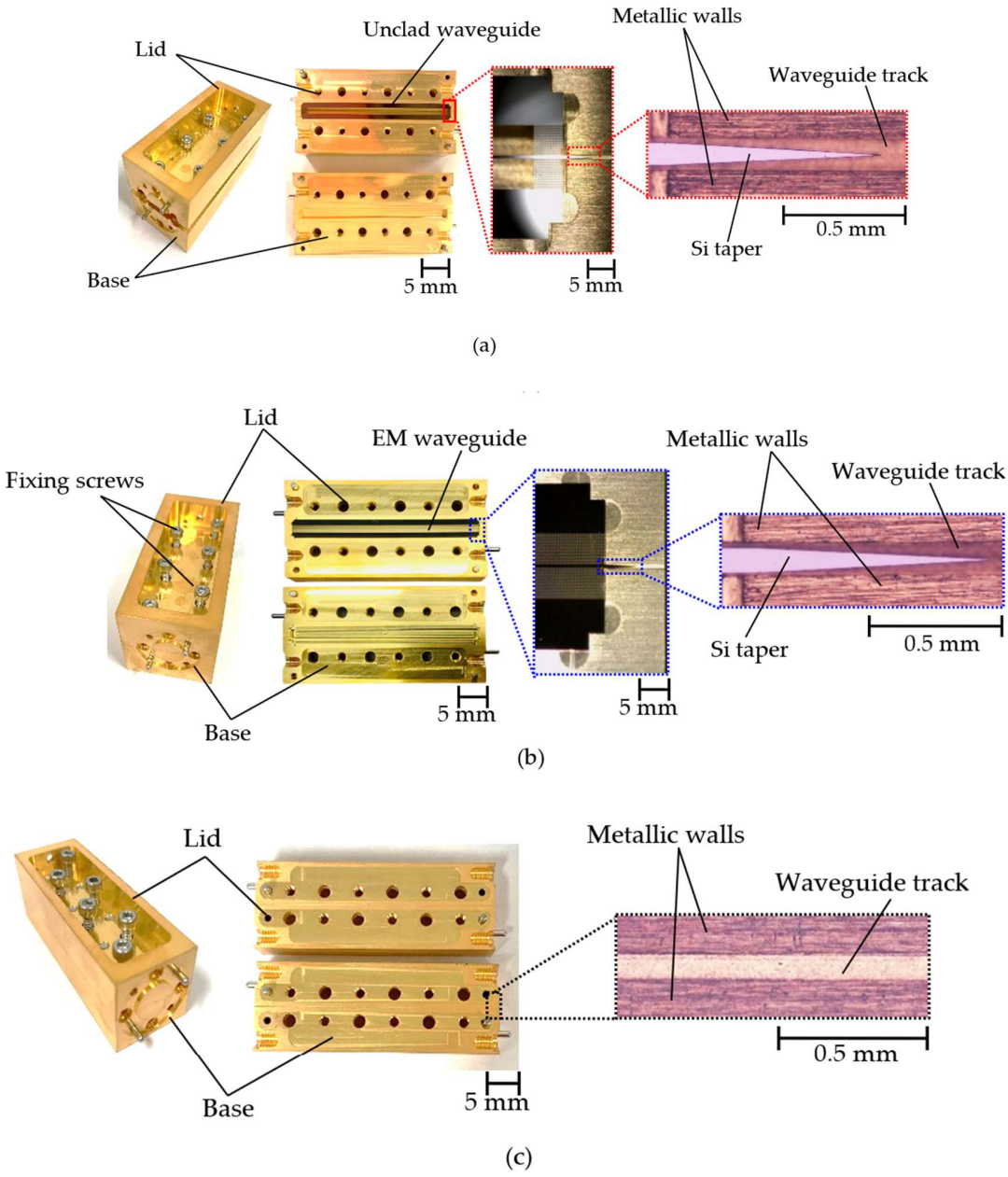

Figure 2.16. Fabricated modules and experimental setup: (a) Unclad waveguide module; (b) EM waveguide module; (c) Hollow metallic waveguide.

2.3.3. Measurement

The power transmission of the three modules was probed using a similar system, as shown in Figure 2.10. A photograph of the experimental setup is shown in Figure 2.17. Figure 2.18 shows the simulated (dashed line) and measured (solid line) transmittances of the modules. The transmittance of the unclad waveguide module is shown in red, that of the EM waveguide module in blue, and that of the metallic hollow waveguide in black. The measured and simulated transmittances of the EM waveguide module are in good agreement. In the case of the unclad waveguide module, the measured transmittance is in good agreement with the simulated transmittance for frequencies up to 0.95 THz. The transmittance is ~ -2 dB for both simulated and measured across 0.75 – 1.1 THz. For frequencies > 0.95 THz, the difference between the measure transmittance and simulated transmittance increases from 0 dB at ~0.955 THz to reaching a maximum of ~ 0.8 dB at 1.05 THz, and finally, 0.4 dB difference at 1.1 THz. For the hollow waveguide module, the trends of both simulated and measured transmittance are the same, with a difference of 0.4 dB at 0.75 THz, slowing decreasing to 0 dB at ~1.0 THz.

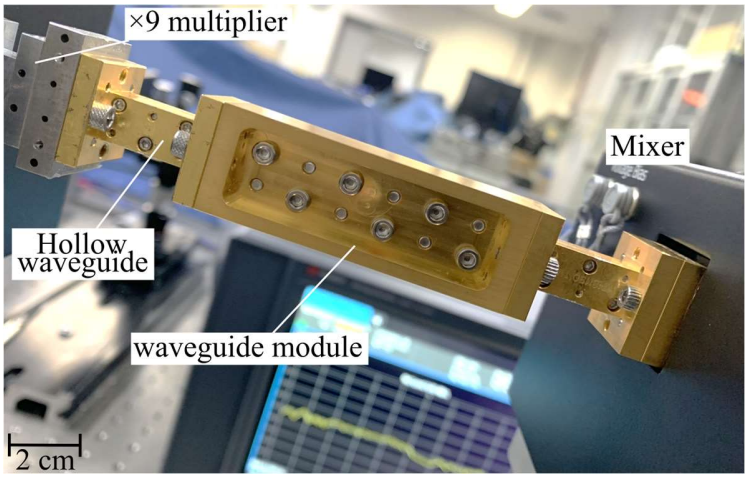

Figure 2.17 Experimental setup for the measurement of the transmittance of the modules.

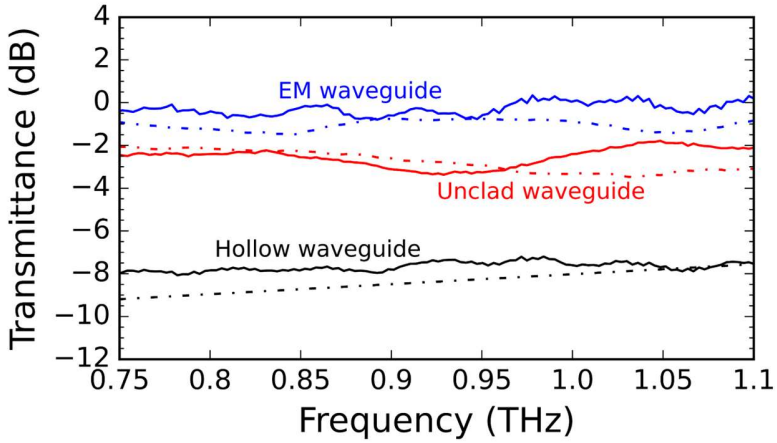

Figure 2.18 Measured transmittance for EM waveguide module (blue), unclad waveguide module (red), and hollow waveguide module (black)

Probing the power transmission of these modules yielded results that were very close to the theoretical approximations. The unclad module has a ~6 dB loss improvement over the hollow waveguide module and ~2 dB loss compared to the EM module. As discussed previously, this is due to the increased coupling loss of the unclad waveguide at the interface where the EM section is interrupted. The EM waveguide module has very little loss and exhibits a ~ 8 dB loss improvement over the hollow waveguide module. Both the unclad waveguide module and EM waveguide module demonstrate superior performance compared to the metallic hollow waveguide module.

2.4. Application II: Packaged Y-junction module for improved THz-range imaging based on unclad waveguide

2.4.1 Design of Y-junction

To demonstrate the versatility of unclad waveguides, we designed the functional Y-junction component based on the unclad waveguide as illustrated in Figure 2.19. An EM section is used to implement the ports of the Y-junction. The dimensions of the EM section are kept identical to the EM waveguides designed as described in Figure 2.8. That is, the hole diameter *d* is 35 μm, and the lattice constant a is 45 μm. Each EM waveguide extends into an unclad

waveguide of core W = 80 µm. The waveguide core was reduced by 20 µm as opposed to the unclad waveguide described in 2.1. This was done to facilitate the insertion of the linear tapers into the hollow waveguides in experiments.

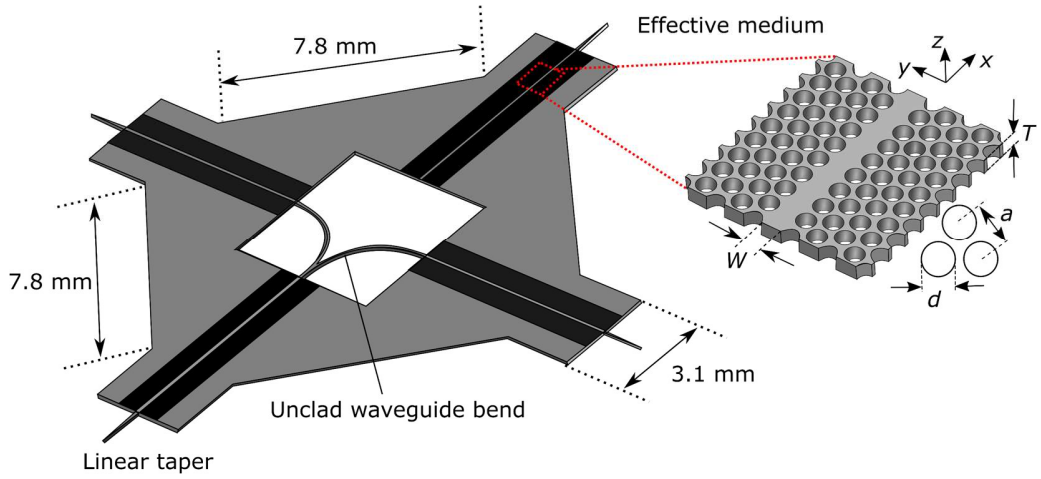

Figure 2.19 Design of proposed Y-branch with the EM section as inset. W = 80 µm, T = 80 µm, D = 45 µm, P = 45 µm.

We fabricated the Y-junction and assembled the Y-junction module with packaging like that described in 2.3. The module is 27 mm × 27 mm × 27 mm and was made of copper with gold plating. The assembly was performed in a similar manner, employing tweezers to place the all-Si component onto the base of the packaging, and then the lid was affixed using screws. The assembled module is shown in Figure 2.20, with a micrograph of the Si taper within the hollow metallic waveguide. Figure 2.20.

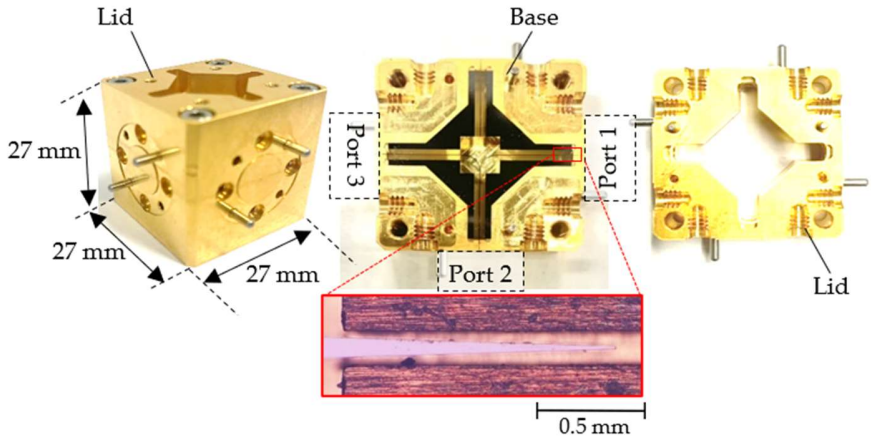

Figure 2.20 Fabricated Y-junction module and assembly

2.4.2. Characterization and imaging demonstration

2.4.2.1. Characterization

Figure 2.21 (a), (c) and Figure 2.21 (b), (e) show the experimental setup for measuring transmittance S21 and isolation S31, respectively. The results of these measurements are shown in Figure 2.22. Both the simulated (dashed line) and measured (solid line) transmittance and isolation are presented. The measured and simulated transmittances (red) are in good agreement, with very little discrepancy between the lower and upper ends of the entire band of interest. The measured isolation is found to be better than the simulated isolation. Theoretically, the lower the isolation, the better. When isolation is lower, very little power deviates from Port 1 to Port 2, causing most of the power to be transmitted. The isolation in the measurement is found to be ~ -26 dB at 0.75 THz, against -20 dB in simulation. However, for frequencies > 0.85 THz, the simulated and measured isolations are in acceptable agreement, mostly around -25 dB. The discrepancy for the lower frequency is attributed to minor fabricator errors in the unclad section leading to port 3 of the module. As shown in Figures 2.4 (c) and 2.4 (d), the unclad waveguide performance is strongly dependent on the waveguide width. A waveguide width of 100 µm has very little loss, with a transmittance of ~ -0.3 dB at 0.75 THz. In comparison, a waveguide width of 80 µm has a transmittance of ~1.8 dB at 0.75 THz. This significant difference could affect the overall performance of the Y-junction. Looking at the trends for the transmittance for

different values of W, it can be deduced that the transmittance worsens as the waveguide width decreases. As such, a waveguide width $W < 80$ μm would cause the transmittance to be <-2 dB. Because of the very small dimensions of the Y-junction, fabrication errors occurred, resulting in an increased measured loss at Port 3. In addition, as established through measurements, unclad waveguides have increased loss caused by additional coupling loss at the interface where the EM is interrupted, revealing the waveguide core. For the straight waveguide, two such interfaces exist, accounting for a loss of ~0.4 dB. In the case of the Y-junction, there are three such interfaces, which theoretically should account for a total coupling loss of 0.6 dB. Considering the circular bending, these losses could have increased in the fabricated device. This phenomenon stresses the requirement for more accurate machining and is a major hindrance to the currently available techniques.

2.4.2.2. Demonstration of THz imaging

THz waves are well-suited for imaging applications. THz waves can penetrate a wide variety of non-conducting materials such as wood, paper, cardboard, plastic, and ceramic. This has allowed key novel applications in healthcare for single-strand DNA detection [96] and security for enhanced non-invasive detection of concealed weapons [91]. Other notable applications have been realized in industrial inspections for the detection of defects [97]. However, imaging applications have been restricted by the physically large size of the systems because of the need for components, such as splitters and lenses. Employing a large number of individual components increases the system complexity and imposes a more stringent alignment for optical paths. More practical imaging systems may require a reduction in the physical size and complexity as more compact systems can allow large-scale hybrid integration and open the door to novel applications. Recent research has sought hybrid integration with flat optics, allowing the realization of all-Si lenses [73], [82], beam splitters [98], and filters [70]. This has significantly reduced the size and complexity of imaging systems, resulting in compact designs that can be handheld [76], enabling applications at higher THz frequencies, and novel applications such as drone-borne technology.

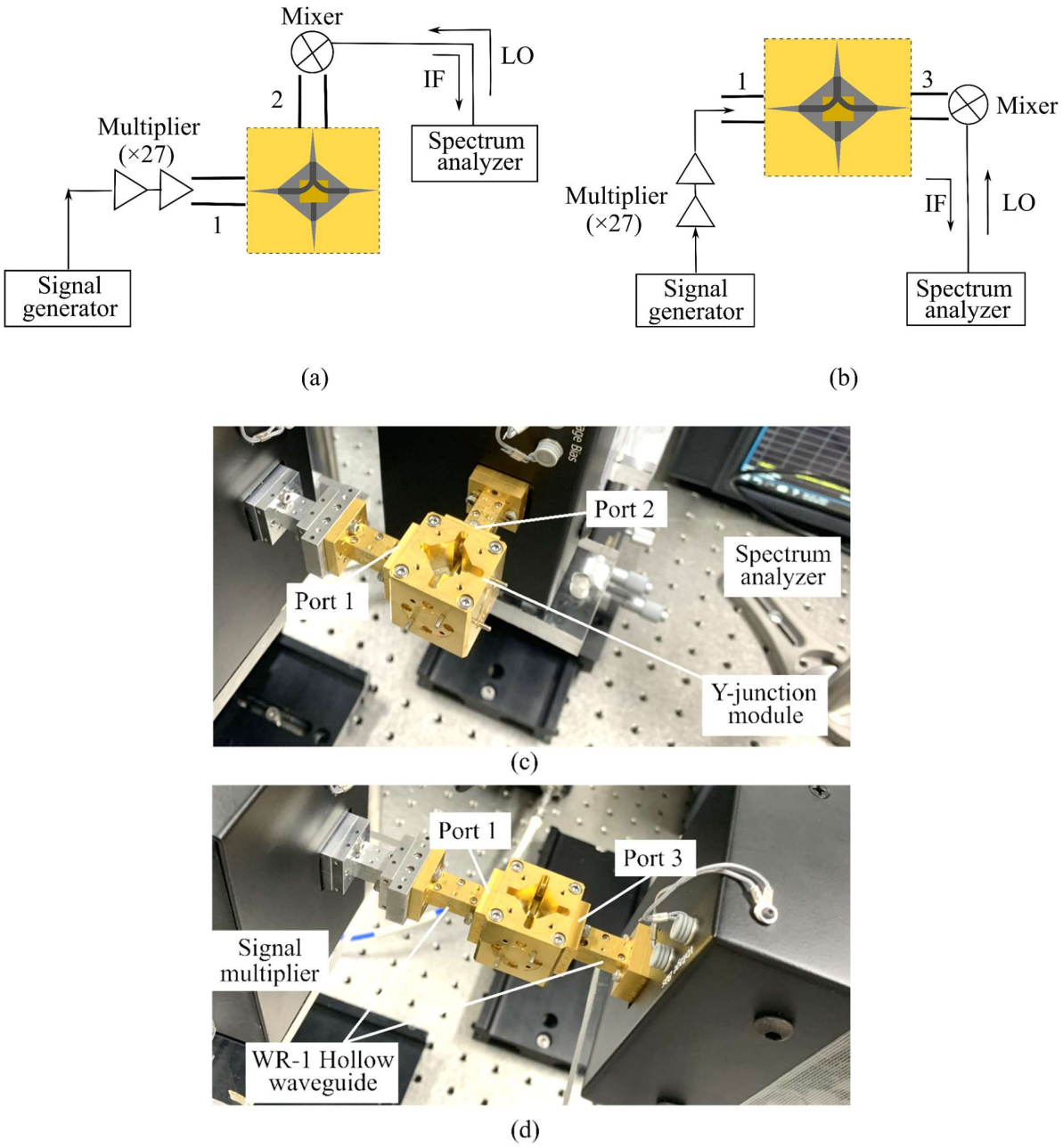

Figure 2.21 Experimental setup for the power transmission measurement: (a) block diagram for the measurement of S21; (b) Diagram for the measurement of S31; (c) Photograph of experiments setup for the measurement of S21; (d) Photograph of the experimental set up for the measurement of S31.

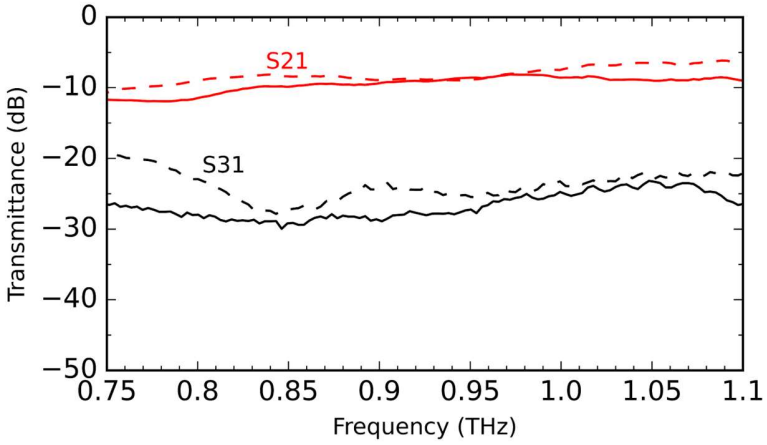

Figure 2.22 Measured S21 (red) and S31 (black) of the proposed Y-branch (dashed lines) and Y-branch module (solid lines).

Having realized and demonstrated the WR-1 band Y-junction module, we attempt to demonstrate the practical imaging applications of this module. Targeting the frequencies in the 0.75 – 1.1 THz is a step toward high-resolution imaging applications. To this end, we employ the configuration shown in Figure 2.23 (a). At the transmitter side, a ~35.4 GHz millimeter wave signal that is modulated using a 100 kHz signal is injected into an ×27 multiplier to deliver THz waves in the WR-1 band. The THz signal is then injected into the Y-junction module through Port 1 and radiated into free space through a horn antenna attached to Port 2. Two parabolic mirrors, one that serves as a collimating mirror and the other as a galvanometer mirror, are employed. The radiated signal from the horn is collimated by the first mirror, which ricochets off the second mirror to reach the target. The target is attached to a motorized stage that allows both x-axis and z-axis scanning. On the receiver side, the residual signal from the target is detected by a Schottky barrier diode (SBD) and measured by a digital multimeter (DMM) after lock-in detection. Figure 2.23 (b) shows a photograph of the imaging experimental setup with the Y-junction module as an inset.

The imaging results are shown in Figure 2.24. Figure 2.24 (a) shows the imaging results for a commercially available test target with paper on top to reproduce a real-life obstacle. The test target was scanned at a resolution of 0.28 mm. A scanning resolution of 0.28 mm is sufficient for the demonstration of THz imaging. The results of the imaging of an integrated chip card are presented in Figure 2.24 (b), revealing the internal circuit that lies beneath the

cover of the IC card. The imaging results indicate that THz waves can penetrate nonconducting materials.

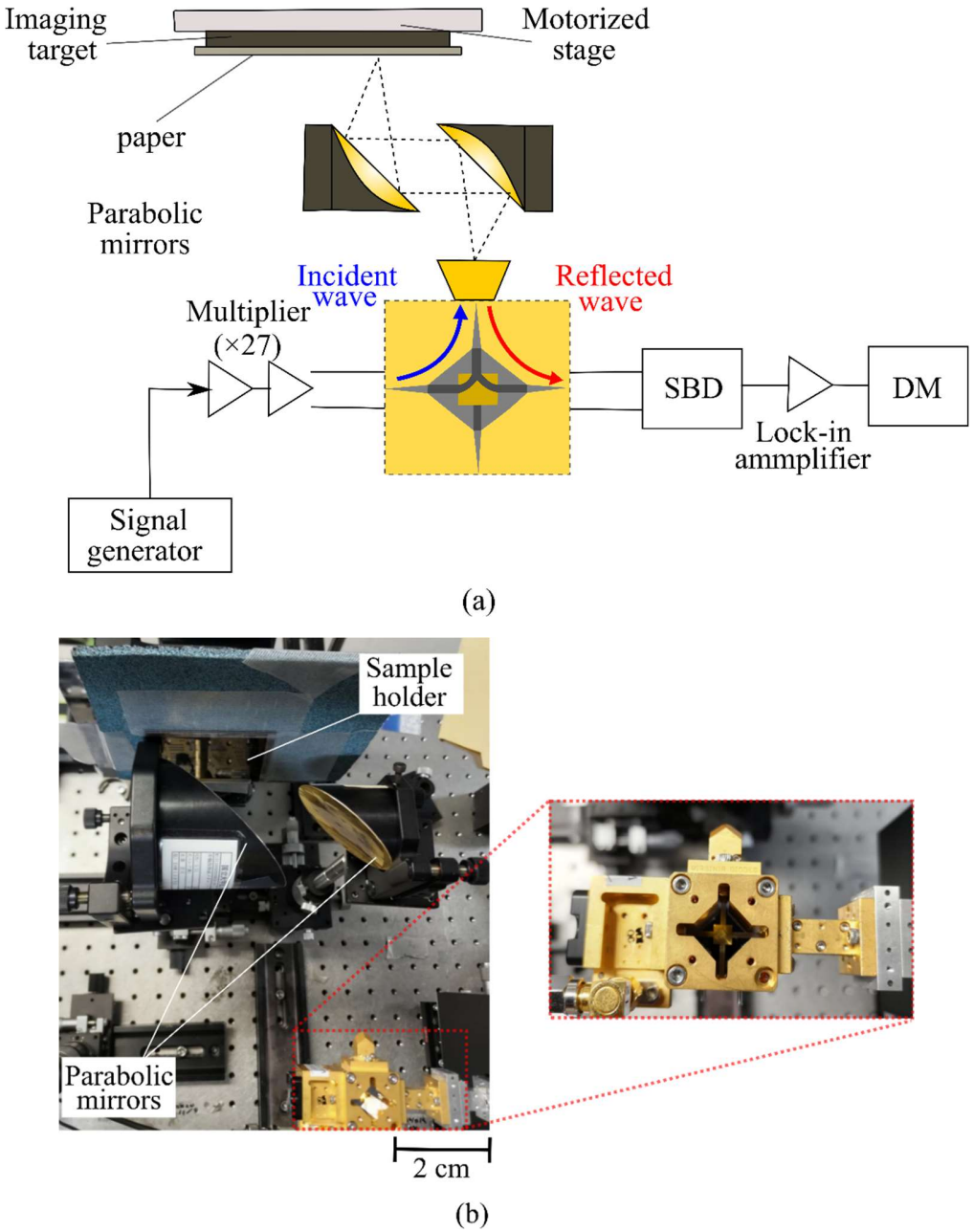

Figure 2.23 Imaging experimental setup: (a) Block diagram of the setup; (b) Photograph of the measurement showing the Y-branch module as inset.

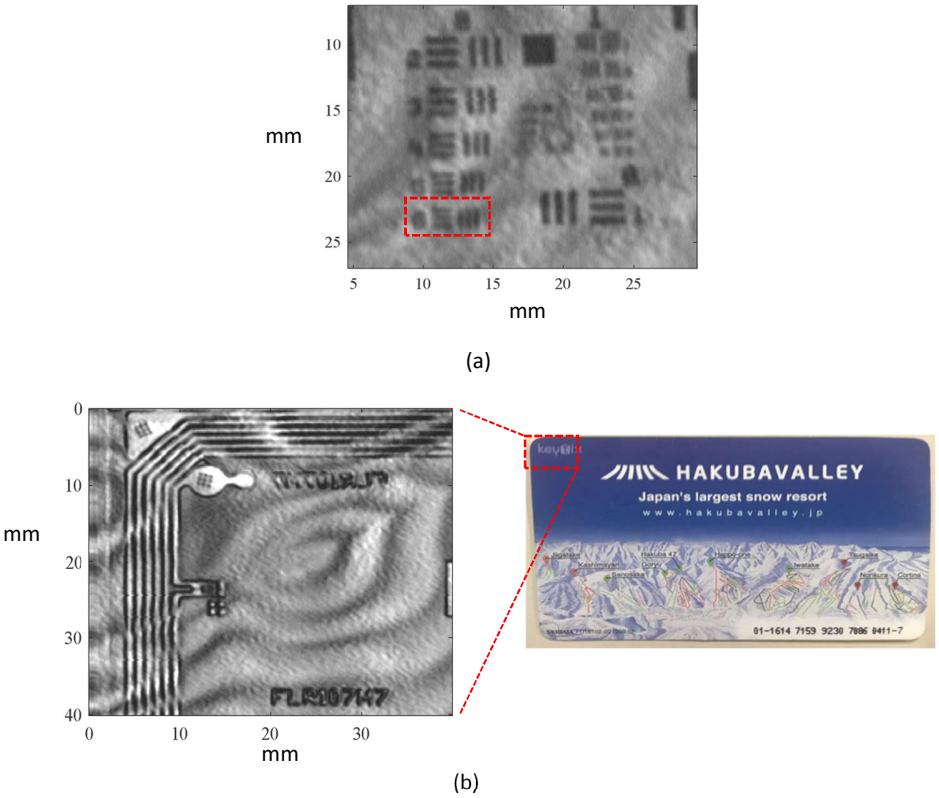

Figure 2.24 Imaging results at 0.957 THz: (a) Imaging of test target without paper; (b); (b) Imaging results of an IC card.

2.5. Application III: WR-1 band high-precision packaged variable attenuator.

Attenuators are fundamental components required for the safety of test equipment. Previous studies have reported a 60 dB attenuation range in 170 – 260 GHz [99]. The proposed attenuator is based on the interaction between the propagation waveguide mode and the photogenerated free carriers in a high-resistivity Si waveguide. That is, when intrinsic Si is illuminated by a light-emitting diode, the Si waveguide becomes a lossy dielectric creating an attenuation. This is because an illuminated Si waveguide changes the inherent properties of the waveguide including the conductivity, relative permittivity, and loss tangent. Different levels of attenuation can be achieved by varying the light intensity. The attenuation range can be further increased to over 60 dB, by targeting operation in the WR-1 band, based on the Si

waveguides presented in this thesis. In addition, by leveraging the packaging technologies introduced in this thesis for dielectric waveguides, it is possible to realize a compact packaged attenuator module. In addition, the precision control of the attenuation can be controlled by integrated millimeter calipers as shown in figure 2.25.

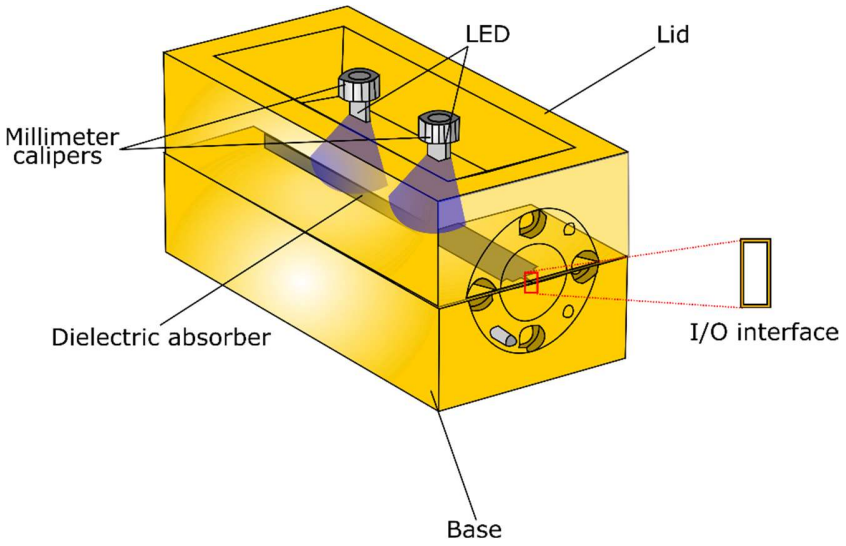

Figure 2.25: Concept of WR-1 band high-precision variable attenuator.

Chapter 3

Dual polarization operation in THz range devices based on silicon waveguides towards higher data rates communications

The improvement of data throughput has been a motivation for extensive research on techniques to improve the link budget of communication channels to achieve high data rates. Some research has focused on reducing losses, and other targeted techniques such as frequency division multiplexing to increase many folds the capacity of transmission channels. Some of those techniques have reported great data throughput improvements. Yet, there is still an opportunity for improvements as we present in this section, with the novel approach of employing dual polarizations.

3.1 Dual polarization over an unclad waveguide

Advances in photonic devices have enabled the development of several dielectric waveguides, such as photonic crystal, EM, and wire waveguides, with no cladding. These waveguides have reported low losses of less than 0.1, 0.05, and 0.1 dB/cm for photonic crystal [56], EM [66], and unclad waveguides [78], [100], respectively. THz-range dielectric

waveguides have been employed in high-resolution imaging [77], sensing [101], ranging, and communication applications [102]. However, the limitations of state-of-the-art equipment limit the highest achievable data rates in the THz region. This is because current systems and interconnects suffer from inherent attenuation, dispersion losses, and limited available power of the signal generators and detector sensitivity [10] as illustrated in Figure 3.1. Figure 3.1 shows the trends of output power (Figure 3.1 (a)) and responsivity (Figure 3.1 (b)) of existing signal generators and detectors as reported by Virginia Diodes Inc., and it can be observed that the responsivity is decreased from 2.8 V/W at 0.2 THz to 0.7 V/W at ~0.9 THz [103]. For the available power of the signal generator, the power is decreased from 15 dBm at 0.2 THz to ~22 dBm at 0.9 THz [104]. However, future metaverse applications and high-computational data centers will require even higher data rates [54]. Therefore, it is crucial to implement techniques that enable higher channel capacities and bypass system limitations in terms of sensitivity and output power. It is common practice to employ frequency multiplexing to increase the highest achievable data rates, however, this renders communications systems bulky and complex, with a lot of individual components. With the dual polarization operation, the highest data rates can be achieved with simplified components such as a Si wire.

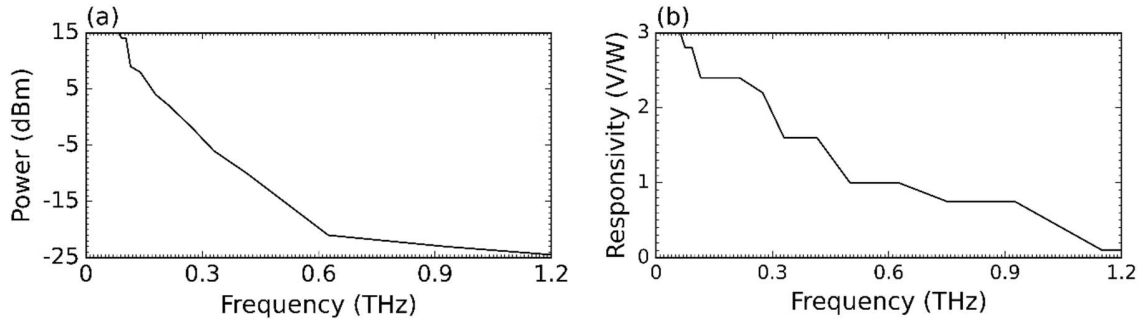

Figure 3.1: (a) Output power of off-the-shelf signal generators from VDI © showing the decreasing output power as the frequency increases, (b) sensitivity of off-the-shelf detectors by VDI © showing reduced sensitivity at higher frequencies.

3.1.1 Characterization of the unclad waveguides

Previous studies have focused solely on investigating the polarization purity of dielectric waveguides by analyzing the cross-polarization phenomenon within them [105]. In this study, we investigate orthogonal polarization over a dielectric wire waveguide to achieve higher

aggregate data rates in the THz region. Such a dual-polarization feature has not yet been applied to THz Si platforms. It can offer more flexibility and bypass system limitations for achieving higher data rates.

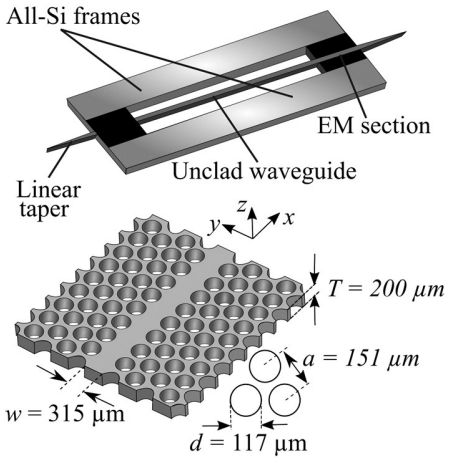

Figure 3.2: Design of the unclad Si wire waveguide with an EM section.

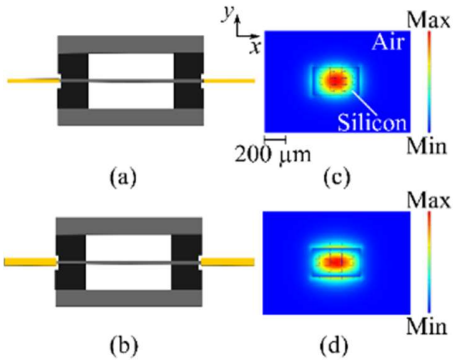

Figure 3.3: Dual-polarisation configuration: (a) E*x* excitation, (b) E*y* excitation, (c) E*x* mode, (d) E*y* mode.

To validate the proposed dual orthogonal polarization, we designed and investigated a dielectric unclad waveguide, which is shown in Figure 3.2. It comprises a waveguide core in a wire shape and an EM section composed of a Si slab perforated with an array of through-holes. A high-resistivity (>10 kΩcm) Si with a relative permittivity of 11.68 was employed to considerably lower both loss and dispersion. This is because the absorption loss in high-resistivity Si decreases with frequency owing to the reduction in free carriers. EM sections of a

finite length were used in the dielectric waveguide design to implement the supporting structures that protect the waveguide core, and for practicality and ease of handling during the experiments. The Si wire waveguide was terminated at either end using linear tapers that served as transition interfaces and coupling structures with metallic hollow waveguides. Linear tapers of this type have been reported to couple well with hollow metallic waveguides, which are necessary for interconnection with measurement equipment. The salient parameters of the waveguide were obtained by considering the desired operation band of the waveguide and the physical limitations on the minimum manufacturable dimensions. The EM sections are 3.5 mm long and 6.5 mm wide, and each linear taper is 3 mm long. The waveguide track is 336 μm wide, the hole diameter is 117 μm, and the hole pitch is 150 μm. The waveguide simulations were conducted in the CST Studio Suite 2021® using the configurations illustrated in Figure 3.3, which shows two configurations for the fundamental mode excitation of the unclad Si wire waveguide. Figure 3.3 (a) shows the *Ex* mode excitation, wherein the electric field is orthogonal to the unclad waveguide, and Figure. 3.3 (b) shows the transverse E_y mode excitation. Figures. 3.3 (c) and Figure 3.3 (d) show the modes profiles of E_x and E_y, respectively. It is evident that in the E_x mode, THz waves are mostly confined to the Si region, whereas in E_y, evanescent fields couple into the surrounding air. Consequently, an unclad Si wire waveguide could be employed to realize a dual-polarization THz-range link. It is noteworthy, that the investigations of the dual polarization using the unclad waveguide remain true with an EM waveguide of the same values of $w = 336$ μm, $d = 117$ μm, and $a = 151$ μm. We investigated the dispersion profile of both designs, to confirm comparable performance.

In addition to the E-field distributions, we analyze the modal profile of the waveguides in terms of propagation constant. We consider two waveguide designs including EM and unclad, as discussed in Chapter 2 of this dissertation. The results are presented in Figure 3.4 and Figure 3.5 for the propagation constants and modal index, respectively. The analysis reveals that both the unclad design (red) and EM design (blue) exhibit tight wave confinement, with the dispersion graphs (solid) well above the curve for the light in free space (dotted). This holds truer for the E_x polarization which exhibits better dispersion than the E_y polarization. With the modal index, we derived the 3dB-dispersion bandwidth as shown in Figure 3.6 for the unclad model, which we will employ in further demonstrations. Figure 3.6 shows that the dispersion

bandwidth of the E_x polarization (red) is better than that of the E_x polarization. That is, for the E_x polarization, the 3-dB dispersion bandwidth is ~120 GHz in 320 – 340 GHz, against ~70 GHz for the E_y polarization. This accounts for a bandwidth difference of 50 GHz, which could be attributed to the differences between the width and height of the waveguide core, and between the in-plane and out-of-plane claddings [106].

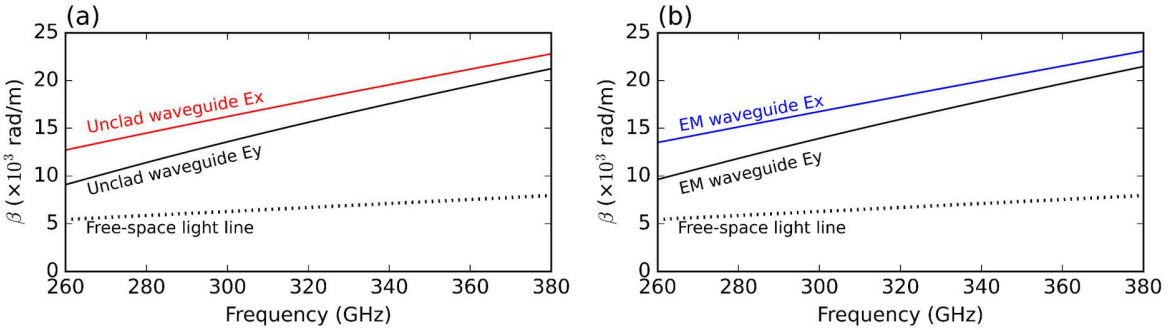

Figure 3.4: Propagation constants for unclad type waveguide (a) and EM type waveguide (b). The dispersion curves are shown in solid lines, and the light line in free space is shown in dashed lines. The E_y polarization is shown in black, whereas the E_x polarization is shown in red and blue for the unclad and EM models, respectively.

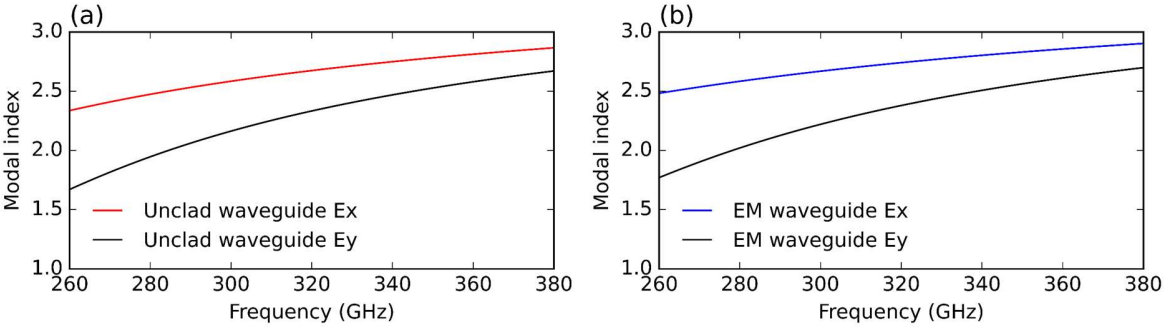

Figure 3.5: Effective index for unclad type waveguide (a) and EM type waveguide (b). The E_y polarization is shown in black, whereas the E_x polarization is shown in red and blue for the unclad and EM models, respectively.

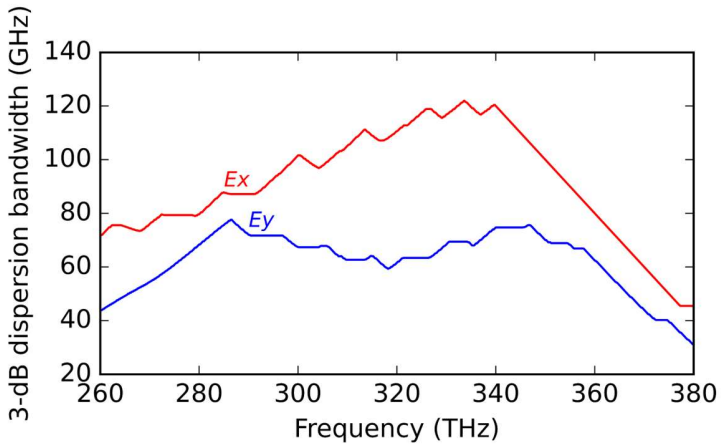

Figure 3.6: 3dB-dispersion bandwidth of the E_x (red) and E_y (blue) polarization of 1 cm long unclad waveguide.

The power transmittance of the Si wire waveguide was probed in the experiments designed according to the block diagram shown in Figure 3.7 (a). In practice, the E_x and E_y modes are excited by rotating the metallic hollow waveguides by 90°. For the measurement, a signal generator was used to deliver a millimeter-wave signal that was multiplied by 9 to deliver the THz signal. The THz waves were injected into the Si wire waveguide through a metallic hollow waveguide. During detection, a mixer was employed to down-convert the received signal, which was then processed and displayed on a spectrum analyzer. The measured (solid lines) and simulated (dotted lines) transmittances for both the E_x (red line) and E_y (blue line) modes were in good agreement as shown in Figure 3.7 (b). In the case of E_x, the average transmittance was approximately -0.1 dB, which is very close to the ideal value of 0 dB, across 260–380 GHz. This range of THz frequencies is particularly interesting because it might be the implementation target of future networks beyond 5G. For E_y mode, measured and simulated transmittances were in good agreement of approximately -0.1 dB at lower frequencies and increased to -0.3 dB at higher frequencies. The reflection (black lines) was less than -20 dB in both cases.

3.1.2 Communication experiment

The dual-polarization operation of the unclad waveguide was investigated through a THz-range communication experiment to demonstrate the increased data rates. For high-capacity communication, having broad transmission and dispersion bandwidths of waveguides is crucial. Dispersion bandwidth accounts for signal distortion owing to group delay dispersion. The 3 dB dispersion bandwidths of E_x and E_y are shown in Figure 3.8, wherein it is evident that the bandwidth of E_y is approximately 25 GHz at 320 GHz, whereas that of E_x is approximately 10 GHz, resulting in a bandwidth difference of approximately 15 GHz. Consequently, E_x excitation experiences less dispersion than E_y, which will result in better performance of E_x.

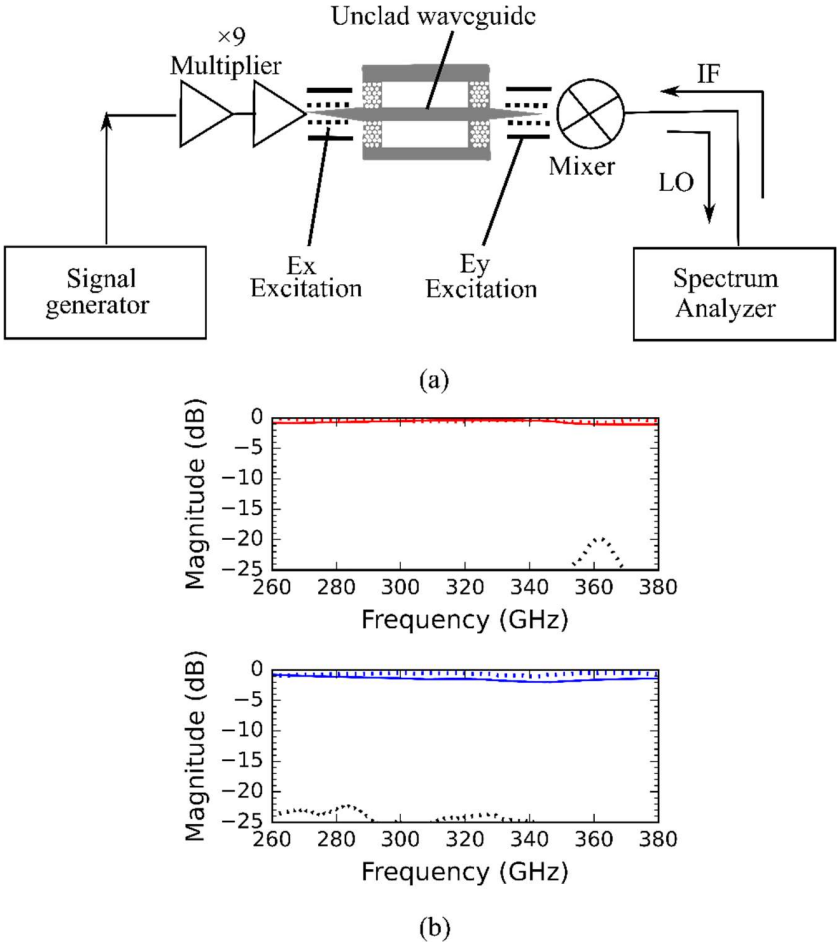

Figure 3.7: Transmittance measurements. (a) Block diagram of the experimental setup, (b) measured (solid line) and simulated (dotted line) transmittances of E_x (red) and E_y (blue). The reflection is indicated by the black lines.

We employed the experimental setup illustrated in Figure 3.5 (a); the images of the setup are shown in Figures 3.8 (b) and Figure 3.8 (c). On the transmitter side, an arbitrary wave generator (AWG) delivered a data signal that was used to modulate the optical signal from two laser sources using an OOK modulation scheme. The modulated signal was subsequently amplified by an erbium-doped fiber amplifier (EDFA) and down-converted by a uni-traveling-carrier photodiode (UTC-PD) to deliver a THz beating signal at 320 GHz. The resulting THz signal was then injected into the fiber through a hollow metallic waveguide. On the receiver side, an SBD receiver was employed to extract the transmitted data using envelope detection. A low-noise amplifier with a bandwidth of 18 GHz was employed to amplify the demodulated signal before it was reshaped using a limiting amplifier. The corresponding eye diagram and BER were assessed using a sampling oscilloscope and a BER tester (BERT), respectively. As shown in Figure 3.9, when the E*x* mode of the unclad waveguide was excited, maximum data rates of 24 Gbit/s ($<10^{-11}$) were achieved with a practical error-free implementation. In the case of E_y excitation, maximum data rates of 22 Gbit/s were achieved. The slight difference in the data rates achieved for the E_x and E_y polarizations could be ascribed to the additional 2 dB loss of the E_y polarization, as shown in Figure 3.7. The maximum data rate was limited, likely due to the bandwidth of the low-noise amplifier. These account for an aggregate data rate of 46 Gbit/s for dual polarization. The difference in the data rates achieved for the E_x and E_y polarizations can be ascribed to the higher dispersion associated with a lower 3 dB dispersion bandwidth for E_y as shown in Figure 3.7 in addition to increased insertion loss between the metallic hollow waveguide and unclad waveguide for E_y polarization.

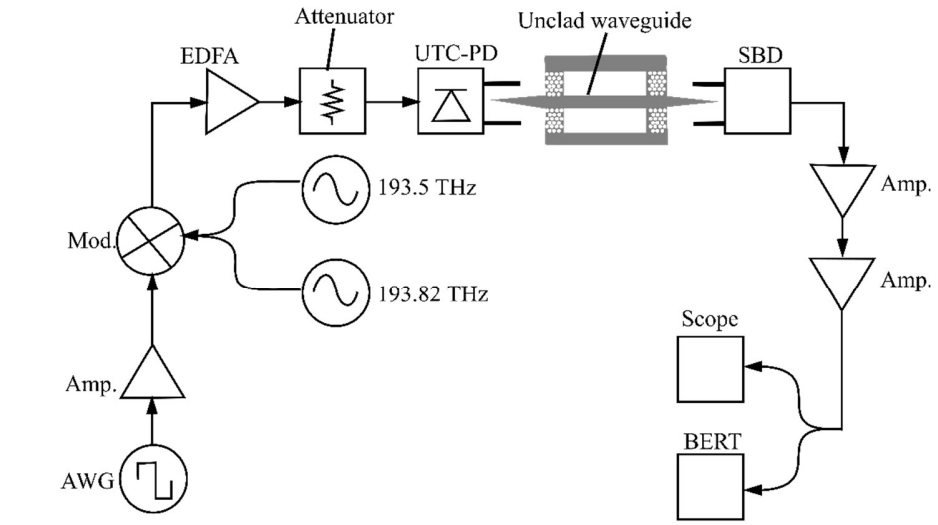

(a)

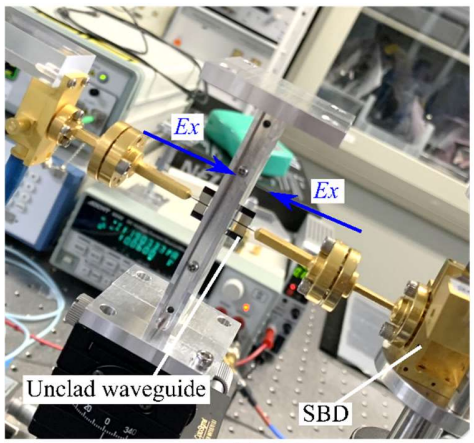

(b)

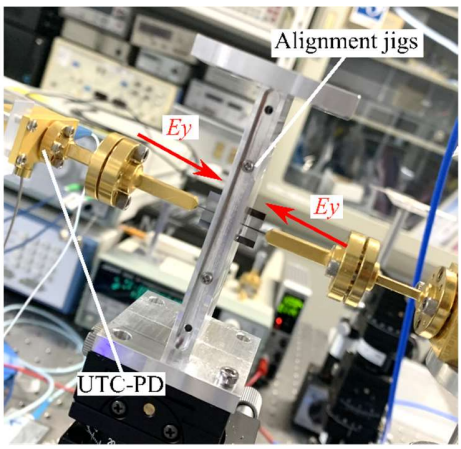

(c)

Figure 3.8: Experimental setup: (a) block diagram of the E_x-excitation setup, (b) image of the of E_x excitation setup, (c) image of the E_y excitation setup.

3.2 Polarization multiplexing over Si diplexer

Frequencies in the THz region have been the subject of high-speed wireless communication applications, to their intrinsic broad bandwidth. So far reported wireless communication links of 50 Gbit/s in the 300 GHz band have achieved real-time error-free communications, based on the OOK modulation scheme [107], [108]. Multiplexing can further expand the potential of THz range communications and enhance the throughput of the

communication links, by transmitting multiple individual carriers on a single shared transmission path. Most implemented multiplexing techniques including time division [109], [110], and code division [111]–[113], require multiplexers that combine both carrier signal divider and combiner functionalities. Implementing multiplexing techniques such as frequency-division-multiplexing (FDM) requires a set of functional components such as waveguides, microstrip lines, and coplanar waveguides that are unfortunately lossy to the skin effect [114]. Diplexers combine both waveguiding technologies and other functional components needed for the implementation of multiplexing.

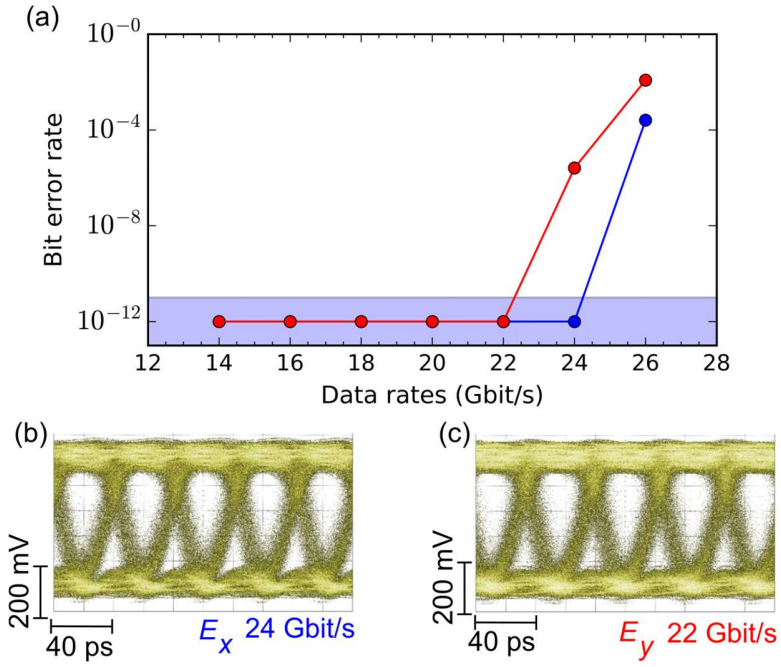

Figure 3.9: Communication experiment results: Recorded data rates versus BER for *Ex* (blue) and *Ey* (red) polarizations (a) and the corresponding eye diagrams for E_x (b) and E_y (c).

For the realization of an efficient broadband communication link based on multiplexing, diplexers with high isolation that suppresses crosstalk are required. But such diplexers are usually complicated to design. In addition, multiplexing techniques have been mostly restricted to frequency multiplexing, but not polarization multiplexing. This is because most metallic

components such as hollow metallic waveguides only support single-mode polarization. For all-dielectric components based on the PBG, only the E_x polarization, where the electric field is oriented parallel to the Si slab plane is supported. In the meantime, recently dual *Ex* and E_y dual polarizations have been reported in all-dielectric EM waveguides [105]. However, only the polarization purity was investigated through the cross-polarization analysis, and there were no reports on polarization Multiplexing. Mode-division multiplexing has been previously reported in optical fibers, but never in all-dielectric platforms. In this section, we leverage low-loss dielectric waveguides to realize a diplexer that can be employed for polarization multiplexing. Here, we demonstrate dual E_x and E_y polarizations across a THz range diplexer.

3.2.1 Diplexer: Design and operation principle

We designed an all-dielectric diplexer that is shown in Figure 3.10. The diplexer comprises two unclad waveguide bends implemented with a 45° circular bend of radius 2 mm. Each waveguide was optimized for operation in the WR-3.4 band (220 – 330 GHz). The waveguide core has a width of 315 μm and the EM section was implemented using an array of through-holes of diameter D = 117 μm, and a lattice constant a = 151 μm. The diplexer was fabricated in high-resistivity (> 10 kOhms.cm) intrinsic Si slab with a thickness of 200 μm. The Si slab is extended to implement frames for ease of handling during experiments, but also for the protection of the waveguide core. Two unclad waveguides are brought into proximity, separated by a gar s = 50μm across a coupling length of L = 1.7 mm. The values for s and L were chosen to realize an evanescent coupler, where modal field transfer is enabled from one waveguide to another through evanescent coupling. Previous reports of the evanescent coupler exploited the weak confinement of THz waves at lower THz frequencies, against the strong confinement of higher frequencies to implement FDM multiplexing [115]. That is, because of the weak confinement of THz waves at lower frequencies, a greater portion of the modal fields at those frequencies is evanescent. Consequently, it was possible to capture those fields by placing a second waveguide in the vicinity. This makes it possible for the diplexer to implement both splitting and combining of the THz waves based on the critical design parameters which are the gap s and the length L. Here we leverage evanescent coupling to implement polarization

selection and demonstrate the potential of the diplexer for the implementation of polarization multiplexing. Initial investigations are conducted at the 0.3 THz frequency band and could be extended to the 0.9 THz frequency band. The values of s and L were achieved through parametric study to enable E_y polarization to be coupled through evanescent coupling while filtering E_x polarization.

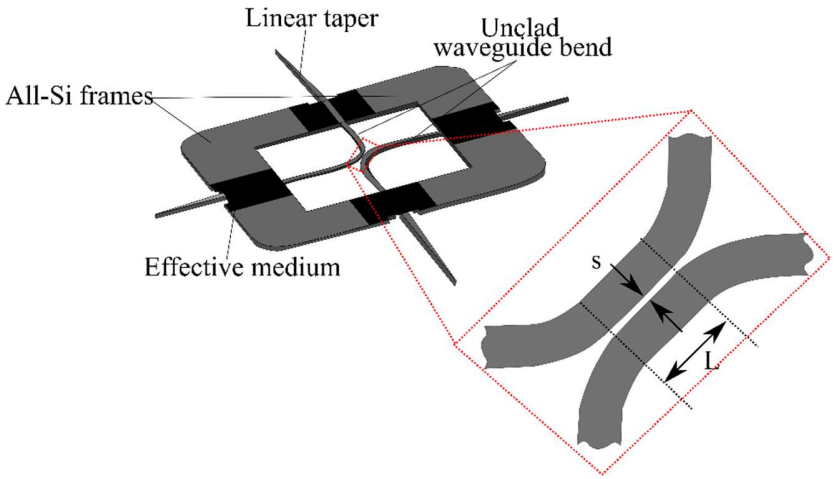

Figure 3.10: Design of the diplexer with the coupling section as inset.

3.2.2 Polarization multiplexing over diplexer

3.2.2.1 Concept of polarization multiplexing

THz hollow core fibers will enable the development of data centers, as they can serve as efficient short-range interconnects for chip-to-chip, board-to-board communications. To this end, hollow core fibers will also need to support multi-channel communications, in the fashion of classic transmission lines. One way to achieve that is to couple hollow core fiber with an all-dielectric unclad diplexer that supports dual E_x and E_y polarizations. The concept for such a multi-channel link based on THz hollow core fiber is illustrated in Figure 3.11. Hollow core fiber can serve as an interconnect between two unclad diplexers. The first diplexer is used as an input interface, where both E_x and E_y polarization can be excited. The Cross channel can be employed to transmit E_y polarization through evanescent coupling, and the Bar channel for the transmission of Ex polarization over an unclad waveguide bend. The two polarizations excite

the output of the first diplexer, which is inserted into the hollow core fiber. As we have demonstrated, hollow core fibers can support multiple modes depending on the diameter. A 1 mm-core fiber could support both E_x and E_y polarization. We can select the carrier frequency in 240 – 280 GHz, which is the window of opportunity we identified for high transmission of E_y polarization, as shown in Figure 3.15. Subsequently, the hollow core fiber routes both polarizations to the second diplexer, where polarization separation occurs.

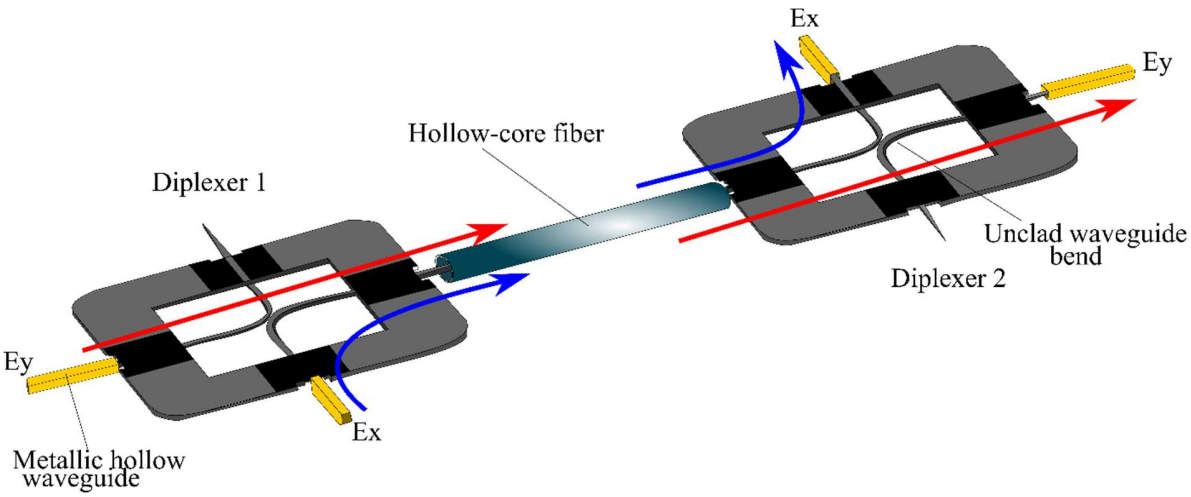

Figure 3.11: Concept of polarization with an unclad diplexer and hollow core fiber.

3.2.2.2 Theoretical analysis of simultaneous dual polarization over diplexer

We investigated the polarization differentiation properties of the diplexer by considering the two configurations presented in Figure 3.12 and figure 3.13. In the first configuration shown in Figure 3.9, port 1 excites E*x* polarization, while ports 2 and 3 are set to support E_x, and E_y polarizations respectively. This configuration renders an E_x-E_x Bar channel and an E_x-E_y Cross channel. This configuration was verified in experiments as shown in Figure 3.12 (b) using a multiplier-based THz source and calorimeter-style power meter. The power transmission for both Bar and Cross is presented in Figure 3.14 for theoretical results and experimental

measurements. It is evident that in the case of the Bar channel (blue), measured transmittance (solid line) is in good agreement with the simulation (dotted line), and close to the ideal value of 0 dB. Such performance of the unclad waveguide bend is expected, as these waveguides are an extremely low loss. For the Cross Channel (red), the measured power is ~ -20 dB in measurement (solid line), corresponding to the noise level of the power meter. In simulation, the measured power level was -120 dB (dotted line). These results confirm the operation principle of the diplexer, by allowing the coupling of E_x polarization in the Bar channel and the differentiation of E_y polarization in the Cross channel.

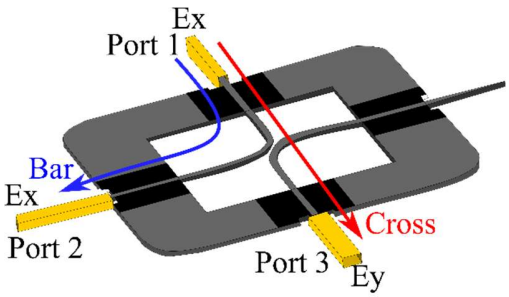

(a)

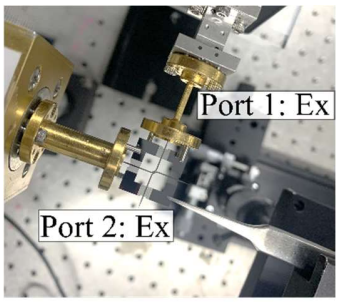

(b)

Figure 3.12: E_x excitation: (a) excitation principle; (b) photograph of the experimental setup.

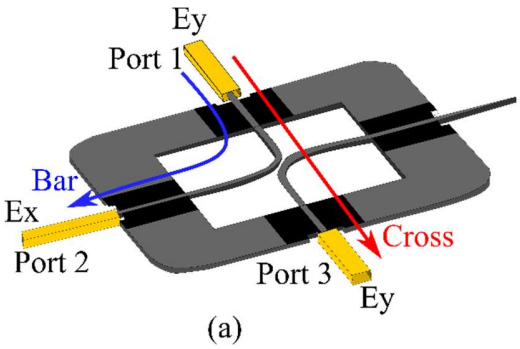

(a)

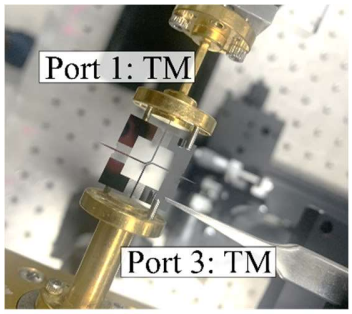

(b)

Figure 3.13: E_y excitation: (a) excitation principle; (b) photograph of the experimental setup.

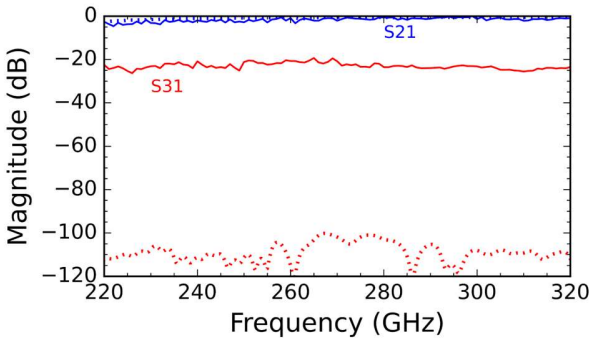

Figure 3.14: E_x excitation: Transmittance measurement. Blue denotes the Bar channel and red cross channel. Simulated results are shown in dotted lines.

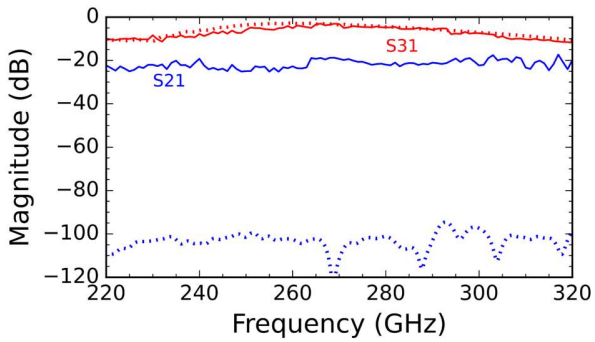

Figure 3.15: E_y excitation: Power probing. Blue denotes the Bar channel and red cross channel. Simulation results are shown in dotted lines.

For the second configuration as shown in Figure 3.13 (a), port 1 excites E*y* polarization, while ports 2 and 3 are set to support E_x, and E_y polarizations respectively. This configuration renders an E_y-E_x Bar channel, and an E_y-E_y Cross channel, and is verified in experiments using a similar process as for the first configuration, with a photograph of the setup shown in Figure 3.13 (b). The results are presented in Figure 3.15, and for the Bar channel, the measured transmittance is ~-20 dB, which corresponds to the noise level of the power meter. Whereas the measured and simulated isolation for the Cross channel is in good agreement, with a maximum transmittance of -3 dB at 260 GHz, with a 3-dB bandwidth of 40 GHz. These results confirm the evanescent coupling of E_y polarization in the Cross channel while filtering the E_x polarization. The cross channel also confirmed good polarization differentiation.

Considering two-channel simultaneous communications such as the configurations presented in Figure 3.12 and Figure 3.13, for applications such as polarization multiplexing, channel crosstalk should be avoided. This is because crosstalk between the channel can create interferences, that could negatively impact the quality of the channel. We investigate the crosstalk phenomenon in simulations considering the configurations shown in Figure 3.16 (a) and (b). The results are presented in Figure 3.17 (a) and (b). It can be noted that for the E_x polarization, there is little transmittance in the cross channel with the transmittance from Port 1 to Port 3 reducing from ~-5 dB at 220 GHz, to -25 dB at 380 GHz. This is indicative of low crosstalk and good polarization isolation. In contrast, there is good transmission between Port 1 and Port 2, with a loss of ~2dB at 220 GHz, and < 1 dB for frequencies > 260 GHz. The higher

loss at 220 GHz could be ascribed to the proximity to the cutoff frequency at the lower end of the frequency band. For the E_y polarization, the crosstalk is quite negligible in 230-270 GHz, where the Bar channel has a transmittance of ~ -10 dB. At 260 GHz, the transmittance is ~-35 dB, which indicated that this frequency could be an ideal carrier frequency for the transmission of E_y polarization over evanescent coupling. One concern would be the narrow bandwidth for the E_y polarization transmission, but considering a transmittance level of -10 dB, the bandwidth could be approximated to ~40 GHz, which is enough for a proof-of-concept demonstration.

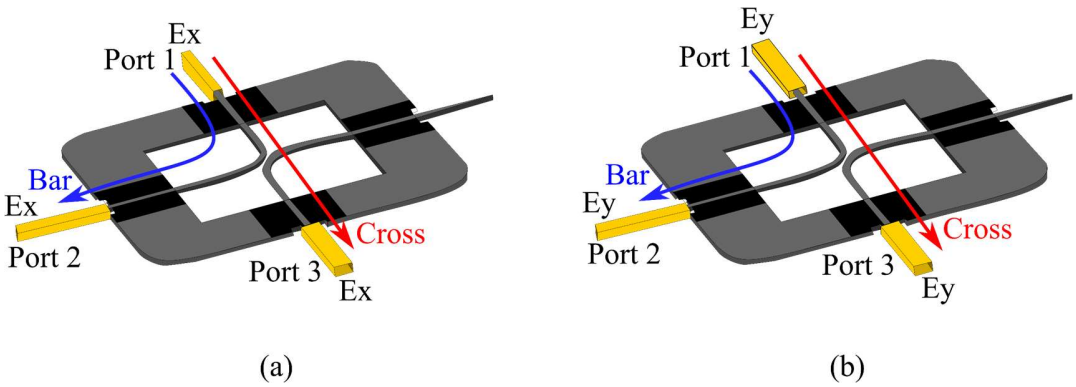

Figure 3.16: Configuration for the analysis of the crosstalk: (a) Crosstalk of E_x polarization; (b) Crosstalk of E_y polarization.

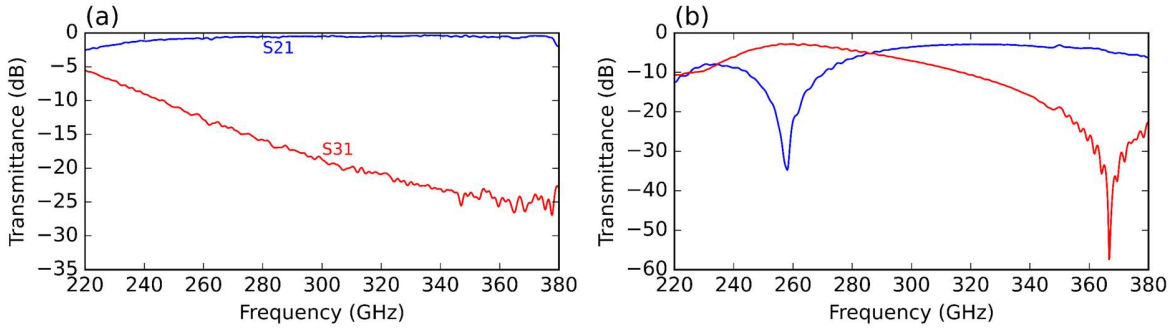

Figure 3.17: Transmittance for the crosstalk analysis of E_x and E_y polarizations: (a) results for the configuration shown in Figure 3.16 (a), and (b) results for the configuration shown in Figure 3.16 (b).

Chapter 4

Hollow core THz fiber link over silicon waveguide interface

Nascent data-intensive emerging technologies are mandating low-loss, short-range interconnects, whereas existing interconnects suffer from high losses and low aggregate data throughput owing to a lack of efficient interfaces. In this section, we investigate a novel THz fiber link that employs a silica glass fiber with a silver coating. We start by analyzing the fundamental properties of hollow core fibers, as well as all-dielectric interfaces that can be implemented with these fibers toward realizing heterogeneous integrated components.

4.1 Fundamentals of hollow core fibers

The development of emerging technologies such as the metaverse, and high computing data centers together with data-intensive systems has been enabled by the advancement of PICs [116]. PICs have allowed single-chip integrated functionalities to support intra-/inter-chip communications. However, current on-chip interconnects cannot meet the needs of the ever-growing computational, and aggregate data throughput, creating an interconnect gap that remains a major performance bottleneck [117]. THz range interconnects have the potential to bridge the interconnect gap, focusing on communication distances between 1 mm and 10 cm, which is the “last centimeter region” for on-chip communications [118]. Si dielectric THz interconnects have demonstrated applications towards 6G and beyond, with extremely low loss of < 0.1 dB/cm and increased bandwidth of ~350 GHz [100], [115]. However, because they are made of high-resistivity crystalline Si, they do not offer the flexibility that is required for chip-

to-chip and module-to-module interconnection. Hollow core fibers have gained a lot of attention as efficient and flexible interconnects. Hollow core fibers coupled with dielectric waveguides have reported a loss of 2 dB/m with a bandwidth of 50 GHz and 10 Gbit/s data rates over a 1-m ePTFE clad fiber [119]. But the coupling efficiency between the dielectric waveguide and the fiber was limited to 30%. More recent studies reported a PTFE core fiber link with 20 Gbit/s data rates under OOK modulation over 25 cm [120]. The loss of the fiber was 20 dB/m, and the fiber link employed a 3D-printed coupler, resulting in a coupling loss as high as 10 dB. In both reported studies, the fiber core with cladding was directly exposed to air, which resulted in poor robustness of the fibers.

4.1.1 Modal analysis and dispersion

The hollow core fiber is made of silica glass with a silver coating, as reported in reference [121]. The thickness of both silica glass and silver coatings is 100 nm. For the inner diameter of the fiber, we considered two cases with 0.7- and 1-mm core diameters. This is because the number of modes supported by a waveguide of this sort tends to be dependent on the waveguiding area size, i.e., the cross-section of the fiber. Modal analysis of the hollow core fiber can be performed by assuming a circular cross-sectional hollow waveguide. We investigated the dispersion bandwidth of the THz fiber. For high-capacity communication, it is important to have a broad dispersion bandwidth to avoid signal distortion due to group delay dispersion [122]. The dispersion bandwidth of the THz fiber defines the bandwidth of a dispersive medium in which the phase velocity of propagating waves is dependent on the wavelength. The dispersion curves for each type of fiber were calculated using COMSOL Multiphysics and are presented in Figure 4.1 (a) and Figure 4.1 (b) for the 1-mm core and 0.7-mm core fibers, respectively. Figure 4.1 (a) and Figure 4.1 (b) confirm the five modes supported by the 1-mm core fiber and two modes supported by the 0.7-mm core fiber. The corresponding mode profiles for the 1-mm core fibers of TE_{11}, TM_{01}, and TE_{21} are shown in Figure 4.2 (a), Figure 4.2 (b), and Figure 4.2 (c), respectively. For the 10-cm long fiber (blue), the dispersion bandwidth of the 1-mm core fiber (Figure 4.3 (a)) is 28 GHz at the center frequency of the WR-2.8 band (260–390 GHz), i.e., 330 GHz, and the dispersion bandwidth for 0.7-mm core

fiber (Figure 4.3 (b)) is ~ 13 GHz. Thus, the 1-mm core fiber can realize approximately twice the high-capacity communications rate compared to that of the 0.7-mm core fiber. Because the propagation constant β of a circular hollow waveguide is expressed by a hyperbolic function, as the frequency increases relative to the cutoff frequency the dispersion becomes linear which results in lower signal distortion owing to differences in group velocity. Consequently, a 1-mm diameter fiber with a lower cutoff frequency for the fundamental TE_{11} mode is less susceptible to the effects of group delay, and hence, a better candidate for high-capacity communication applications.

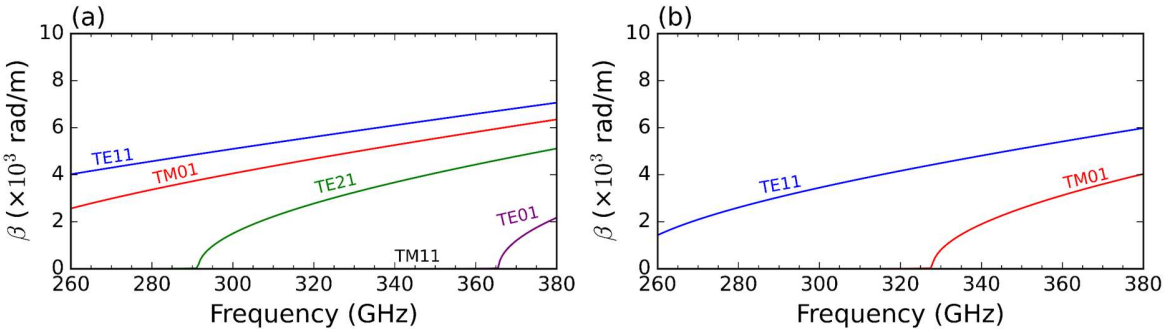

Figure 4.1: Dispersion curves of (a) 1-mm core, (b) 0.7-mm core fibers showing the propagation constant as a function of frequency.

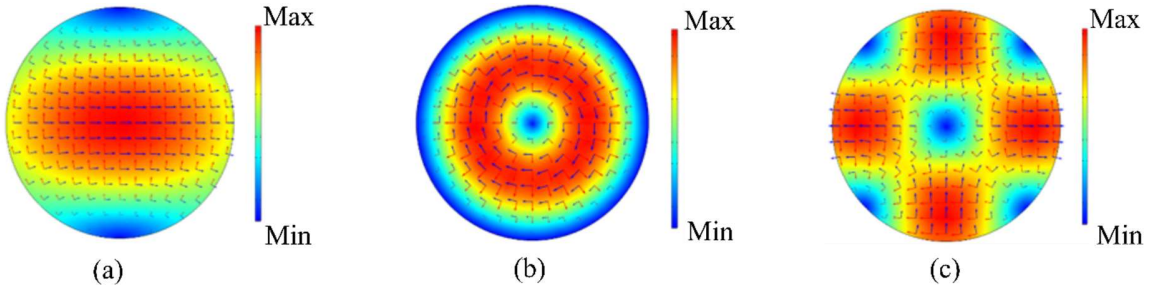

Figure 4.2: Mode profiles of 1mm-core fiber: (a) TE_{11}, (b) TM_{01}, and (c) TE_{21}. Color map shows the electric-field intensity of in-plane component.

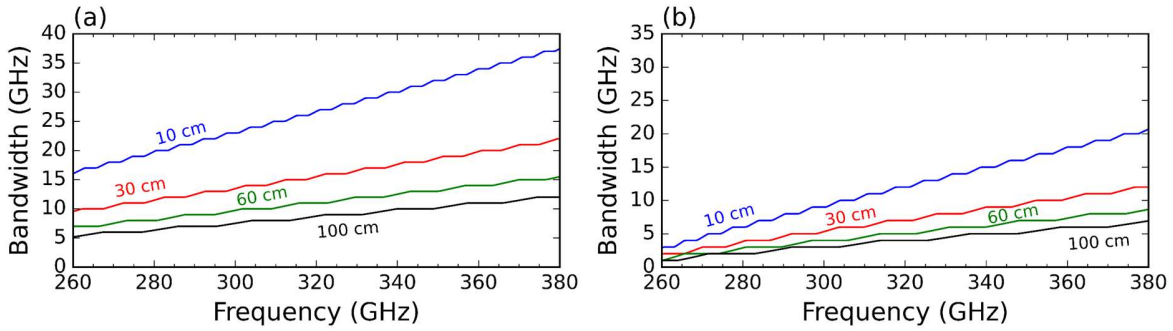

Figure 4.3: Dispersion bandwidth as a function of frequency: (a) and (b) for 1-mm, and 0.7-mm core, respectively.

The results of the modal analysis were confirmed by theoretical calculations of the cutoff frequency *fc* for each mode supported by the fibers using Equation (4-1) [123]:

$$f_c = \frac{P_{nm}{}' c}{2\pi r\sqrt{\mu\varepsilon}} \tag{4-1}$$

where P'_{nm} represents the zeros of Bessel functions of the first kind, c is the velocity of light in free space, r is the radius of the circular waveguide, ε is the permittivity constant, and μ is the permeability constant. Based on Equation (3), the cutoff frequency *fc* of each mode for the 0.7-mm and 1-mm core fibers is summarized in Table 4.1. The calculation of the cutoff frequencies for the circular waveguide is detailed in Appendix 2.

Table 4.1: Calculated cutoff frequency of first-order modes supported by each fiber

Mode	$2r$ = 1 mm	$2r$ = 0.7 mm
TE_{11}	176 GHz	251 GHz
TM_{01}	230 GHz	328 GHz
TE_{21}	292 GHz	417 GHz
TM_{11}	366 GHz	523 GHz
TE_{01}	366 GHz	523 GHz

As can be seen in Table 4.1, the number of guided modes in the fiber increases with diameter. That is, the fiber of 0.7-mm diameter supports fewer modes than the fiber of 1 mm diameter. For the fiber of 0.7-mm diameter, only the fundamental TE_{11} mode and the TM_{01} modes are supported for operation in the WR-2.8 band, which covers frequencies from 260 to 400 GHz. For the other modes, the cutoff frequency is beyond the frequency range of interest. For the 1-mm diameter fiber, five modes have fc within the frequency range of interest. These calculations confirm our initial modal analysis.

4.1.2 Loss estimation of hollow core fibers

To estimate fiber loss, we probed the power transmission in fibers of different lengths using the experimental setup shown in Figure 4.4 (a). Two sets of fibers with 1-mm and 0.7-mm core diameters were prepared, and four fibers with lengths of 10, 30, 60, and 100 cm were tested for each set. A signal generator was employed to generate a millimeter-wave signal that was inputted into a 9-times multiplier coupled to a WR-2.8 band hollow waveguide that delivers a THz range signal into the fiber through the unclad wire waveguide interface. A variable attenuator was attached to the hollow waveguide to maintain a constant safe power level in the mixer. The waveguide acted as a coupling interface. On the detection side, a THz range mixer was employed to perform frequency down-conversion, for producing microwave signals that were processed using a spectrum analyzer. Alignment jigs were employed to position the waveguides, for ensuring vertical alignment without tilts. This helps reduce imperfect alignment between the hollow metallic waveguides and the unclad waveguide as well as between the unclad waveguide and the fiber. A photograph of the experimental setup is shown in Figure 4.4 (b).

The measured transmittances of the 1-mm and 0.7-mm core fiber are presented in Figure 4.5 (a) and Figure 4.5 (b), respectively. The 1-mm core fiber achieved better transmittance than the 0.7-mm one. The difference in performance increased as the fiber length increased. An average transmittance of approximately -5 dB for the 10-cm fiber was achieved by both the 1-mm and 0.7-mm core fibers. Similar performances for the 1-mm and 0.7-mm cores were achieved for the 30-cm and 60-cm fibers, with average transmittances of approximately - 9 dB and -11 dB, respectively. However, for the 1 m long fiber, the difference in performance is

significant with a transmittance of -15 dB for the 1 mm core fiber and -20 dB for the 0.7 mm core fiber. The lower transmittance of the 0.7 mm core fiber can be ascribed to the dispersion phenomenon of this fiber, as discussed in 4.1.1.

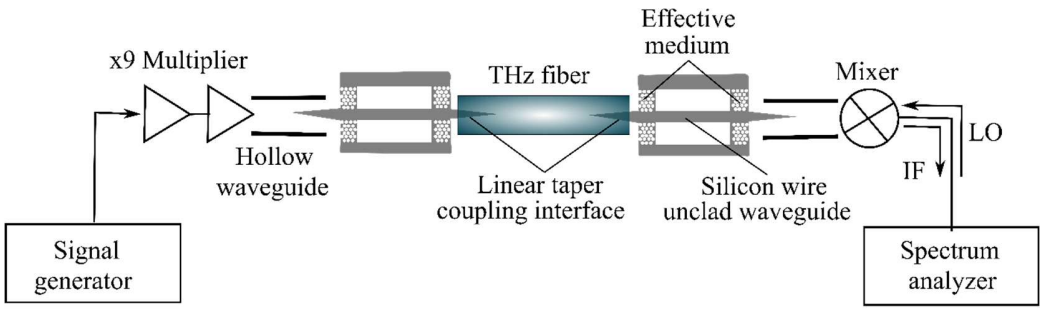

(a)

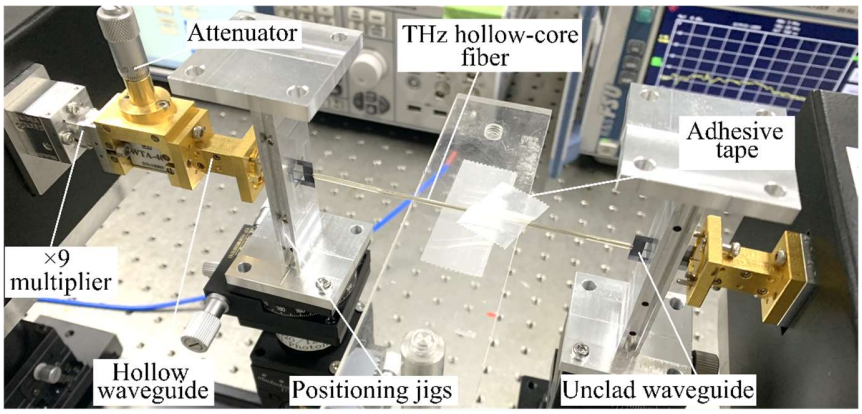

(b)

Figure 4.4: Experimental setup for the measurement of the transmittance of fibers: (a) block diagram, (b) photograph of the setup.

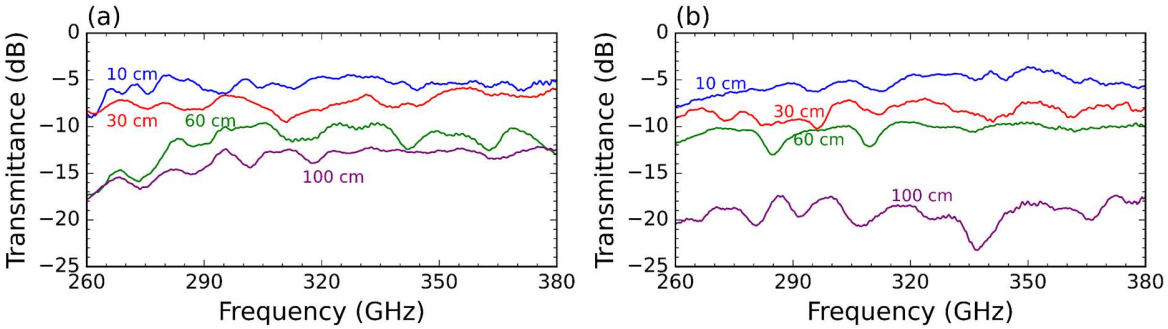

Figure 4.5: (a) Measured transmittance of 1 mm core fiber, (b) measured transmittance of 0.7 mm core fiber. The lower transmittance of -20 dB for the 0.7 mm core fiber could be ascribed to the higher dispersion of the fiber.

Probing the transmission power of the four fibers with different lengths allows the estimation of propagation and coupling losses. The four measurements for 10, 30, 60, and 100 cm correspond to four data points that were fitted to a curve using the least squares method. Subsequently, the propagation and coupling losses can be deduced using the slope and intercept of the curve. In other words, the slope corresponds to the propagation loss and the intercept corresponds to the coupling loss. An illustration of this procedure for a 1-mm core fiber at 320 GHz is shown in Figure 4.6 (a). The results for a 10 cm-long fiber in the entire WR-2.8 band are presented in Figure 4.6 (b) for the 1-mm core fiber, and Figure 4.6 (c) for the 0.7-mm core fiber. It can be seen in Figure 4.6 (b) and Figure 4.6 (c) that the measured propagation losses (red) are ~1 dB and 1.5 dB for the 1-mm and 0.7-mm core fiber, respectively. The simulated propagation loss is in good agreement with the measured propagation loss for both fibers with averages of ~1 dB and ~1.5 dB for the 1-mm and 0.7-mm core fibers, respectively. The measured coupling loss (blue) is ~2 dB and ~2.5 dB on average for the 1-mm and 0.7-mm core fiber, respectively. Although the average value of the simulated coupling loss is comparable in the case of the 1-mm fiber, it shows less variation. This could be ascribed to the difficulty in accurately inserting the Si linear taper inside the fiber in the experiments. This difficulty is reflected in the increased coupling loss of the 0.7-mm core fiber in comparison to the 1-mm core fiber, owing to the much smaller diameter of the 0.7-mm core fiber. These results show that the 1-mm core fiber has reduced losses and is more suitable for applications in THz-range communications.

For the estimation of the loss of hollow core THz fibers, it is not only important to evaluate the loss with straight fibers, but also the bending loss of the fiber. Because these fibers are made of glass silica, their robustness is suspected to be higher than that of fibers made of porous ePTFE. We investigated the bending loss of the fibers as illustrated in Figure 4.7. Figure 4.8 shows a photograph of the experimental setup. For the measurements, we employed a 1m long fiber, and the fiber was bent 30º, 60 º, and 90 º around its central axis. The power transmission was probed, and the results are presented in Figure 4.9 (a). The bending loss associated with the three rotation angles is quite similar with very few variations. In general, the loss is between 0 and 3 dB. The loss is less than 0 dB around 310 GHz, which could be ascribed to calibration errors with the reference measurement. The reference measurement is

done considering a 1m straight fiber. A maximum bending loss < 0.06 dB can be derived from the power transmission measurement. This could be ascribed to the robustness of the fiber, which is immune to bending. The small variations in the power transmission loss across the three rotation angles is a testimony to the fiber robustness.

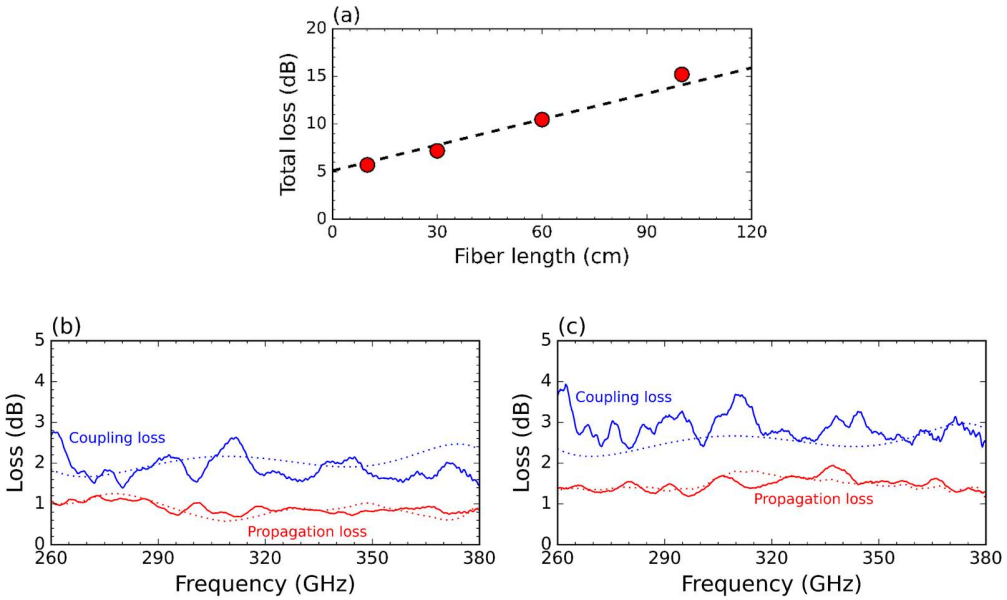

Figure 4.6: Estimated propagation loss (red) and coupling loss (blue) of fiber: (a) curve-fitting and estimation for 1 mm core diameter fiber at 320 GHz, (b) 1 mm core diameter fiber, (c) 0.7 mm core diameter fiber. Measured values are presented in solid lines and simulated values are in dashed lines. For the coupling loss, measured values are higher than simulated results, owing to an increased difficulty for the insertion of the linear tapers in the THz fiber during experiments. In simulations, the ideal case, with perfect insertion was considered.

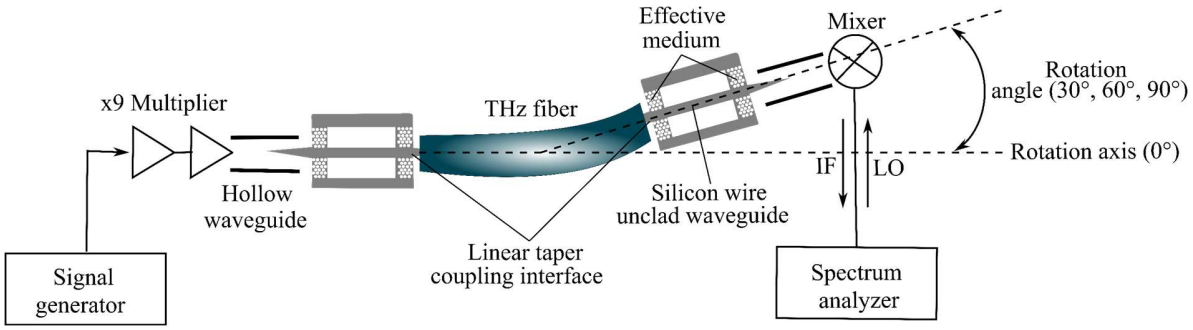

Figure 4.7: Configuration for the experimental verification of the fiber bending loss. The diagram shows the system for the power transmittance measurement.

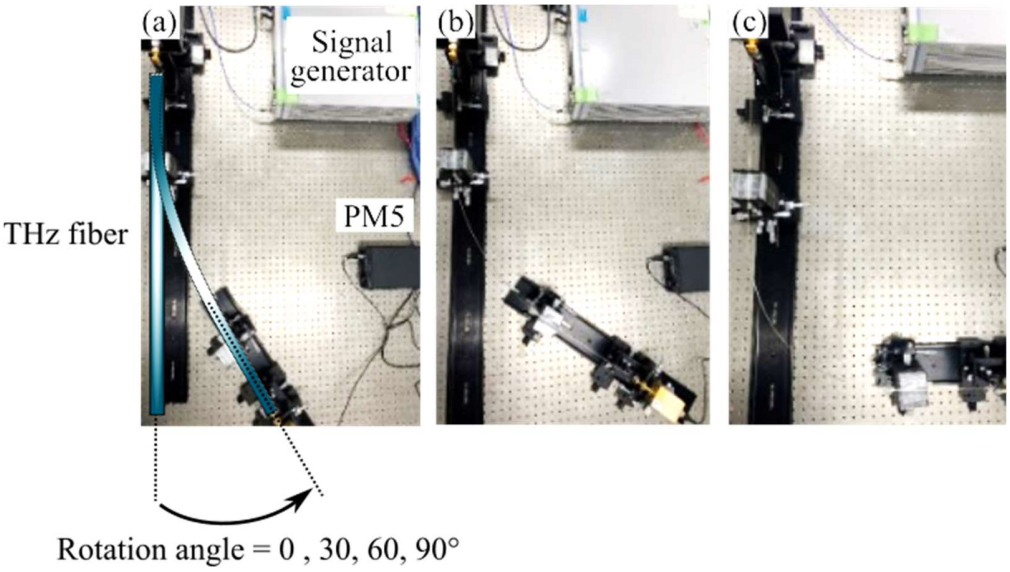

Figure 4.8: Photographs of the bending loss measurement setup: (a) 30º bend, (b) 60 º bend, and 90 º bend.

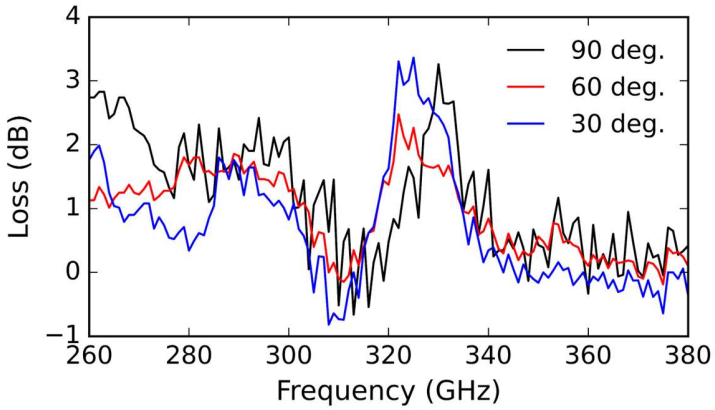

Figure 4.9: Bending loss of hollow core THz fiber. (a) total loss of 30º bend, 60º bend, 90º bend. Blue, red, and black denote 30º, 60º, and 90º, respectively.

4.2 Efficient dielectric interfaces based on Si waveguide for hollow-core fibers

Hollow core fibers are gaining momentum for various applications in the THz region. However, there are still a few roadblocks to overcome to make the most of the flexibility, and multi-modal properties of the hollow-core fiber. More specifically, adequate interfaces need to be engineered and devised to allow for ubiquitous and smooth integration with devices and

components ranging from RF to optical wavelengths. Usually, direct connection with the test and measurement equipment is not possible and results in increased losses. We investigated the direct coupling between hollow-core fiber and rectangular waveguide to confirm low power transmittance between the THz fiber and the metallic rectangular waveguide. This preliminary investigation is presented in detail in Appendix 3. In this section, we explore the possible interfaces that can support hybrid co-integrated heterogeneous components based on hollow-core fibers.

4.2.1 Hollow core fibers are attractive interconnects

The networks of the future will not only need broader bandwidth operation but also low latency to keep efficiency up to the standards of an all-connected world. This will require efficient interconnects for rack-to-rack communication between data centers that are physically in different locations ranging from 0.5 – 2 km [124]. For a long time, glass fibers were the interconnect of choice for such applications but reported latency of ~10 μs [125]. This is because, in hollow-core fibers, light propagates in a vacuum, at a speed close to 3×10^8 m/s. Hollow core fibers rose as alternative low-latency interconnects with a predicted 30% reduction of the latency. In the meantime, chips, boards, and data center configurations have changed a lot in the past few decades, incorporating more optical components. This change came with a few challenges as to the size mismatch between capillary-type fibers, and the optical components, which have dimensions in wavelength order. In this section, we investigate possible transition interfaces of high efficiency for dielectric waveguide components.

4.2.2 Investigation of Si waveguides interfaces

4.2.2.1 Single Rod interface

The tapered rod interface is the simplest interface to serve as a transition interface between the hollow core fiber and the metallic hollow waveguide attached to the measurement equipment. A performance index in designing transition interfaces is coupling efficiency. The coupling efficiency measures how effectively the interface routes most of the THz waves from and to the hollow core fiber. To investigate that in simulation, we considered models of the

fundamental components needed including the hollow waveguide, the linear taper, and the hollow core fiber as shown in Figure 4.10. The hollow waveguides are modeled after standard WR3.4 hollow waveguides (432 μm × 864 μm) by Virginia Diodes (4.10 (a)). The tapered structure follows a linear tapering (4.10 (b)), from a base width of 365 μm, which corresponds to the width of the Si wire that is employed as a waveguiding structure between the two tapers. For the hollow core fibers (4.10 (c)), we considered quite a large core fiber, which based on the modal analysis discussed in 3.2, should exhibit multi-mode operation, but because this analysis of the coupling efficiency is done with different interfaces, the relative performance should be the same, and the comparison of the interfaces remains fair.

For both the metallic hollow waveguide and the hollow core fiber, the material is a perfect electric conductor (PEC). For the linear taper, we considered high-resistivity Si of the refractive index of 3.4. For the investigations on the coupling efficiency, the first step is to assess the fundamental properties of the linear taper structure. Therefore, the transmittance and the reflection of the single rod linear taper were analyzed using the simplified model shown in Figure 4.11 (a). And thereafter, the efficiency of a straight Si wire terminated on either end with identical tapered structures was assessed as shown in Figure 4.11 (b). Figure 4.12 shows the simulated transmittance and reflection of the simplified model presented in Figure 4.11. (b). We confirmed good transmittance of ~0 dB across 220-330 GHz and reflection < -20 dB. Such low-loss performance is expected of dielectric waveguides of this sort. Subsequently, we investigated the transmittance with a 1-mm core fiber as shown in Figure 4.13. Here, we considered the taper length, the impedance matching between the linear taper and the THz fiber, but also the impact of the gap between the linear taper and the hollow core fiber. For the impedance, good impedance matching between the silicon taper and the fiber is crucial for better coupling performance. The simulated wave impedance of the Si effective-medium-clad waveguide and the fiber are shown in Figure 4.14, where the impedance of the THz fiber is close to that of free space and has a relatively large difference from that of the Si waveguide. To this end, a Si tapered structure is introduced to allow the propagation mode of the waveguide to be gradually coupled into the THz fiber with enhanced impedance matching. Consequently, as illustrated in Fig., the simulated reflection coefficient at the waveguide-fiber interface is well below -20 dB. Such a low level of reflected THz energy is not expected to impact the link

efficiency. For the length of the taper, the impact of the taper length on the coupling was analyzed as shown in Figure 4.15. The results show that the coupling increases as the length of the taper increases. This is because longer tapers allow for a more gradual transition of THz waves into the hollow core fiber. As shown in Figure 4.15, a 4-mm taper can achieve a coupling efficiency as high as ~90%. However, as the length increases, the taper is more susceptible to breakage. The length of the taper should be chosen to allow length-robustness balance.

The degree of insertion of the linear taper into the hollow core fiber is a critical parameter for achieving high coupling efficiency. Figure 4.16 shows the results of the coupling with hollow core fiber as a function of the gap. It can be observed that a maximum coupling if achieved is at ~220 GHz, with a gap of 1.4 mm. However, the performance is not uniform across the entire band, as the gap of 1.4 mm shows a lot of variations. A 2.5 mm gap exhibits much linear variation of the coupling across 220 – 330 GHz, with a maximum coupling efficiency of 45% at 230 GHz, and a minimum coupling of 15% at 330 GHz. Although a coupling efficiency of 50% is an improvement compared to previous studies that reported 30% coupling efficiency [126], there was still room for improvement, toward a more uniform coupling efficiency across the entire band of interest, as it will allow for more broadband applications. Therefore, we considered additional interfaces of rod array antennas and 2D lens elements.

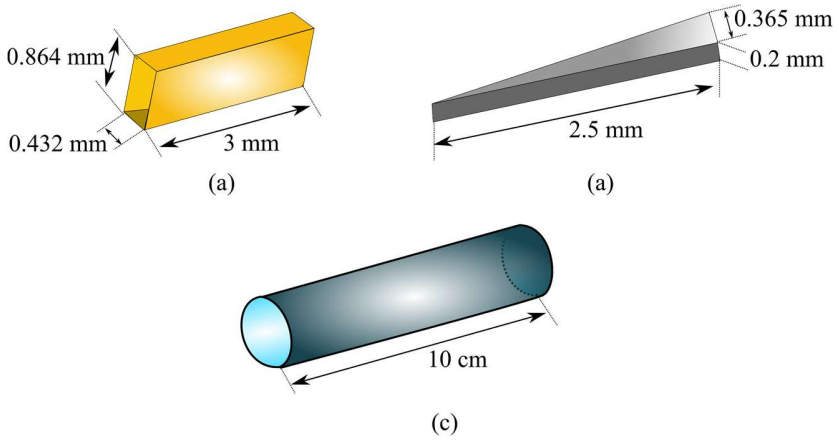

Figure 4.10: Fundamental components for the investigations of the dielectric rod interface: (a) metallic hollow waveguide; (b) All-dielectric linear taper interface; (c) THz hollow core fiber.

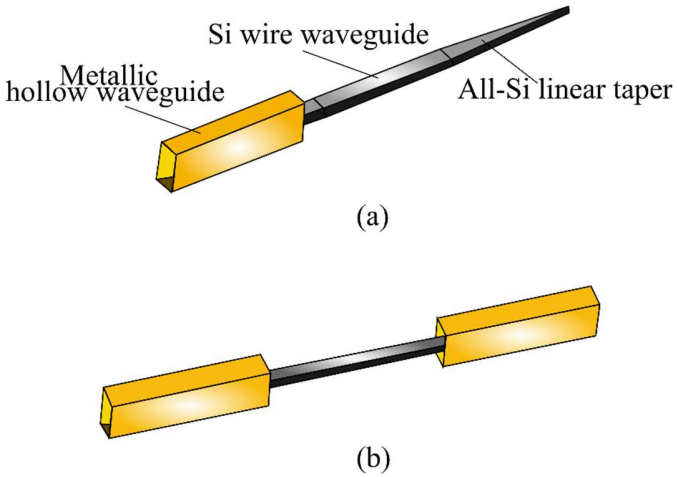

Figure 4.11: Simplified simulation model of the single rod antenna interface: (a) Model for the assessment of transmittance and reflection; (b) Model for the simulation of the transmittance and reflection of the Si wire waveguide

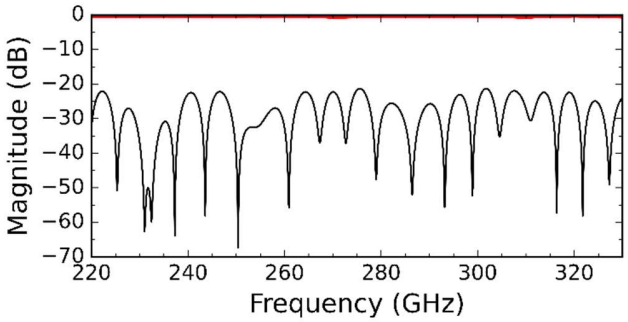

Figure 4.12: Simulated transmittance (red) and reflection (black) of the simplified single-rod linear taper.

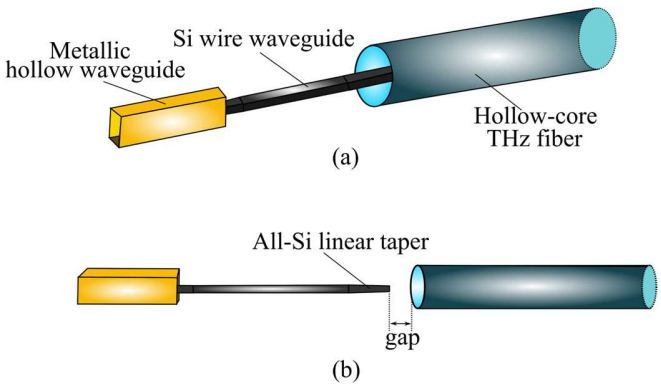

Figure 4.13: Simulated transmittance (red) and reflection (black) of the simplified single-rod linear taper.

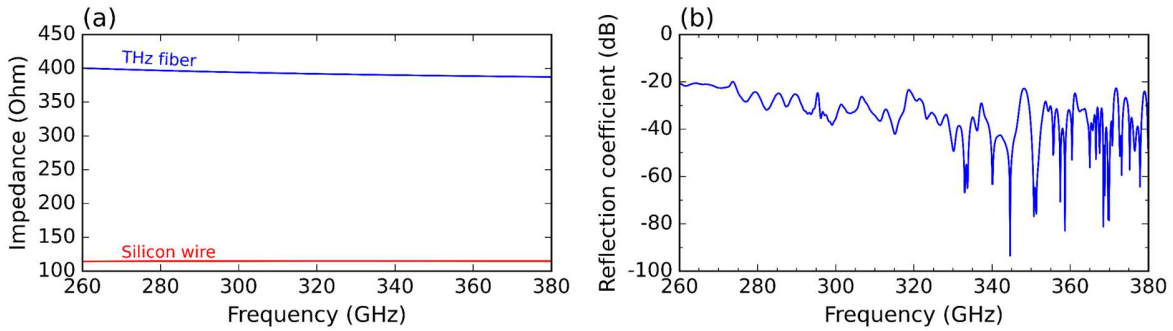

Figure 4.14: Simulated wave impedance and reflection coefficient. (a) Simulated wave impedance of the EM clad waveguide (red) and hollow core fiber (blue). (b) Simulated reflection coefficient at the waveguide-fiber interface.

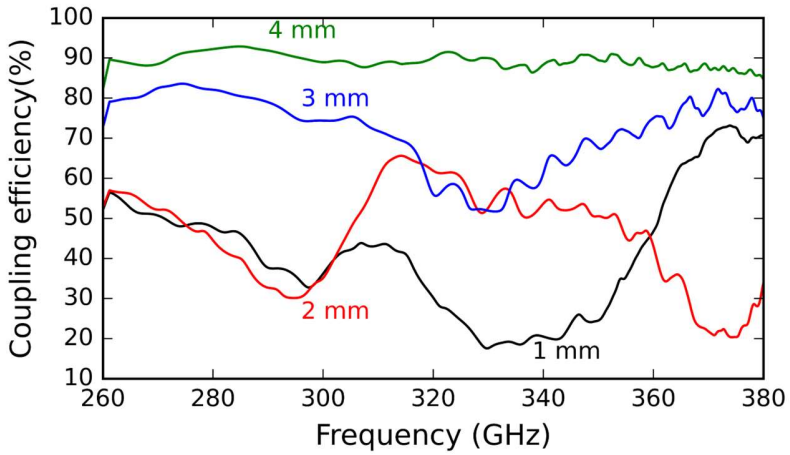

Figure 4.15: Coupling efficiency of various taper lengths.

4.2.2.2 Rod array interface

The single rod interface achieved a gain of ~9.5 dBi and maximum coupling efficiency of ~50%. We considered the gain might be a limiting factor in achieving higher efficiency and uniform coupling efficiency in 220 – 330 GHz. Array elements are commonly employed to improve the yield/performance of devices and components. This is the case for antenna elements as well. All-dielectric rod array antennas have been widely investigated for operation in the THz range. Previously reported dielectric antennas implemented a flaring section together with an

EM for impedance and/or modal matching [74], [82]. In [82], Withayachumnankul *et al.* reported an all-dielectric rod array antenna that comprises a photonic crystal waveguide, with a flaring section that acts as a planar horn antenna, an EM, and an array of rods. The flaring section is employed to feed the array of rods through an EM section that acts as a lens body to equalize the phase delay for the different rods. The reported rod array antenna achieved a 20 dBi gain across 315 – 390 GHz. Subsequently, a rod array antenna with a lens body was introduced in [74] and achieved a gain of 20 dBi across a much broader bandwidth in 260-380 GHz. Both antennas reported a gain of 20 dBi, twice the gain of a single rod antenna. We implemented a simpler rod array antenna to serve as an interface with the hollow core fiber as shown in Figure 4.17. Figure 4.17 (a) shows the antenna design, without any EM section. This is to reduce the complexity of the design, as EM structures tend to be difficult to manufacture because of the relatively small hole dimensions.

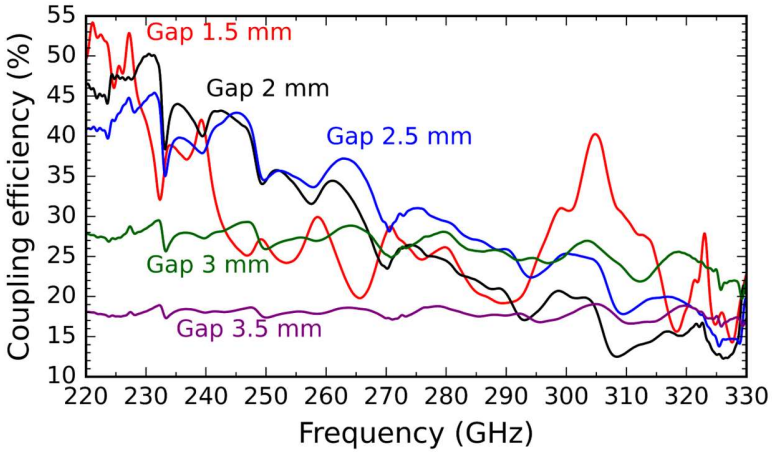

Figure 4.16: Simulated coupling efficiency between all-Si linear taper interface and hollow core fiber.

For array antennas, the gain depends on the number of rods of the antenna. Increasing the number of rods together with the aperture should increase the gain of the antenna. We studied the impact of the number of rods on the antenna gain, and a maximum gain of 14.5 dBi is achieved for 10 rods, and a minimum gain of 11 dBi for 30 rods. We notice that the gain is reduced as the number of rods increases, which is counter-intuitive but can be justified by the

constant aperture size of the flaring section. That is, even if the number of rods is increased, as the aperture remains the same, only the size of the single rods is reduced. Consequently, the increase in the number of rods leads to thinner rods and the array structure evolves into a uniform slab.

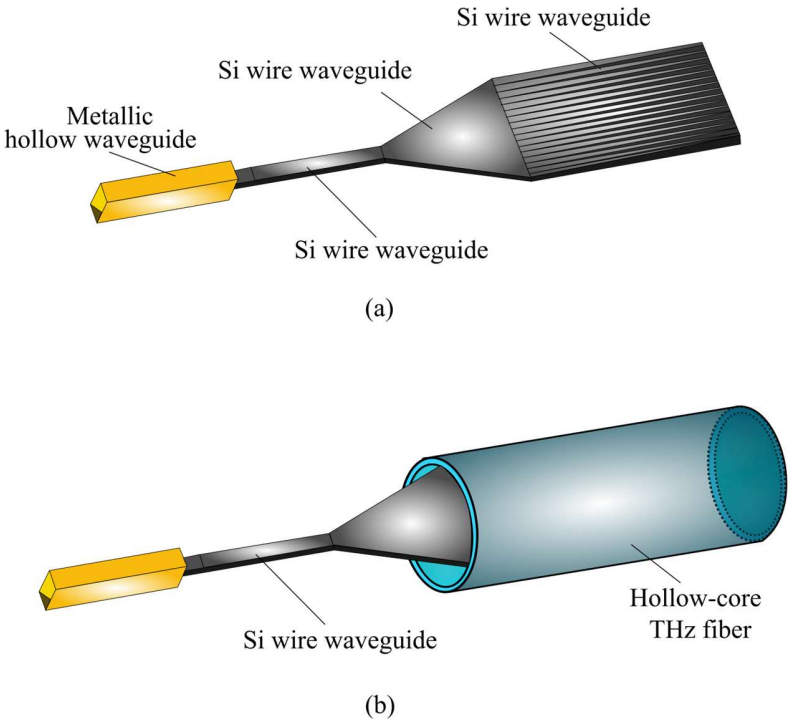

Figure 4.17: Simulation model of the rod array antenna with hollow core fiber: (a) Rod array antenna; (b) Rod array antenna coupled with 1 mm core diameter THz hollow core fiber. Each rod has a width of 0.25 mm at the base and is linearly tapered over a length of 5mm.

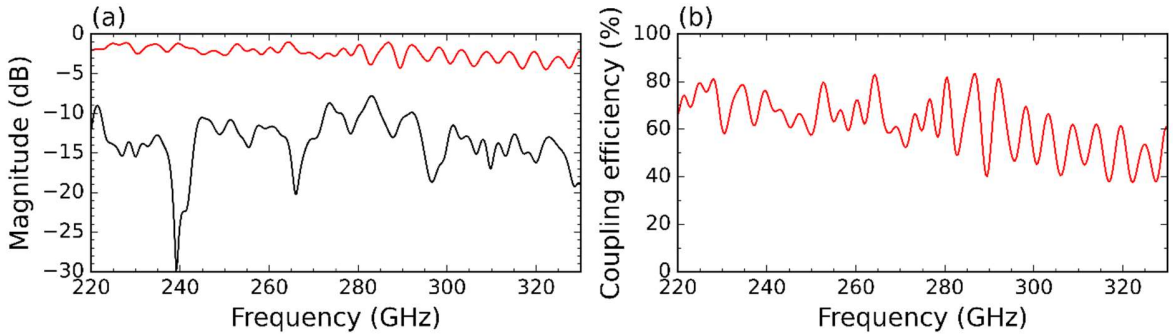

Figure 4.18: Simulated performance of the rod array antenna and hollow core fiber: (a) simulated transmittance (red) and reflection (black); (b) Simulated coupling efficiency.

After confirming the gain of the rod array antenna, we investigated the coupling between the rod array and the hollow core fiber as shown in Figure 4.17. The results of the coupling are shown in Figure 4.18. The transmittance is quite comparable to the single rod interface, but with a higher reflection of ~ -10 dB. This is expected as discussed before, owing to the reflection at the metallic walls of the fiber. The coupling efficiency of this structure is shown in Figure 4.17 (b) and the coupling is improved, with the coupling efficiency in the range of 40% - 80% across 220 – 330 GHz.

4.2.2.3 Lens interface

Dielectric lenses have been widely employed in the microwave region, to solve the high power loss of integrated antennas [127]–[129]. Integrated antennas on thick dielectric substrates suffer from power loss in the substrate [130]. The thinner the substrate, the less loss occurs. However, thin substrates tend to get even thinner in the order of 1-3 μm in the mmW and submillimeter wavelengths, rendering the designs non-manufacturable. Dielectric lenses have been employed to eliminate the substrate modes. Because dielectric lenses do not support surface waves, antennas placed on dielectric lenses exhibit a unidirectional radiation pattern, resulting in less power loss. Dielectric lenses of different sorts have previously been investigated including hemispherical, hyper hemispherical, or ellipsoidal. To serve as an efficient coupling interface, we investigated a two-dimensional (2D) hyper hemispherical lens, to allow for the integration with a planar all-Si waveguide platform, but also fabrication in a single etch process. The hyper hemispherical lens is a variation of the hemispherical lens with an extension length, i.e. the distance between the tip of the fundamental ellipse to its more distant focus, of R/n, where n is the index of refraction of the lens, and R is the radius of the lens. Hyper hemispherical lenses have been widely investigated and used in the mmW field, as they have reported very few spherical aberrations, which increases their efficiency in focusing all the rays of the optical system they are integrated with to a single point. Further, by improving ray focus, hyper hemispherical lenses yield shaper radiation patterns with an increase in gain of n^2 when integrated with the antenna.

The design of the lens starts with the definition of an ellipse:

$$\left(\frac{x}{a}\right)^2 + \left(\frac{y}{b}\right)^2 = 1 \tag{4-2}$$

Where a and b represent the major and the minor axes, respectively, and are defined as $c = \sqrt{b^2 - a^2}$; where ±c are the foci of the ellipse. From the ellipse, a hemisphere is derived as:

$$x^2 + y^2 = 1 \tag{4-3}$$

Choosing only positive *y* values. With the above considerations, we designed the 2D semi hyper hemispherical lens as shown in Figure 4.18 (a). The values of a = 2 mm, and b = 1.4 mm were achieved in a combination of the analytical expression and parametric studies. The coupling with THz hollow core fiber is shown in Figure 4.18 (b). The simulated coupling efficiency is shown in Figure 4.19. and a maximum efficiency of 40 % was achieved.

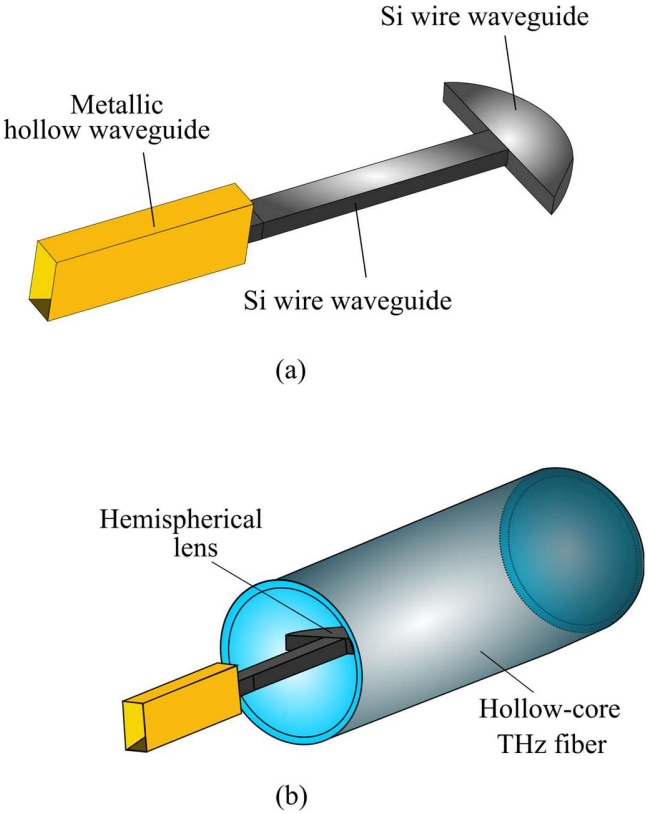

Figure 4.18: Simplified simulation model with semi-hemispherical lens: (a) lens structure and coupling to the hollow metallic waveguide; (b) coupling of the lens with THz hollow core fiber.

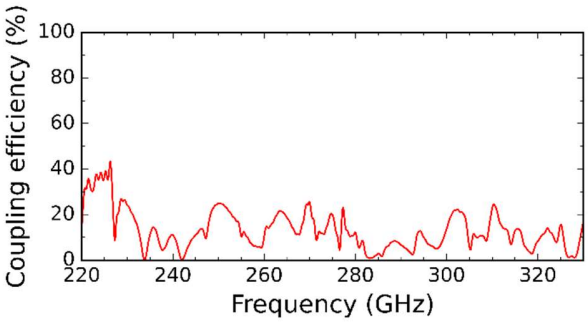

Figure 4.19: Simulated coupling efficiency between the 2D semi-hemispherical lens and THz hollow core fiber.

4.2.2.4 Conclusion

We analyzed different interfaces for coupling with THz fiber inclusion singe rod coupler, rod array coupler, and 2D planar lens coupler. The single rod reported a maximum coupling efficiency of up to 90% depending on the length of the taper. The rod array coupler and the lens coupler reported 80% and 40% maximum coupling efficiencies, respectively. These values for the coupling efficiency are constant across the frequency range of interest in 220 – 330 GHz, with little variations for the single rod and the rod array couplers. The variations are more significant for the lens coupler of ~30% difference between the coupling efficiency at 220 GHz, and that at 260 GHz. This could be ascribed to the non-uniform wave profile because of the small size of the lens. Indeed, the lens helps planarize incoming THz waves from the waveguides. The incoming aperture size of the lens should greatly impact the efficiency of the lens to planarize the THz waves. The performance of the lens coupler could further be improved by increasing its aperture. The couplers proposed here could compete with industry standards of coupling interfaces for fibers including sub-miniature type A (SMA) and ferrule core (FC) adapters. The typical insertion loss of SMA connectors is reported to be over 1 dB [131]. The value will greatly depend on the assembly process. In the case of an FC connector, the typical insertion loss is dependent on the material of the connector. For ceramic FC connectors, the insertion loss is ~0.3 dB [131]. For metallic FC connectors, the insertion loss is > 1dB, also depending on assembly precision [131]. Besides SMA and FC connectors, grating couplers are widely used for coupling to optical fibers. The design and the platform widely differ. A CMOS-compatible grating coupler with coupling loss between -1.34 dB and -0.79 dB was realized in SiGe platforms [132]. Other work reported lithium niobate (LiNbO3) with a coupling loss of -

0.89 dB and Si nitride (Si_2N_4) platform with a coupling loss of 5 dB. Printed 3D couplers have also gained in popularity and reported coupling loss of ~10 dB. Other work based on 3D couplers reported a lower loss of ~-8 dB. We summarize these performances for various couplers in Table 4.2. The single rod taper coupler is chosen for subsequent investigations on THz fiber owing to its high coupling efficiency with a very simplified design. We further investigate the impact of the single rod coupler depending on the positioning within the THz fiber, and also the tilt to confirm the minimum impact on the coupling efficiency. These results are presented in Appendix 4-5.

Table 4.2: Survey of fiber couplers

Coupler	**Platform/material**	**Design & fabrication complexity**	**Coupling efficiency (%)**	**Reference**
Grating coupler	SiGe	Complex requires a metal bottom layer for improved performance	~73– 83%	[132]
	LiNbO3	Complex requires cavity grating and top metal mirror for improved performance	~81%	[133]
	Si_2N_4	Complex requires an amorphous Si top layer for improved performance	31%	[133]
SMA	Metallic	Medium complexity can be fabricated in a large number	>80%	[131]
FC	Ceramic		~93%	
	Metallic		> 80%	
3D printed coupler	High-resistivity silicon	Complex requires laser writing equipment	10%	[120]
			15%	[134]
Linear taper		Simple, monolithic, favorable to hybrid integration	25%	[119]
			>60%	This dissertation
Rod array			90%	
Semi hyper hemispherical lens			40%	

4.3 Application I: high-data rates THz fiber link

4.3.1 Modal analysis of Si wire for hollow core fiber

Figure 4.20 details the realization of the fiber link based on a Si wire waveguide interface. An unclad Si waveguide is chosen as an interface for the fiber link because these waveguides are low-loss and broadband in comparison to photonic crystal waveguides. Unclad waveguides reported bandwidth of ~120 GHz and up to 350 GHz at higher frequencies. The design of the unclad waveguide is shown in Figure 4.20, and it is built upon an EM waveguide by removing a portion of the EM section. The EM section serves to implement all-Si frames that are used in the experiments for handling as well as protection of the unclad waveguide core. The EM section was realized by introducing an array of through holes in a 200-μm thick Si slab with relative permittivity of 11.68, a refractive index of 3.418, and resistivity > 10 kΩ·cm.

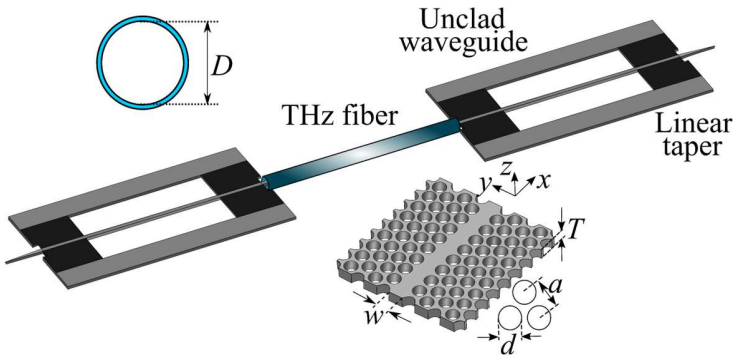

Figure 4.20: Schematic of proposed THz fiber link based on Si waveguide interface.

Values of a = 150 μm, d = 117 μm, and w = 336 μm in the proposed design were obtained after a careful parameter sweep for the optimal wave confinement of the waveguide. The unclad waveguide is terminated by a linear taper on either end to serve as a coupler for both the fiber and hollow metallic waveguide which is necessary to interface with the measurement equipment. Among various taper shapes, linear tapers have been proven to allow the gradual transmission of THz waves with < 0.2 dB loss [56]. The length of the taper has been chosen as 3 mm to optimize coupling efficiency. The design of the waveguide coupler interface is critical for achieving good modal matching between the fundamental mode TE_{11} of the fiber and the E_x mode of the unclad wire waveguide.

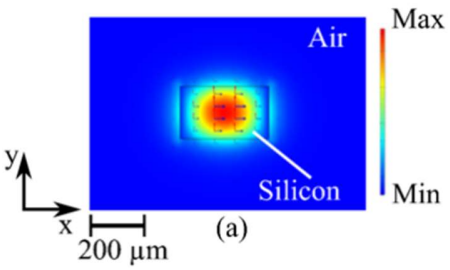

Figure 4.21: Fundamental E_x mode of the Si wire waveguide.

Considering the mode profiles presented in Figure 4.2 (a-c), the Si wire waveguide mode E_x (Figure 4.21) could only be coupled efficiently to the fundamental TE_{11} fiber mode in Figure 4.2 (a). As a result, although the 1-mm core fiber supports five modes, the designed waveguide interface only allows for the unclad wire waveguide E_x mode to be coupled to the fundamental TE_{11} mode of the fiber, thereby achieving quasi-single polarization operation of the fiber.

The performance of a 1-cm long unclad waveguide alone was evaluated in a simulation employing CST Studio to confirm the minimal loss of the unclad waveguide alone, close to the ideal value of 0 dB across 260–380 GHz. Thereafter, the transmittance of each mode of the fiber to the unclad waveguide was analyzed using the same software. The coupling between the unclad waveguide and the fiber was performed through a linear taper that was 3 mm long and fully inserted into the fiber. The results are presented in Figure 4.22 (a) and Figure 4.22 (b) for 1-mm core, and 0.7-mm core, respectively. For the fundamental-mode TE_{11}, the transmittance is very close to the ideal value of 0 dB for both the 1-mm core and 0.7-mm cores. The transmittance of TM_{01} was - 20 dB approximately, which is indicative of the negligible coupling of this mode to the unclad waveguide. This is attributable to the fact that only the E_x mode of the Si wire was excited in this simulation. The value of -20 dB indicates the TM_{01} mode is not strongly coupled to the Si wire waveguides. This has been demonstrated through modal analysis and confirmed by theoretical calculations as well. For the simulations, we employed a PEC circular waveguide as well as a simplified Si wire waveguide with two tapers on wither sides as described in Figure 4.10. This is not the case for the remaining modes, i.e., TE_{21}, TE_{01}, and TM_{11}, which are non-existent in the 0.7-mm core fiber. For the 1-mm core fiber, these modes have a transmittance of < -100 dB. This means that even when a fiber of 1 mm diameter supports

multiple modes, only the fundamental mode TE_{11} is strongly coupled to the unclad waveguide, thus allowing pseudo-single-mode operation.

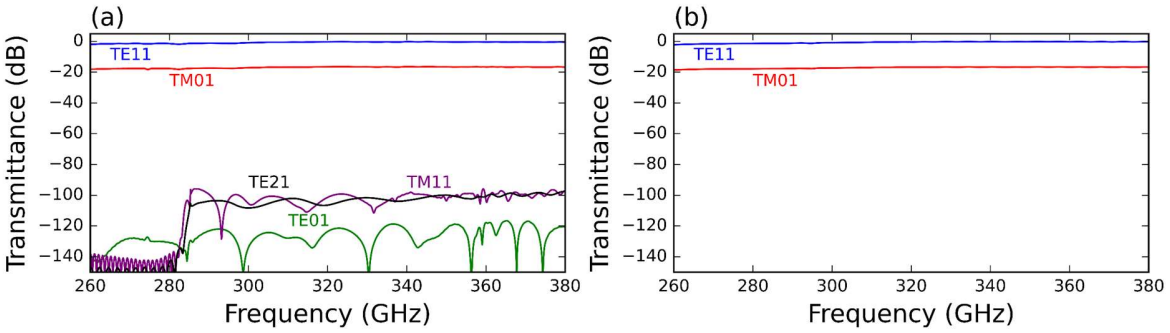

Figure 4.22: Fiber mode coupling to unclad waveguide: (a) 1 mm core fiber, (b) 0.7 mm core fiber.

4.3.2 Communication link proof of concept: Study cases of 0.7-mm core and 1-mm core

Based on the measurements of the fibers, we employed both 1-mm and 0.7-mm core fibers for the realization of high-data-rate fiber links through communication demonstration. THz sources already suffer from limited power [10]. Taking into consideration additional losses from the individual components of the fiber link, a 1-mm core fiber with reduced loss is expected to exhibit better performance. Although multiple modes exist in the 1-mm core fiber, only the fundamental TE_{11} mode is excited through the developed Si waveguide interface, as described previously. Figure 4.23 (a) and Figure 4.23 (b) present the block diagram of the communication experiment and a photograph of the experimental setup, respectively. For demonstration, an AWG delivered data that is used to modulate the optical signal from two laser sources using the OOK modulation scheme. The modulated signal was subsequently amplified by an EDFA and down-converted by a UTC-PD to deliver a THz signal at 320 GHz. The resulting signal was then injected into the unclad waveguide through a metallic hollow waveguide. The unclad waveguide guided the THz waves into the THz fiber through the tapered coupling interface. During detection, a second unclad waveguide is used to interface with a metallic hollow waveguide, which was connected to an SBD. The transmitted data were extracted by the SBD through envelope-detection demodulation. A low-noise amplifier with a bandwidth of 18 GHz was employed to amplify the demodulated signal before it was reshaped

using a limiting amplifier. The corresponding eye diagram and BER were assessed using an oscilloscope and a BERT, respectively.

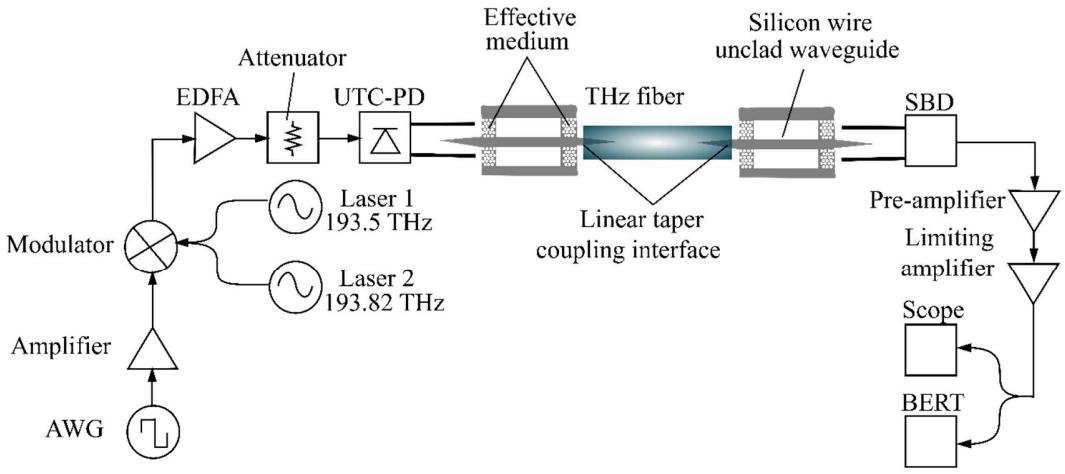

(a)

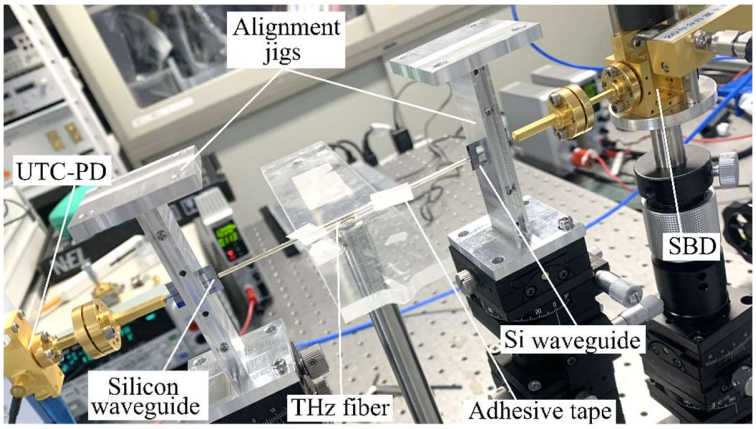

(b)

Figure 4.23: THz fiber link communication experiments: (a) Block diagram, (b) photograph of the experimental setup.

The results presented in Figure 4.24 show the detected BER as a function of the transmitted data rates. For this measurement, an 80-mV bias voltage was applied to the SBD to enhance the sensitivity [135]. Practical error-free (BER of $< 10^{-11}$) communication was achieved at a data rate of up to 22 Gbit/s for the 1-mm core fiber, whereas at 24 Gb/s data rate, the BER increased to 2×10^{-3}. For the 0.7-mm core fiber, the maximum error-free data rate was 14 Gbit/s. This could be ascribed to the exacerbated dispersion phenomenon that further reduced the

dispersion bandwidth of the fiber, which was much lower than the theoretical value of 13 GHz estimated in theory. The eye diagrams for data rates of 10 Gbit/s and 14 Gbit/s for 0.7-mm core fiber, and 18 Gbit/s and 20 Gbit/s for 1-mm core fiber are provided. It can be noticed that both fibers experience some level of amplitude distortion, which is reflected in a high eye-crossing percentage of >80%. Such distortion could be attributed to the failure of the measurement system to perform data pulse symmetry efficiently. Provided eye diagrams also suggest a low signal-to-noise ratio (SNR) for both fibers, resulting in limited data rates of 22Gbit/s and 14 Gbit/s for 1mm-core and 0.7-mm core fibers, respectively. The discrepancy in data rates can be attributed to the higher dispersion of the 0.1 mm core fiber. A comparison of the recorded performance with that of previous works is provided in Table 4.2. In comparison to previous works, the reported fiber link achieved improved data rates under relatively poor SNR, and higher coupling efficiency based on an all-Si coupling interface.

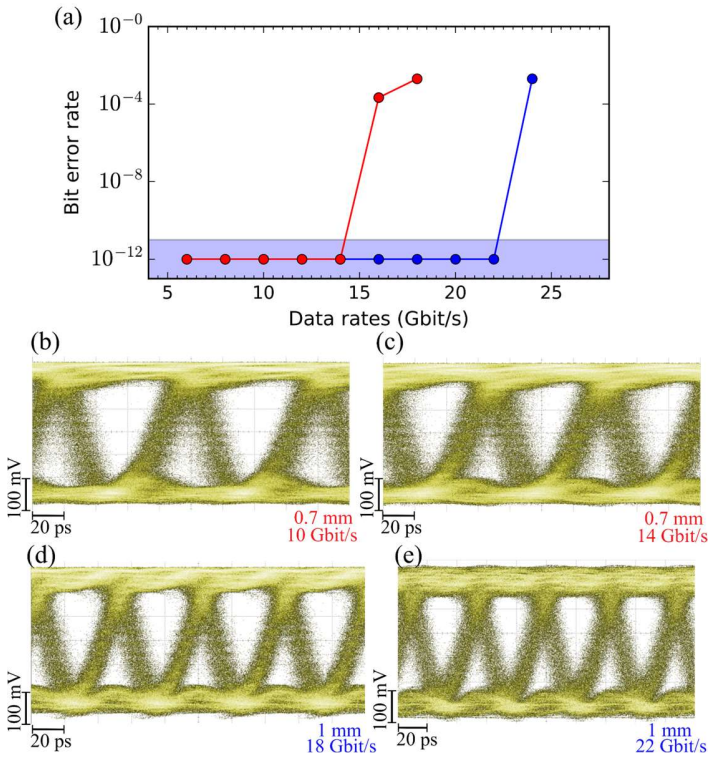

Figure 4.24: Performance of proposed THz fiber link for communication applications: (a) Recorded BER as a function of data rates for 0.7-mm core fiber (red) and 1-mm core fiber (blue) with associated eye diagrams for 0.7-mm core fiber (b-c) and 1-mm core fiber (d-e). The eye reveals that the signal might be distorted, which could be the result of the dispersion of the fiber.

Table 4.2. Comparison between reported THz hollow core fiber links

	Transmission Loss (dB/m)	**Error-free Data Rates (Gbit/s) (Gbit/s)**	**Fiber Length (cm)**	**Coupling Efficiency (%)**
[141]	2	10	100	30
[142]	20	20	25	10
This Work	9	22	10	60

4.4 Application II: Dual polarization over THz hollow core fiber

To demonstrate THz fiber communications for orthogonal polarization input, we employed the experimental setup presented in Figure 4.23 (a). The measured BER versus transmitted data rates are shown in Figure 4.25. It can be observed that the maximum data rates for practical error-free ($<10^{-11}$) were 22 Gbit/s, and 18 Gbit/s for E_x and E_y input, respectively. This accounts for an aggregated data rate of 40 Gbit/s. The associated eye diagrams are presented as inset, and each eye is open, indicative of uninterrupted transmission.

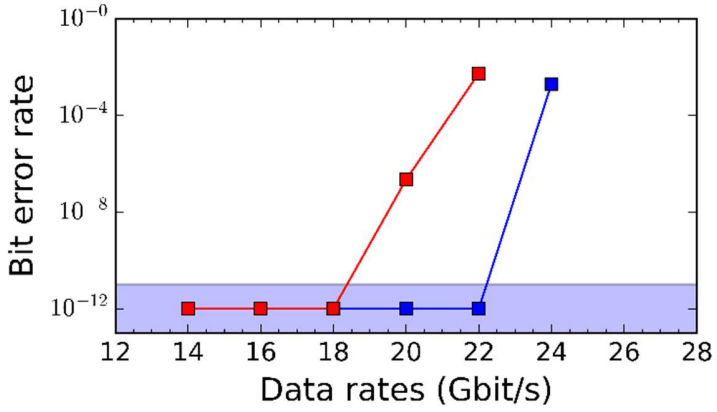

Figure 4.25: Communication experiment: Recorded data rates for E_x (blue) and E_y (red) versus bit error rate with eye diagram for 22 Gbit/s (E_x) and 18 Gbit/s (E_y).

4.5 Application III: HD video transmission over 1m fiber

4.5.1 HD video transmission over 1 m straight THz fiber

The loss estimation of THz fiber as discussed in 4.1.2 revealed that 1m fiber has a total loss of ~9dB for 1m long fiber. We sought to demonstrate practical applications for video transmission employing the 1m fiber. Although the reported loss of 10dB of the fiber is not significant compared to the 30 dB loss reported by previous work, we employed a high-power THz transmitter. The configuration for the experimental setup is presented in Figure 4.26. THz waves are generated through photomixing, by employing two lasers at 192 THz and 192.1 THz. The combination of the two lasers yields a 100 GHz signal that is amplified with an EDFA and modulated with an HD video (1.5 Gbit/s) signal input by a video player. The modulated signal is ×3 multiplied to deliver the THz signal at 300 GHz. This signal is injected into the THz fiber through the unclad waveguide linear taper interface. At the detection, a similar unclad waveguide interface is employed to conduit the transmitted signal into the SBD. The detected signal is amplified and injected into an HD converter before it is displayed. Figure 4.27 shows the demonstration of HD video transmission.

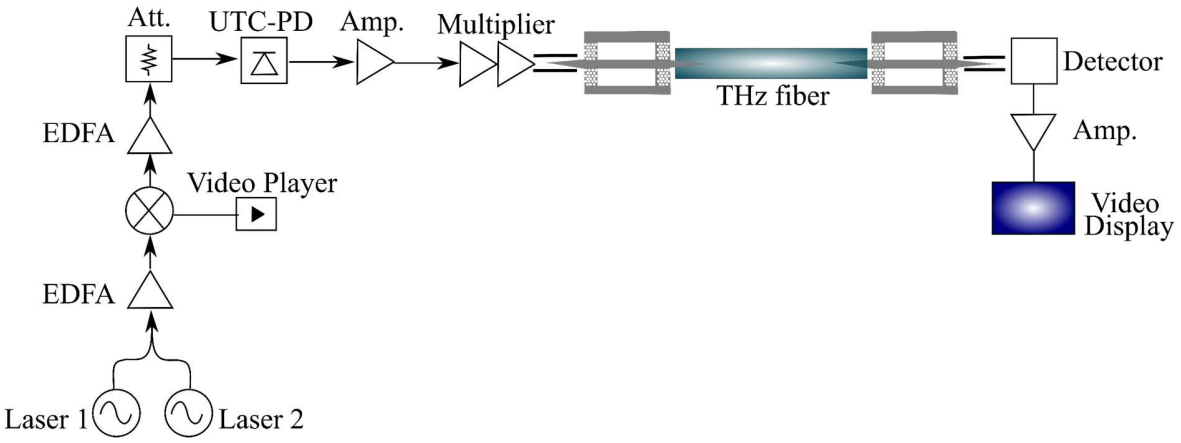

Figure 4.26: Experimental configuration for the demonstration of HD resolution video transmission over 1m straight fiber.

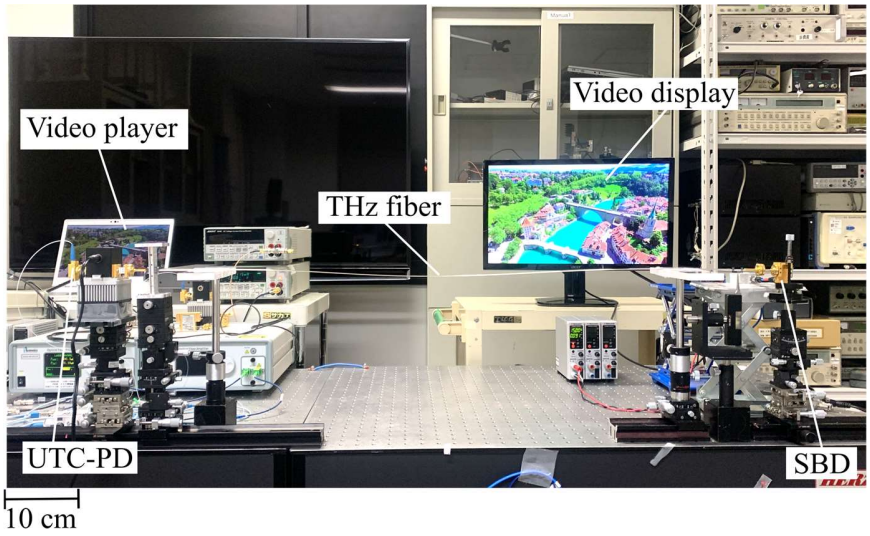

Figure 4.27: HD video transmission over 1m straight fiber.

4.5.2 HD video transmission over 1 m bent fiber

The THz waves experience a few propagation phenomena in wireless communications. The propagation phenomena comprise free-space loss (FSL) [136], atmospheric absorption [137], scattering loss due to surface roughness [138], [139], diffraction [140], and ray shadowing among others. With the increasing frequencies in the THz region, FSL significantly increased. For example, there is a ~41dB loss increase between wireless local area network transmission at 2.4 GHz and THz transmission at 300 GHz[9]. Rough surface scattering loss is of particular interest in cases where the indirect rays play a crucial role in the level of detected power. This is because incident waves to a reflecting object experience specular reflection that can orchestrate loss as high as ~14 dB [9]. Specular reflections are usually associated with diffuse lobes that can account for > 20dB attenuations [141]. Specular reflections can be reduced and even suppressed with the increasing roughness of the surface of the reflecting object, but doing so would increase the level of the diffuse components. This phenomenon is a significant hindrance to THz wireless communications.

Hollow-core THz fiber can be employed for the realization of THz communications using configurations that require bending. In fact, because of the low bending loss of the THz

fiber as shown in Figure 4.9, it is conceivable to realize complex configurations requiring significant bends with THz fiber without employing any reflecting object. This would not be possible in free space because of FSL and also scattering. To investigate this, we employ the configuration shown in Figure 4.28. The system is similar to the one employed for the demonstration of HD transmission through 1m length straight fiber. Here, we bend the fiber following an Omega pattern. This is done to circumvent a physical obstacle that was placed between the transmitter and the receiver. We achieved the demonstration of HD resolution video transmission over the 1m fiber bend as shown in Figure 4.29.

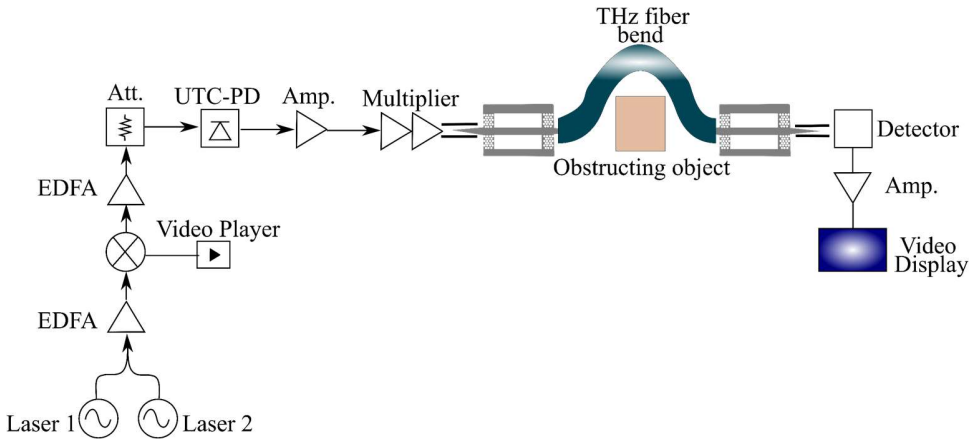

Figure 4.28: Experimental configuration for the demonstration of HD resolution video transmission over 1m bent fiber.

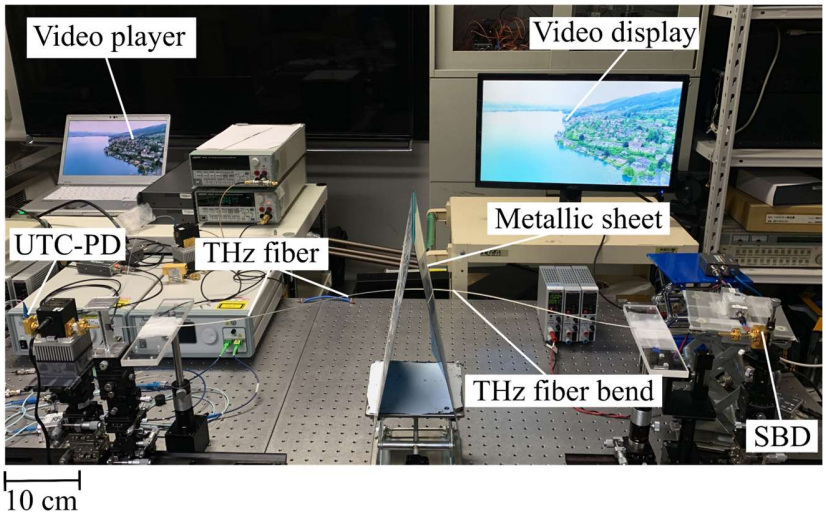

Figure 4.29: HD video transmission over 1m straight fiber.

Chapter 5

Conclusions and perspectives

5.1. Conclusions

In this doctoral thesis, ultra-broadband Si waveguides were proposed. We have detailed the analysis, design, and characterization of EM waveguides and unclad waveguides for operation in the WR-1 band, covering frequencies from 0.75 THz to 1.1 THz. We have established the design principles as well as the techniques for testing and evaluating waveguides of this sort with small features at extremely high frequencies. Subsequently, we developed packaged compact modules for these waveguides to serve, as well as a Y-junction module for the demonstration of THz high-resolution imaging at 0.9 THz. To increase the THz communication throughout, we demonstrated dual orthogonal polarization over dielectric unclad waveguide and hollow core fiber. We employed a dielectric waveguide coupler for interconnection with hollow core fiber, resulting in 60% coupling efficiency. Finally, we demonstrate flexible, low-loss, and low-cost THz-range hollow core fiber links. The developed hollow core fiber links implemented an all-Si tapered waveguide interface as a coupler. Employing such a link, we demonstrated improved data rates via the THz range communication link.

Chapter 1 clarifies the research goals of this dissertation by identifying the interconnect gap, which is a major performance bottleneck in THz range systems. The interconnect gap arose from the limitations of the current network and the needs for future networks. Specifically, we

detailed the shortcoming of THz wireless communications, to highlight the possible contributions of THz wired communication links. Afterward, we surveyed the empirical THz range waveguides including metallic hollow waveguides (circular and rectangular), planar transmission lines (coplanar, microstrip, and stripline), and dielectric coated waveguides to confirm the high loss of those waveguides. In addition, we confirmed the low loss performance of the dielectric waveguides in the order of 0.1 dB/cm. We thereafter reported THz dielectric waveguides (photonic crystal waveguides, EM waveguides, and unclad waveguides) that confirmed superior performance in achieving very low loss and positioned themselves as an efficient canvas for the realization of THz range integrated components and systems. This chapter concludes with a summary of the research goals, namely the development of low loss dielectric waveguide in the WR-1 band (0.75 – 1.1 THz), the establishment of low-loss, low-cost, and flexible hollow core fibers as efficient THz range interconnects, and finally the research effort toward achieving higher data rates communication links by leveraging dual polarization over unclad waveguide, and hollow core fiber to demonstrate polarization multiplexing.

In chapter 2, the detailed design of all-Si EM and unclad waveguides is provided. We highlighted the challenges related to the design of waveguides with small dimensions, and we established empirical design techniques, leading to very low loss performance of both waveguides. For the establishment of low-loss waveguides in the WR-1 band, we conducted a theoretical analysis of the EM theory, that confirmed that the refractive index of the EM needed to be further reduced to meet the minimum manufacturable dimension of 10 µm. We thereafter conducted a parametric study focused on the key performance driver of the waveguide, including the waveguide width W and the waveguide thickness. We achieved an optimum design with the values of $W = 100$ µm and $T = 80$ µm. With those design parameters, we reported a world-record bandwidth of 350 GHz. We confirmed in experiments a propagation loss of 0.15 dB/cm, and <0.1 dB/cm for the EM waveguide and the unclad waveguide, respectively. The coupling loss for the unclad waveguide and the EM waveguide was 0.9 dB, and 0.5dB respectively. The achieved results represent a benchmark to build upon for subsequent waveguides in a similar operation frequency range or higher. We demonstrated two applications

for these waveguides: Packaged WR-1 band modules and Packaged Y-junction module that was employed to demonstrate high-resolution THz imaging.

In Chapter 3, we investigated the possibility of increased data rates THz communication with dual orthogonal polarization dielectric unclad waveguide. We demonstrated dual polarization over a dielectric unclad waveguide with recorded data rates of 24 Gbit/s for E*x* and 22 Gbit/s for E*y*. These results confirmed the possibility of achieving >40 Gbit/s combined data rates with simultaneous transmission by implementing polarization multiplexing. We thereafter reported a dielectric diplexer, that confirmed in both theory and experiments polarization differentiation can be implemented with the diplexer.

In chapter 4, we reported an efficient hollow core fiber based on a low-loss dielectric waveguide coupler. Here, we have explored different waveguide interfaces including single rod antenna interface, rod array antenna interface, and 2D semi-hemispherical lens interface. The analysis of the different interfaces confirmed coupling efficiencies of 45%, 80%, and 40% for the single rod interface, the rod array interface, and the 2D lens interface, respectively. The rod array interface was chosen for subsequent implementations, owing to the simplified structure. Employing the single rod interface, we have also studied the fundamental properties of hollow core fibers, including the modal analysis of the fiber, as well as the dispersion. Our analysis revealed that the number of modes supported by the hollow core fiber increases with the fiber diameter. Specifically, for 1 mm core fiber, five modes including TE_{11}, TM_{01}, TE_{21}, TM_{11}, and TE_{01} were supported, whereas for the 0.7 mm core fiber, only TE_{11}, and TM_{01} were supported. The dispersion analysis of the fiber confirmed a 3dB dispersion bandwidth of 28 GHz, and 13 GHz for a 0.7 mm core, respectively. The power probing of the hollow core fibers confirmed loss of 1 dB and 1.5 dB for 10 cm long with 1 mm core, and 1.5 mm core fibers respectively. This fundamental study allows for a better understanding of the operation principle of the fiber, which allows us to unlock interesting applications for THz communications by confirming data rates of 22 Gbit/s, and 14 Gbit/s for 1 mm core fiber, and 0.7 mm core fiber, respectively.

The technologies proposed in this dissertation, as well as the techniques for their practical evaluations in experiments, are applicable for operation in higher frequencies, beyond 1 THz. More specifically, the parametric analysis on the impact of the waveguide with and thickness is a valid design process for dielectric waveguides operating > 1THz. The packaging

technology proposed for the development of low-loss waveguide modules is an effective design strategy for not only waveguides and passive components, but also active devices, and heterogenous hybrid integrated components. The estimation of the loss of the waveguides employing the curve-fitting methods was also effective in the case of THz fiber and is applicable for THz fiber operating beyond 1 THz.

5.2. Perspectives

5.2.1 THz waveguides and THz hollow core fiber for intra-/inter-chip interconnection

Intra-/inter-chip I/O bandwidth doubles every two years creating an increased gap between the number of I/O pins and the bandwidth density, which is defined as the transmitted data per I/O pin. Such bandwidth requirements together with the need for high-speed communication applications are the major bottlenecks for intra-chip interconnects that relays communications among CPU cores and high-speed processing units, but also inter-chip interconnects for communications between chips. Both electrical interconnects [142]–[146] and optical interconnects [147]–[149] are commonplace in research laboratories depending on the application. Optical interconnects have reported very little loss, and high-efficiency light sources are compatible with CMOS platforms [149], whereas electrical interconnects are suitable for large-scale photonic integration although metallic transmission media experience severe conduction losses. Sub-THz and THz range waveguides are prime candidates to solve the bandwidth density, as well as the power efficiency issues faced by intra-/inter-chip, interconnects. That is, the Sub-THz range interconnects operate at frequencies between optical and microwave frequencies, and thus benefit from the low-loss feature of optical interconnects, but also the high-speed features of semiconductor devices.

In this section, we expound on the potential of the waveguide technologies discussed throughout this thesis including THz dielectric waveguides and THz hollow core fibers for the realization of high bandwidth, seamless interconnections for boards configurations in data centers, focusing on short-length interconnections up to 10 cm.

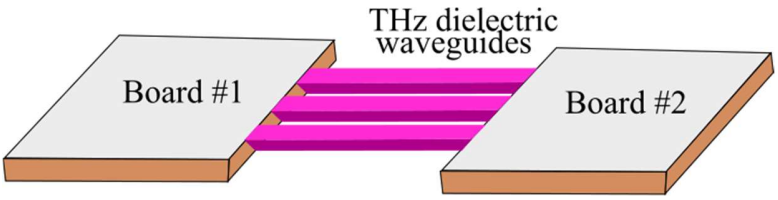

Figure 5.1. Concept of hybrid, free-standing THz, and optical sub-systems type I: THz Si waveguides for intra-board interconnections.

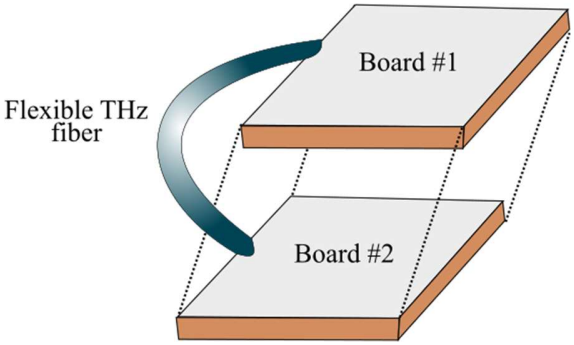

Figure 5.2. Concept of hybrid, free-standing THz, and optical sub-systems type II: THz fiber for inter-board interconnections.

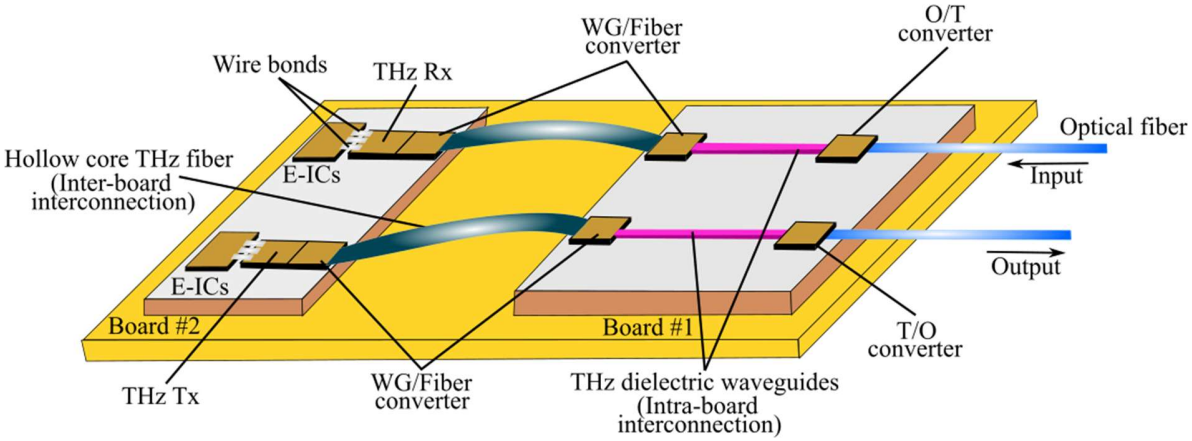

Figure 5.3. Concept of hybrid, free-standing THz, and optical sub-systems type III: THz Si waveguides for intra-board interconnections, and THz fiber for inter-board interconnections.

The configuration illustrated in Figure 5.3 will allow for the improvement of the bandwidth density, as THz range interconnects are very broadband, but also the improvement of power efficiency by the introduction of THz sources. The concept illustrated in Figure 5.3 is

the ultimate configuration based on the realization of board-to-board type configurations of Type I and Type II presented in Figures 5.1 and Figure 5.2, respectively. Type I of board-to-board configuration presented in Figure 5.1 illustrates the use of THz dielectric waveguide as interconnects between two boards in the same dimension, in this case, the horizontal plane. The introduction of such broadband THz dielectric waveguides would allow for the improvement of the bandwidth density and the number of pins in data center units. Type II of the board-to-board configuration illustrated in Figure 5.2 shows the realization of a 3D-like configuration with two boards in planes that are horizontally parallel. For such a configuration, flexible interconnects are crucial. In Chapter 4, we introduced hollow-core THz fibers, as flexible, low-loss, and low-cost interconnect. The final configuration Type III as illustrated in Figure 5.3 shows that the realization of an optical-THz hybrid platform requires several components such as dielectric waveguides, THz range transmitters (Tx) and receivers (Rx), and optical/THz (O/T), THz/optical (T/O), waveguide/fiber (WG/Fiber), and fiber/waveguide (Fiber/WG) converters.

There is extensive supporting research for the realization of planar integrated circuits based on THz waveguide technologies. More recent research has focused on leveraging THz all-silicon dielectric waveguides as a canvas for the realization of such hybrid circuits. THz-enabled integrated circuits can be categorized into three main generations. Each generation was facilitated by various passive waveguides, but also active devices such as resonant tunneling diodes (RTDs), mixers, etc. Waveguide platforms have reported very broadband operation that positively impacts the bandwidth density, whereas RTDs have reported high output power, with the potential of improved energy density. The generations of THz integrated circuits can be summarized as follows:

- First generation: Photonic crystal waveguides were the canvas for the development of the first generation of THz integrated components and systems. These waveguides relied on PBG for THz wave confinement. Although these waveguides exhibited low loss and low dispersion, their typical bandwidth was limited. Together with the development of THz dielectric waveguides, a lot of research effort went into the development and integration of resonant tunneling diodes into planar waveguide platforms. At this stage, RTDs were integrated into end-fire patch antennas and coupled to the THz waveguide

platform through the parallel coupling scheme and the end-fire coupling scheme as illustrated in Figure 5.4.

- ❖ Second generation: The second generation of interconnects sought to improve the bandwidth. That led to EM waveguides and unclad waveguides. These waveguides achieved broadband operation and very little loss. Such waveguides, integrated with active devices such as RTDs, have allowed the realization of the second generation of THz-integrated components and systems. For the coupling of the RTDs to the waveguide platforms, the embedded coupling scheme reported a very high coupling efficiency of ~60% [119]. Further improvement of the coupling efficiency was possible by adding a parasitic InP portion on top of the RTD chip [150].
- ❖ Third generation: The interconnects studied in this thesis will be at the center of the third generation of THz integrated systems, together with novel topological waveguides. Novel techniques for coupling active devices to all-dielectric waveguide platforms such as the backside coupling technique will be crucial. The backside coupling technique reported a coupling efficiency of 70% without any additional parasitic element.

The waveguide technologies and their applications by generation are in Table 5.1, and we further discuss future research axes and technologies that can be integrated with the waveguides studied in this thesis, toward to realization of large-scale integrated THz systems.

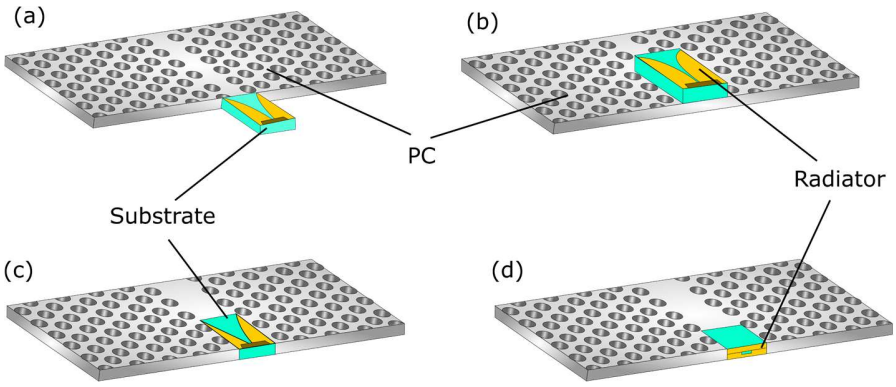

Figure. 5.4 Various coupling schemes between RTD chip and THz Si waveguide platform: (a) End-fire technique, (b) Parallel technique, (c) embedded technique, and (d) backside coupling technique.

Table 5.1: Si waveguides by generation

Generation	Waveguide technology	Hybrid integration of active device	Demonstrated application	Comments
First-generation	Photonic crystal	Parallel coupling End-fire coupling	THz sensor [63]	Early stages of THz integrated components based on photonic crystals
Second generation	Photonic crystal EM Unclad	Embedded coupling	- THz fiber communications [151][152] -THz imaging [76][77] - Wireless communications [153]	High-performance waveguides for enhanced THz IC components
Third generation	Photonic crystal EM Unclad Topological	Embedded coupling Backside coupling	On-going	Towards large scale integration based on all-Si platform: Enabling technologies

Technology	Impact
High precision machining	Accurate manufacturing of devices with nanoscale features
High-power THz sources	Self-sufficient THz emitters for long-range and high-data rates communications
Array technology for THz diodes	High-output THz sources and high-sensitivity THz detectors
Development of coherent oscillators	Unlock multi-level modulation schemes

Record-breaking data rates of 240 Gbit/s and 192 Gbit/s were reported on a single optical career by leveraging optical to sub-THz conversion using a plasmonic modulator, over 115 m, without the need for an electrical amplifier [154]. The reported link employed a UTC-PD to map optical frequencies to THz frequencies. UTC-PDs are quintessential THz sources that are frequently employed in the process of photomixing for the generation of THz carrier frequencies.

These results confirm the potential of the combination of THz carriers to bridge optical links. This is because THz carrier frequencies can transmit the highest capacities. High data rates of 1056 Gbit/s were achieved over a distance of 2.8 m [155]. Other studies have reported data rates of 100 Gbit/s [156], 300 Gbit/s [157], and 600 Gbit/s [158] over 20 m, 110 m, and 0.5 m, respectively. These performances were possible over THz transmission links using direct optical-to-RF conversion performed by a UTC-PD at the transmitting unit, and RF-to-optical conversion at the receiving unit. The RF-to-optical conversion is generally followed by a down-conversion process where the THz signals are mixed to a baseband or intermediate frequency. This is because there are no viable solutions for the direct mapping of THz information into optical carriers. In this regard, electro-optical (EO) modulators are very crucial, as they permit the direct mapping of RF signals to optical carriers. With EO modulators, the achievable data rates are usually dependent on the bandwidth of the modulator. As a result, the data rates of most communication links are limited by the typical 80-GHz bandwidth of the EO modulators [159]–[162]. However, as was reported in [163] it is possible to realize direct RF-to-optical conversion solely based on broadband plasmonic devices. This could be achieved by integrating a resonant antenna with a plasmonic modulator. There have been many reports on integrated antennas [71], [74], [82], [164] that could be prime candidates for the realization of broadband RF-to-optical conversion. The realization of a free-standing hybrid THz and optical sub-system as described in Figure 5.1 will require interconnects with high bandwidth density and high power efficiency. Table 5.2 summarizes the performance of the state-of-the-art interconnects for bandwidth density. As can be observed, the bandwidth density of the Si waveguides reported in this doctoral thesis is superior to existing solutions offered by CMOS foundries. This is due to the record high bandwidth performance of 350 GHz in the WR-1 band (0.74 – 1.1 THz) combined with the small dimensions of the waveguide's core (100 μm × 80 μm).

5.2.2 High-power and high-sensitivity THz detectors and transmitters

Another critical performance bottleneck of both optical and THz systems is energy efficiency. High-data rates communication links built with optical-RF transmission and RF-optical detections require down-conversion owing to the lack of encoders to map THz

information onto optical carriers. Such down-conversion has put a limit on the performance in terms of data rates, but also because of the small level of the detected signal. It is therefore crucial to employ high-output THz transmitters and high-sensitivity detectors to compensate for the losses occurring in the communication link. In the THz region, resonant tunneling diodes have reported high output power in the orders of 400 μW at 530 – 590 GHz [165]. As a result, RTDs are prime candidates for the realization of both transmitters and detectors of high energy efficiency. That is, the high output power, with operation at high frequencies in the THz region will enable an increase in power efficiency. Specifically, a power efficiency of ~10 PJ/bit was reported for RTD and could be further improved to less than 1 PJ/bit considering higher output RTDs. One way to achieve that would be the array configuration of RTDs. Preliminary results have reported 0.73 mW and 10 mW THz sources based on 89-elements [166] and 36-elements [167] RTD arrays, respectively. Although RTD can be employed as a detector too, there is a broad range of THz detectors with small area sizes that could be suitable converters capable of implementing broadband down-conversion while maintaining a sufficient detected power level. Detectors such as Fermi barrier diodes (FMBD), SBD, and laser diodes can be employed for the conversion of type baseband (BB) to THz, THz to BB, O-T, and T-O. Table 5.3 summarizes the performance of Si photodetectors in comparison to THz detectors. It can be observed that THz detectors have a higher sensitivity than SiGe photodetectors and could therefore be competitive alternatives for the implementation of hybrid THz optical communications.

Table 5.2 Interconnection for chip-to-chip communications: Comparative performance of Si photonic waveguides and THz waveguides

	Platform	Frequency (GHz)	Length (cm)	Medium	Loss (dB)	Cross-section area (mm^2)	Data rates (Gbit/s)	Bandwidth density ($Gbit/mm^2$)
Si photonics waveguides	CMOS [168]	135	10	Air		2	10	7.1
	SOI [169]	-	-	Fiber		-	25	-
THz waveguides	This work	750 - 1100	5	Si crystalline	< 0.5	0.008	30	3,750

Table 5.3 Interconnection for chip-to-chip communications: Comparative performance of Si photonics photodetectors and THz photodetectors.

Si photonics SiGe photodetectors	Foundry	AIM Photonics [170]	Cea Leti [171]	Imec [172]
	Bandwidth (GHz)	50	35	50
	Responsivity (A/W)	1	0.75	0.9
THz detectors	Devices	SBD InP [173]	FMBD InP [174]	RTD InP [175]
	Operation frequency (GHz)	399 GHz	140 – 160	340
	Sensitivity (kV/W)	7.00	10^6-10^5	16

Appendix

Appendix 1: Positioning jigs for accurate testing of WR-band waveguides

We confirmed in practice the worst performance of the coupling between the linear taper and hollow core fiber as a direct result of manual manipulations for the insertion and positioning of the taper within the hollow core fiber. That has led to further considerations to increase the positioning and alignment of the taper. We devised an alignment jig as presented below for better positioning of the Si waveguides, aided by micro stages for precision insertion. The devised jigs are presented in Figure S1. The jigs consist of top and bottom parts, serving as a lid and base. In both the lid and the base, a shelf of 40 µm depth was carved out to house the Si waveguide, which has a thickness of 80 µm. Above and below the shelf a trench deep enough to avoid any interference of the metallic base on the inherent behavior of the waveguide was cut out. The steps for the assembly of the jigs are summarized in Table S1, and the assembled jig is presented in Figure S1 (b).

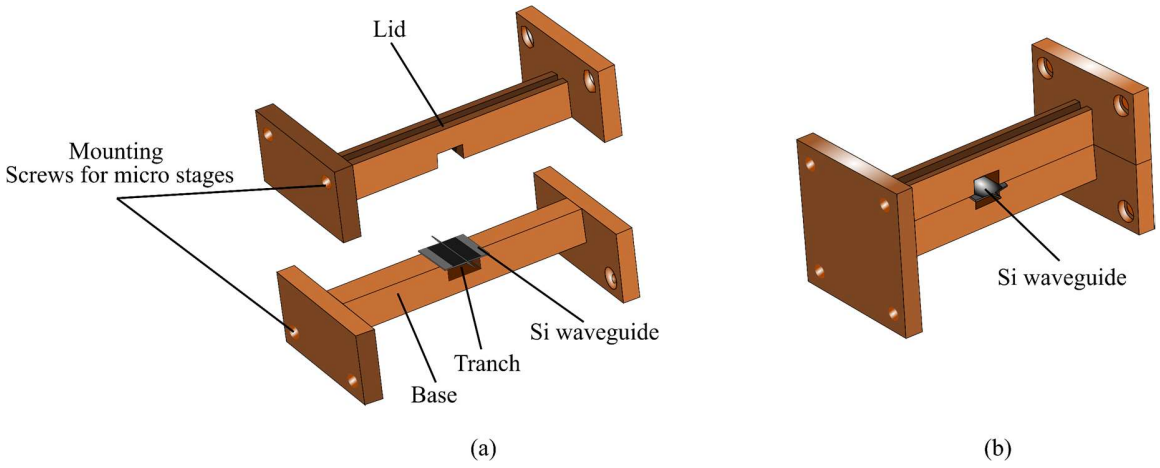

Figure S1: Design of positioning jigs, (a) assembly showing lid and base with Si waveguide, (b) assembled jig.

Table S1 Assembly steps of the positioning jigs

Step n°	Procedure
1	Secure the Si waveguide onto the base
2	Affix the lid using screws
3	Securely assembled jig onto the micro stage

Appendix 2: Cutoff frequencies of circular waveguides

In Chapter 4, we introduced THz hollow core fibers as efficient low-loss, low-cost and flexible interconnect that can be leveraged for the realization of inter-chip communications. The analysis of hollow core fiber was done considering a metallic circular waveguide of radius *r*. Considering a source-free, isotropic, and homogenous propagation region of the waves in the circular waveguide, Maxwell's equations can be approximated as follows:

$$\nabla \times \bar{E} = -j\omega\mu\bar{H} \qquad (S\text{-}1)$$

$$\nabla \times \bar{H} = j\omega\epsilon\bar{E} \qquad (S\text{-}2)$$

where $\bar{E}$ is the electric field, $\bar{H}$ the magnetic field, and μ and ϵ respectively the permeability and permittivity of the propagation medium.

Solving equations (S-1) and (S-2) for TE, we can deduct the cutoff frequency for the TE_{nm} modes as:

$$f_c = \frac{P_{nm}{}' c}{2\pi r\sqrt{\mu\varepsilon}} \qquad (S\text{-}3)$$

where P'_{nm} represents the zeros of Bessel functions of the first kind and c is the velocity of light in free space. The values for $P_{nm}{}'$ are given as constants following:

TableS1 Values of P'_{nm} for TE modes of a circular waveguide

n	$P_{n1}{}'$	$P_{n2}{}'$	$P_{n3}{}'$
0	3.832	7.016	10.174
1	1.841	5.331	8.536
2	3.054	6.706	9.970

Solving equations (S-1) and (S-2) for TM, we can deduct the cutoff frequency for the TM$_{nm}$ modes as:

$$f_c = \frac{P_{nm} c}{2\pi r\sqrt{\mu\varepsilon}} \qquad (S\text{-}4)$$

where P_{nm}represents the zeros of the Bessel functions of the first kind for TM modes. The values of P_{nm} are given as constants following:

TableS2 Values of P_{nm} for TM modes of a circular waveguide

n	P_{n1}	P_{n2}	P_{n3}
0	3.405	5.520	8.654
1	3.832	7.016	10.174
2	5.135	8.417	11.620

Appendix 3: Direct coupling between rectangular metallic waveguide and hollow core THz fiber

Measurement equipment is commonly coupled with hollow metallic waveguides as interfaces to interconnect with the devices and components under test. In Chapter 4, we introduced various interfaces such as single rod linear taper to serve as a coupler for the hollow core THz fiber. This was done to increase the accuracy of measurement using standard hollow metallic waveguides, as we suspected a direct coupling between the metallic hollow waveguide and the THz fiber would not yield good performance. We investigated the performance of the direct connection between the metallic rectangular hollow waveguide and the THz fiber as illustrated in Figure S1. The power transmittance of the direct coupling was probed by transmitting THz waves through Port 1 and measuring the detected power at Port 2. The results are presented in Figure S2 (b). The power transmittance from Port 1 to Port 2 is ~-5 dB on average, which is indicative of non-negligible losses at the interface where the rectangular hollow waveguide comes into contact with the THz fiber, owing to physical dimensions mismatch, but also mode mismatch. That is, the rectangular waveguide supports single polarization depending on the exciting signal. Without an adequate polarization converter or selector between the rectangular waveguide and the THz fiber, a modal mismatch is most likely to occur, leading to poor performance. This realization has led to the development of an all-Si linear taper coupler, that yielded ~60% coupling efficiency.

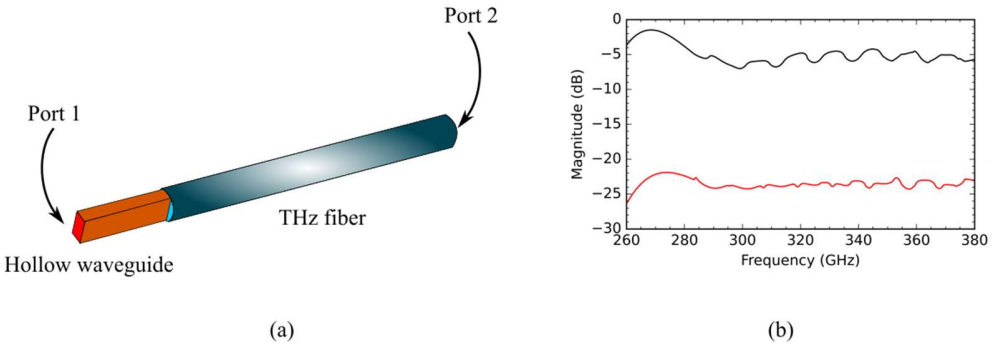

Figure S2: Direct coupling between rectangular metallic waveguide and hollow-core THz fiber: (a) Simulation model, (b) transmittance (black) and reflection (red).

Appendix 4: Impact of Si taper alignment in a hollow-core fiber

A linear taper coupler is introduced in chapter 4 to enable efficient interconnection between the Si waveguide and THz hollow core fiber. Considering a fiber of 1 mm diameter, the impact of the alignment of the linear taper with the hollow core fiber is aligned following the configuration presented in Figure S3.

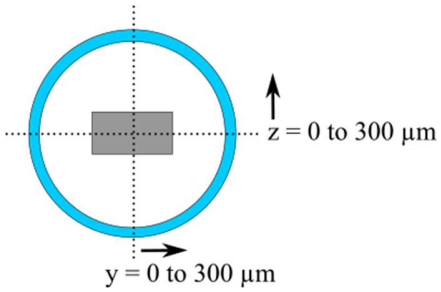

Figure S3: Configuration for the investigations of y- and z-axis shift impact

The impact of alignment was analyzed by shifting the linear taper along the *z*- and *y*-axis, up to 300 µm, considering the limit of 500 µm to avoid direct contact with the walls of the fiber. The results are presented in Figure S4 (a-b) for 280 GHz, Figure S4 (c-d) for 320, and Figure S4 (e-f) for 360 GHz. As a general observation, the misalignment loss is not as significant and only increases at the extremities, where *z*-shift and *y*-shift = 300 µm. In this case, a maximum loss of -6 dB is observed at 360 GHz, against a loss of ~ -4.5 dB at 280GHz and 320 GHz. Higher losses can be predicted for the worst case, where the Si linear taper is in direct contact with the hollow core fiber.

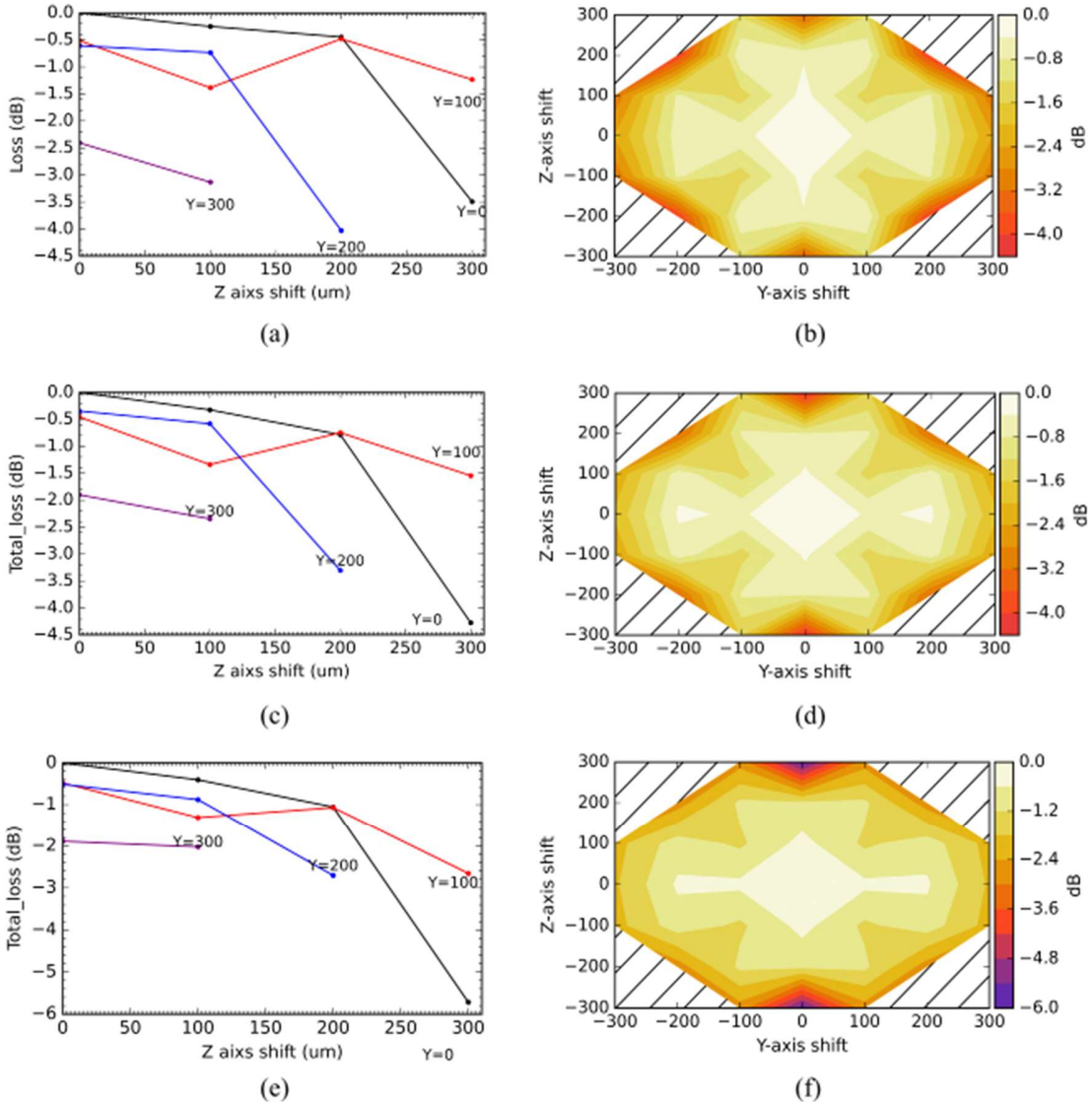

Figure S4: Loss caused by the misalignment of Si taper within the THz fiber for 280 GHz (a-b), 320 GHz (b-c), and 360 GHz (e-f). The graphs show the loss of the *y*-axis shift of 0, 100, 200, and 300 μm. The colormaps show the loss caused by the *y*-axis and *z*-axis shifts.

Appendix 5: Impact of Si taper tilt within the hollow-core fiber

The loss caused by the tilt on the linear taper inside the THz fiber was also investigated following Figure S5 For the investigations, the linear taper was tilted by an angle varying between 0° and 15°. The results are presented in Figure S6. The results concluded that a small tilt does not have a big impact on performance. Yet, a much more important tilt could lead to a rotation of the polarizations of the Si wire, which could create further losses. This realization created an urgency for the development of efficient testing methods.

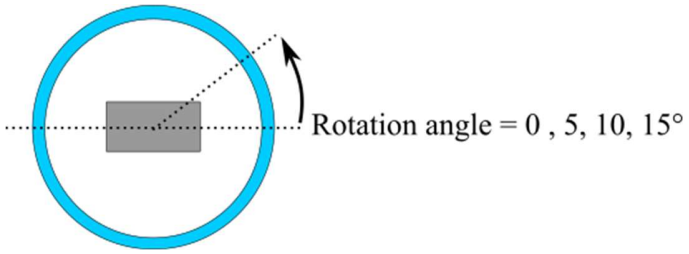

Figure S5: Configuration for the investigations of rotation impact.

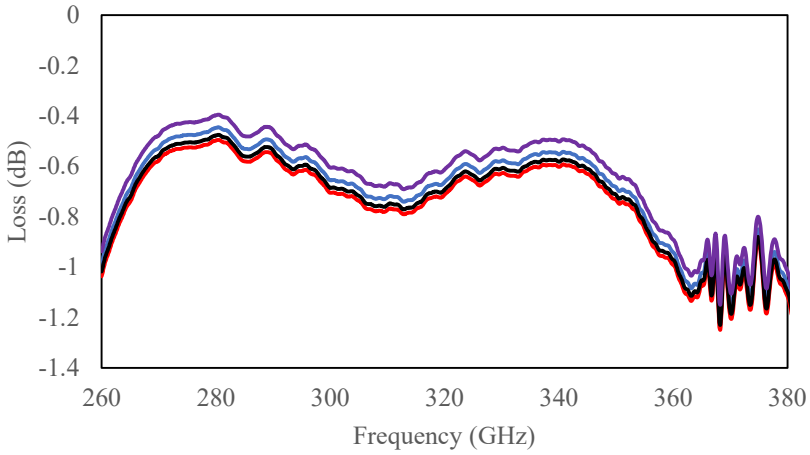

Figure S6: Loss caused by linear taper rotation within hollow core THz fiber. Blue, red, black, and purple lines denote rotations of 0, 5, 10, and 15°, respectively.

List of abbreviations

2D	Two Dimensional
3D	Three Dimensional
5G	Fifth Generation of mobile network
6G	Sixth Generation of mobile network
AWG	Arbitrary Wave Generator
BER	Bit Error Rate
BERT	Bit Error Rate Tester
DMM	Digital Multimeter
EDFA	Erbium-Doped Fiber Amplifier
E-IC	Electronic – Integrated Circuit
EM	Effective Medium
ePTFE	expanded polytetrafluoroethylene
FC	Ferrule Connector
Ge	Germanium
GMM	Guided waves by Metallic Media
HMD	Head-Mounted Device
I/O	Input/Output
IC	Integrated Circuits
IoT	Internet of Things
IR	Infrared

LED	light-emitting Diode
LO	Local Oscillator
O/T	Optical/THz
OOK	On-OFF keying
PBG	Photonic Band Gap
PIC	Photonic Integrated Circuit
SBD	Schottky Barrier Diode
Si	Silicon
SiO_2	Silicon dioxide
SMA	Sub-Miniature A
SOI	Silicon On Insulator
TE	Transverse Electric
THz	Terahertz
TIR	Total Internal Reflection
TM	Transverse Magnetic
UTC-PD	Uni-Traveling-Carrier Photodiode
WG/Fiber	Waveguide/Fiber

References

[1] T. S. Rappaport *et al.*, “Millimeter wave mobile communications for 5G cellular: It will work!,” *IEEE Access*, vol. 1, pp. 335–349, 2013.

[2] J. Ma, R. Shrestha, L. Moeller, and D. M. Mittleman, “Invited Article: Channel performance for indoor and outdoor terahertz wireless links,” *APL Photonics*, vol. 3, no. 5, 2018.

[3] T. S. Rappaport *et al.*, “Wireless communications and applications above 100 GHz: Opportunities and challenges for 6g and beyond,” *IEEE Access*, vol. 7, pp. 78729–78757, 2019.

[4] J. A. Shaw, “Radiometry and the Friis transmission equation,” *Am. J. Phys.*, vol. 81, no. 1, pp. 33–37, 2013.

[5] P. Tang et al., "Channel measurement and path loss modeling from 220 GHz to 330 GHz for 6G wireless communications," *China Coms*., vol. 18, no. 5, pp. 19-32, 2021, doi: 10.23919/JCC.2021.05.002.

[6] V. Petrov, D. Moltchanov, and Y. Koucheryavy, “Interference and SINR in dense terahertz networks,” *IEEE 82nd Vehicular Technol. Conf.,* 2016.

[7] T. Nagatsuma, “Terahertz technologies: Present and future,” *IEICE Elec. Express*, vol. 8, no. 14, pp. 1127–1142, 2011.

[8] H. J. Song and T. Nagatsuma, “Present and future of terahertz communications,” *IEEE Trans. Terahertz Sci. Technol.*, vol. 1, no. 1, pp. 256–263, 2011.

[9] H. J. Song and T. Nagatsuma, *Handbook of terahertz technologies: Devices and app.*, 1st ed. 2015.

[10] R. A. S. D. Koala, M. Fujita, and T. Nagatsuma, “Nanophotonics-inspired all-silicon waveguide platforms for terahertz integrated systems,” *Nanophotonics*, vol. 11, no. 9, pp. 1741–1759, 2022.

[11] D. J. Harris, “Waveguides for the 100–1000 GHz frequency range,” *Radio Electron. Eng.*, vol. 49, pp. 389–394, 1979.

[12] G. Gallot, S. P. Jamison, R. W. McGowan, and D. Grischkowsky, “Terahertz waveguides,” *J. Op. Soc. Am. B*, vol. 17, no. 5, p. 851, 2000.

[13] O. Mitrofanov, R. James, F. A. Fernández, T. K. Mavrogordatos, and J. A. Harrington, “Reducing transmission losses in hollow THz waveguides,” *IEEE Trans. Terahertz Sci. Technol.*, vol. 1, no. 1, pp. 124–132, 2011.

[14] C. D. Nordquist, M. C. Wanke, A. M. Rowen, C. L. Arrington, M. Lee, and A. D. Grine, “Design, fabrication, and characterization of metal micromachined rectangular waveguides at 3 THz,” *IEEE Int. Symp. Antennas Propag.*, pp. 3–6, 2008.

[15] Online. Available at: www.vadiodes.com (accessed: January 2023).

[16] R. Mendis and D. Grischkowsky, “Undistorted guided-wave propagation of subpicosecond terahertz pulses,” *Opt. Lett.*, vol. 26, no. 11, p. 846, 2001.

[17] Y. Matsuura and E. Takeda, “Hollow optical fibers loaded with an inner dielectric film for terahertz broadband spectroscopy,” *J. Op. Soc. Am. B*, vol. 25, no. 12, p. 1949, 2008.

[18] B. Bowden, J. A. Harrington, and O. Mitrofanov, “Low-loss modes in hollow metallic terahertz waveguides with dielectric coatings,” *Appl. Phys. Lett.*, vol. 93, no. 18, 2008.

[19] M. Navarro-Cía, M. S. Vitiello, C. M. Bledt, J. E. Melzer, J. A. Harrington, and O. Mitrofanov, “Terahertz wave transmission in flexible polystyrene-lined hollow metallic waveguides for the 25-5 THz band,” *Opt. Express*, vol. 21, no. 20, p. 23748, 2013.

[20] O. Mitrofanov, R. James, F. A. Fernández, T. K. Mavrogordatos, and J. A. Harrington, "Reducing transmission losses in hollow THz waveguides," *IEEE Trans. Terahertz Sci. Technol.*, vol. 1, no. 1, pp. 124–132, 2011.

[21] P. Doradla, C. S. Joseph, J. Kumar, and R. H. Giles, "Characterization of bending loss in hollow flexible terahertz waveguides," *Opt. Express*, vol. 20, no. 17, p. 19176, 2012.

[22] M. Navarro-Cía, J. E. Melzer, J. A. Harrington, and O. Mitrofanov, "Silver-Coated Teflon Tubes for Waveguiding at 1–2 THz," *J. Infrared Millim. Terahertz Waves*, vol. 36, no. 6, pp. 542–555, 2015.

[23] B. Bowden, J. A. Harrington, and O. Mitrofanov, "Fabrication of terahertz hollow-glass metallic waveguides with inner dielectric coatings," *J. Appl. Phys.*, vol. 104, no. 9, 2008.

[24] J. Campion *et al.*, "Toward Industrial Exploitation of THz Frequencies: Integration of SiGe MMICs in Silicon-Micromachined Waveguide Systems," *IEEE Trans. Terahertz Sci. Technol.*, vol. 9, no. 6, pp. 624–636, 2019.

[25] H. Zhan, R. Mendis, and D. M. Mittleman, "Terahertz energy confinement in finite-width parallel-plate waveguides," *Int. Symp. Photoelectronic Detect. Imaging*, vol. 7385, no. 001, p. 73851K, 2009.

[26] L.-J. Chen, H.-W. Chen, T.-F. Kao, J.-Y. Lu, and C.-K. Sun, "Low-loss subwavelength plastic fiber for terahertz waveguiding," *Opt. Lett.*, vol. 31, no. 3, p. 308, 2006.

[27] M. Y. Frankel, S. Gupta, J. A. Valdmanis, and G. A. Mourou, "Terahertz Attenuation and Dispersion Characteristics of Coplanar Transmission Lines," *IEEE Trans. Microw. Theory Tech.*, vol. 39, no. 6, pp. 910–916, 1991.

[28] D. R. Grischkowsky, "Optoelectronic characterization of transmission lines and waveguides by terahertz time-domain spectroscopy," *IEEE J. Sel. Top. Quantum Electron.*, vol. 6, no. 6, pp. 1122–1135, 2000.

[29] X. Yu, M. Sugeta, Y. Yamagami, M. Fujita, and T. Nagatsuma, "Simultaneous low-loss and low-dispersion in a photonic-crystal waveguide for terahertz communications," *Appl. Phys. Express*, vol. 12, no. 1, 2019.

[30] K. Tsuruda, T. Ishigaki, A. Suminokura, R. Kakimi, M. Fujita, and T. Nagatsuma, "Ultralow-loss photonic-crystal waveguides for gigabit terahertz-wave communications," *IEEE Int. Topical Meeting Microw. Photonics (MWP)*, pp. 9–12, 2013.

[31] K. Tsuruda, M. Fujita, and T. Nagatsuma, "Extremely low-loss terahertz waveguide based on silicon photonic-crystal slab," *Opt. Express*, vol. 23, no. 25, p. 31977, 2015.

[32] J. C. Knight, T. A. Birks, P. St. J. Russell, and D. M. Atkin, "All-silica single-mode optical fiber with photonic crystal cladding: errata," *Opt. Lett.*, vol. 22, no. 7, p. 484, 1997.

[33] A. Argyros, "Microstructures in Polymer Fibres for Optical Fibres, THz Waveguides, and Fibre-Based Metamaterials," *ISRN Opt.*, pp. 1–22, 2013.

[34] A. Patrovsky and K. Wu, "Substrate Integrated Image Guide (SIIG) - A planar dielectric waveguide technology for millimeter-wave applications," *IEEE Trans. Microw. Theory Tech.*, vol. 54, no. 6, pp. 2872–2879, 2006.

[35] N. Ranjkesh, M. Basha, A. Taeb, and S. Safavi-Naeini, "Silicon-on-glass dielectric waveguide-Part II: For THz applications," *IEEE Trans. Terahertz Sci. Technol.*, vol. 5, no. 2, pp. 280–287, 2015.

[36] H.-M. Heiliger *et al.*, "Low-dispersion thin-film microstrip lines with cyclotene (benzocyclobutene) as dielectric medium," *Appl. Phys. Lett.*, vol. 70, no. 17, pp. 2233–2235, 1997.

[37] Y. Y. Wang, N. V. Wheeler, F. Couny, P. J. Roberts, and F. Benabid, “Low loss broadband transmission in hypocycloid-core Kagome hollow-core photonic crystal fiber,” *Opt. Lett.*, vol. 36, no. 5, p. 669, 2011.

[38] N. Ranjkesh, M. Basha, A. Taeb and S. Safavi-Naeini, "Silicon-on-Glass Dielectric Waveguide—Part II: For THz Applications," *IEEE Trans. Terahertz Sci. Technol.*, vol. 5, no. 2, pp. 280-287, 2015.

[39] L. Shen, Z. Ye, S. He, and S. He, “Design of two-dimensional photonic crystals with large absolute band gaps using a genetic algorithm,” *Phys. Rev. B Condens. Matter Mater Phys.*, vol. 68, no. 11, pp. 1–5, 2003.

[40] F. Meng, X. Huang, and B. Jia, “Bi-directional evolutionary optimization for photonic band gap structures,” *J. Comput. Phys.*, vol. 302, pp. 393–404, 2015.

[41] C. Elachi and C. Yeh, “Periodic structures in integrated optics,” *J. Appl. Phys.*, vol. 44, no. 7, pp. 3146–3152, 1973.

[42] E. Yablonovitch, “Inhibited Spontaneous Emission in Solid-State Physics and Electronics,” *Phys. Rev. Lett.*, vol. 58, no. 20, pp. 2059–2062, 1987.

[43] S. John, “Strong localization of photons in certain disordered dielectric superlattices,” *Phys. Rev. Lett.*, vol. 58, no. 23, pp. 2486–2489, 1987.

[44] S. Noda, A. Chutinan, and M. Imada, “Trapping and emission of photons by a single defect in a photonic bandgap structure,” *Nature*, vol. 407, no. 6804, pp. 608–610, 2000.

[45] M. Fujita, S. Takahashi, Y. Tanaka, T. Asano, and S. Noda, “Applied physics: Simultaneous inhibition and redistribution of spontaneous light emission in photonic crystals,” *Science (1979)*, vol. 308, no. 5726, pp. 1296–1298, 2005.

[46] R. Kakimi, M. Fujita, M. Nagai, M. Ashida, and T. Nagatsuma, “Capture of a terahertz wave in a photonic-crystal slab,” *Nat. Photonics*, vol. 8, no. 8, pp. 657–663, 2014.

[47] T. Baba, N. Fukaya, and J. Yonekura, “Observation of light propagation in photonic crystal optical waveguides with bends,” *Electron. Lett.*, vol. 35, no. 8, pp. 654–655.

[48] A. Chutinan and S. Noda, “Waveguides and waveguide bends in two-dimensional photonic crystal slabs,” *Phys. Rev. B*, vol. 62, no. 7, pp. 4488–4492, 2000.

[49] S. G. Johnson, P. R. Villeneuve, S. Fan, and J. D. Joannopoulos, “Linear waveguides in photonic-crystal slabs,” *Phys. Rev. B Condens. Matter Mater Phys.*, vol. 62, no. 12, pp. 8212–8222, 2000.

[50] M. Lončar, J. Vučković, and A. Scherer, “Methods for controlling positions of guided modes of photonic-crystal waveguides,” *J. Op. Soc. Am. B*, vol. 18, no. 9, p. 1362, 2001.

[51] H. Kurt and D. S. Citrin, “Photonic crystals for biochemical sensing in the terahertz region,” *Appl. Phys. Lett.*, vol. 87, no. 4, pp. 1–4, 2005, doi: 10.1063/1.1999861.

[52] T. Hasek, R. Wilk, H. Kurt, D. Citrin, and M. Koch, “Sub-terahertz 2D photonic crystal waveguides for fluid sensing applications,” *Int. Conf. Infrared Milli.*, p. 239, 2006, doi: 10.1109/ICIMW.2006.368447.

[53] T. Hasek, H. Kurt, D. S. Citrin, and M. Koch, “Photonic crystals for fluid sensing in the subterahertz range,” *Appl. Phys. Lett.*, vol. 89, no. 17, pp. 87–90, 2006.

[54] R. Menais and D. Grischkowsky, “THz interconnect with low-loss and low-group velocity dispersion,” *IEEE Microwave and Wireless Compon. Lett.*, vol. 11, no. 11, pp. 444–446, 2001.

[55] L. Jiusheng and Z. Xiaoli, “Terahertz waveguides based on photonic crystal,” *Optics InfoBase Conf. Papers*, vol. 211, pp. 4–5, 2009.

[56] K. Tsuruda, M. Fujita, and T. Nagatsuma, “Extremely low-loss terahertz waveguide based on silicon photonic-crystal slab,” *Opt. Express*, vol. 23, no. 25, p. 31977, 2015.
[57] K. Tsuruda, T. Ishigaki, A. Suminokura, R. Kakimi, M. Fujita, and T. Nagatsuma, “Ultralow-loss photonic-crystal waveguides for gigabit terahertz-wave communications,” *IEEE Int. Topical Meeting Microw. Photonics (MWP),* pp. 9–12, 2013.
[58] W. J. Otter *et al.*, “Terahertz Photonic Crystal Technology,” Workshop on THz, Saint Petersburg 2015, pp. 3–4, 2015.
[59] W. J. Otter, S. M. Hanham, N. M. Ridler, G. Marino, N. Klein, and S. Lucyszyn, “100 GHz ultra-high Q-factor photonic crystal resonators,” *Sens. Actuators A Phys.*, vol. 217, pp. 151–159, 2014.
[60] S. M. Hanham, C. Watts, W. J. Otter, S. Lucyszyn, and N. Klein, “Dielectric measurements of nanoliter liquids with a photonic crystal resonator at terahertz frequencies,” *Appl. Phys. Lett.*, vol. 107, no. 3. 2015.
[61] S. M. Hanham, M. M. Ahmad, S. Lucyszyn, and N. Klein, “LED-Switchable High-Q Packaged THz Microbeam Resonators,” *IEEE Trans. Terahertz Sci. Technol.*, vol. 7, no. 2, pp. 199–208, 2017.
[62] K. Tsuruda, K. Okamoto, S. Diebold, S. Hisatake, M. Fujita, and T. Nagatsuma, “Terahertz sensing based on photonic crystal cavity and resonant tunneling diode,” *Progress Electromag. Res. Symp.,* pp. 3922–3926, 2016.
[63] K. Okamoto, K. Tsuruda, S. Diebold, S. Hisatake, M. Fujita, and T. Nagatsuma, “Terahertz Sensor Using Photonic Crystal Cavity and Resonant Tunneling Diodes,” *J. Infrared. Millim. Terahertz Waves*, vol. 38, no. 9, pp. 1085–1097, 2017.
[64] S. Lucyszyn and Y. Zhou, “Characterising room temperature THz metal shielding using the engineering approach,” *Progress Electromag. Res.*, vol. 103, pp. 17–31, 2010.
[65] Y. Zhou and S. Lucyszyn, “Modelling of reconfigurable terahertz integrated architecture (Retina) siw structures,” *Prog. Electromag. Res.*, vol. 105, pp. 71–92, 2010.
[66] W. Gao, X. Yu, M. Fujita, T. Nagatsuma, C. Fumeaux, and W. Withayachumnankul, “Effective-medium-cladded dielectric waveguides for terahertz waves,” *Opt. Express*, vol. 27, no. 26, p. 38721, 2019.
[67] P. Cheben, R. Halir, J. H. Schmid, H. A. Atwater, and D. R. Smith, “Subwavelength integrated photonics,” *Nature*, vol. 560, no. 7720, pp. 565–572, 2018.
[68] H. Mosallaei and Y. Rahmat-Samii, “Photonic band-gap (PBG) versus effective refractive index: a case study of dielectric nanocavities,” *IEEE Antennas and Propag. Soc. Int. Symp.*, vol. 1, pp. 338–341, 2000.
[69] A. v. Subashiev and S. Luryi, “Modal control in semiconductor optical waveguides with uniaxially patterned layers,” *J. Lightwave Technol.*, vol. 24, no. 3, pp. 1513–1522, 2006.
[70] W. Gao, W. S. L. Lee, C. Fumeaux, and W. Withayachumnankul, “Effective-medium-clad Bragg grating filters,” *APL Photonics*, vol. 6, no. 7, pp. 1–9, 2021.
[71] D. Headland, W. Withayachumnankul, R. Yamada, M. Fujita, and T. Nagatsuma, “Terahertz multi-beam antenna using photonic crystal waveguide and Luneburg lens,” *APL Photonics*, vol. 3, no. 12, 2018.
[72] D. Headland, M. Fujita, and T. Nagatsuma, “Half-Maxwell fisheye lens with photonic crystal waveguide for the integration of terahertz optics,” *Opt. Express.*, vol. 28, no. 2, p. 2366, 2020.

[73] D. Headland, A. K. Klein, M. Fujita, and T. Nagatsuma, “Dielectric slot-coupled half-Maxwell fisheye lens as octave-bandwidth beam expander for terahertz-range applications,” *APL Photonics*, vol. 6, no. 9, 2021.

[74] R. A. S. D. Koala, D. Headland, Y. Yamagami, F. Masayuki, and T. Nagatsuma, “Broadband Terahertz Dielectric Rod Antenna Array with Integrated Half-Maxwell Fisheye Lens,” *Int. Topical Meeting Microw. Photonics (MWP)*, pp. 54–57, 2020.

[75] H. T. Zhu, Q. Xue, J. N. Hui, and S. W. Pang, “Design, Fabrication, and Measurement of the Low-Loss SOI-Based Dielectric Microstrip Line and its Components,” *IEEE Trans. Terahertz Sci. Technol.*, vol. 6, no. 5, pp. 696–705, 2016.

[76] T. Sagisaka *et al.*, “Integrated Terahertz Optics with Effective Medium for 600-GHz-band Imaging,” *Int. Topical Meeting Microw. Photonics (MWP)*, pp. 62–65, 2020.

[77] L. Yi *et al.*, “Towards Practical Terahertz Imaging System with Compact Continuous Wave Transceiver,” *J. Lightwave Technol.*, vol. 39, no. 24, pp. 7850–7861, 2021.

[78] D. Headland, W. Withayachumnankul, X. Yu, M. Fujita, and T. Nagatsuma, “Unclad Microphotonics for Terahertz Waveguides and Systems,” *J. Lightwave Technol.*, vol. 38, no. 24, pp. 6853–6862, 2020.

[79] H. Amarloo, N. Ranjkesh, and S. A. Safavi-Naeini, “Terahertz Silicon-BCB-Quartz Dielectric Waveguide: An Efficient Platform for Compact THz Systems,” *IEEE Trans. Terahertz Sci. Technol.*, vol. 8, no. 2, pp. 201–208, 2018.

[80] H. Amarloo and S. Safavi-Naeini, “Terahertz Line Defect Waveguide Based on Silicon-on-Glass Technology,” *IEEE Trans. Terahertz Sci. Technol.*, vol. 7, no. 4, pp. 433–439, 2017.

[81] N. Ranjkesh, S. Gigoyan, H. Amarloo, M. Basha, and S. Safavi-Naeini, “Broadband single-mode THz suspended silicon-on-glass waveguide,” *IEEE Microw. Wireless Compon. Lett.*, vol. 28, no. 3, pp. 185–187, 2018.

[82] W. Withayachumnankul, R. Yamada, M. Fujita, and T. Nagatsuma, “All-dielectric rod antenna array for terahertz communications,” *APL Photonics*, vol. 3, no. 5, 2018.

[83] N. Ranjkesh, M. Basha, A. Taeb, and S. Safavi-Naeini, “Silicon-on-glass dielectric waveguide-Part II: For THz applications,” *IEEE Trans. Terahertz Sci. Technol.*, vol. 5, no. 2, pp. 280–287, 2015.

[84] E. Akiki *et al.*, “High-Q THz Photonic Crystal Cavity on a Low-Loss Suspended Silicon Platform,” *IEEE Trans. Terahertz Sci. Technol.*, vol. 11, no. 1, pp. 42–53, 2021.

[85] Y. Yang *et al.*, “Terahertz topological photonics for on-chip communication,” *Nat. Photonics*, no. 14, pp. 446-451, 2020.

[86] D. Headland, X. Yu, M. Fujita, and T. Nagatsuma, “Near-field vertical coupling between terahertz photonic crystal waveguides,” *URSI Asia-Pacific Radio Sci. Conf., AP-RASC 2019*, vol. 6, no. 8, 2019.

[87] E. Akiki *et al.*, “High-Q THz Photonic Crystal Cavity on a Low-Loss Suspended Silicon Platform,” *IEEE Trans. Terahertz Sci. Technol.*, vol. 11, no. 1, pp. 42–53, 2021.

[88] N. Shibata, Y. Uemura, Y. Kawamoto, L. Yi, M. Fujita and T. Nagatsuma, "600-GHz-band Silicon Dielectric Waveguide Module," *Int. Conf. Infrared Milli. Terahertz Waves (IRMMW-THz)*, pp. 1-2, 2021.

[89] P. De Maagt, P. H. Bolivar, and C. Mann, “Terahertz Science, Engineering and Systems-from Space to Earth Applications,” *Encyclopedia of RF and Microwave Engineering*, vol. 2, no. 7, Hoboken: John Wiley & Sons, Inc., pp. 3–10, 2005.

[90] P. H. Siegel, "Terahertz technology in biology and medicine," *IEEE Trans Microw. Theory Tech.*, vol. 52, no. 10, pp. 2438–2447, 2004.
[91] J. C. Dickinson *et al.*, "Terahertz imaging of subjects with concealed weapons," *Terahertz Mil. Sec. Appl. IV*, vol. 6212, no. 978, p. 62120Q, 2006.
[92] S. Diebold *et al.*, "High-speed error-free wireless data transmission using a terahertz resonant tunnelling diode transmitter and receiver," *Electron. Lett.*, vol. 52, no. 24, pp. 1999–2001, 2016.
[93] S.-H. Yang and M. Jarrahi, "Navigating Terahertz Spectrum via Photomixing," *Opt. Photonics News*, vol. 31, no. 7, p. 36, 2020.
[94] Y. Kawamoto et al., "Integrated Resonant Tunneling Diode with Rectangular Waveguide I/O using Photonic Crystal Interface," *Int. Conf. Infrared Milli. Terahertz Waves (IRMMW-THz)*, pp. 1-2, 2021.
[95] D. Headland, M. Fujita, and T. Nagatsuma, "Bragg-mirror suppression for enhanced bandwidth in terahertz photonic crystal waveguides," *IEEE J. Sel. Top. Quantum Electron.*, vol. 26, no. 2, pp. 1–9, 2020.
[96] V. Toccafondo et al., "Single-strand DNA detection using a planar photonic-crystal-waveguide-based sensor," *Opt. Lett.*, vol. 35, no. 21, p. 3673, 2010.
[97] H. Quast and T. Löffler, "3D-Terahertz-tomography for material inspection and security," *Int. Conf. Infrared Milli. Terahertz Waves (IRMMW-THz)*, pp. 1-2, 2009.
[98] W. S. L. Lee et al., "Broadband Terahertz Circular-Polarization Beam Splitter," *Adv. Opt. Mater*, vol. 6, no. 3, pp. 1–7, 2018.
[99] J. Ren, Z. Jiang, P. Fay, J. L. Hesler, C. Y. E. Tong, and L. Liu, "High-Performance WR-4.3 Optically Controlled Variable Attenuator with 60-dB Range," *IEEE Microw. Wireless Compon. Lett.*, vol. 28, no. 6, pp. 512–514, 2018.
[100] R. Koala, R. Maru, K. Iyoda, L. Yi, M. Fujita, and T. Nagatsuma, "Ultra-Low-Loss and Broadband All-Silicon Dielectric," *Photonics*, vol. 9, no. 8:515, 2022.
[101] P. Hillger, J. Grzyb, R. Jain, and U. R. Pfeiffer, "Terahertz Imaging and Sensing Applications With Silicon-Based Technologies," *IEEE Trans. Terahertz Sci. Technol.*, vol. 9, no. 1, pp. 1–19, 2019.
[102] C. Am Weg, W. von Spiegel, R. Henneberger, R. Zimmermann, T. Loeffler, and H. G. Roskos, "Fast active THz cameras with ranging capabilities," *J. Infrared Millim. Terahertz Waves*, vol. 30, no. 12, pp. 1281–1296, 2009.
[103] C. W. Berry and M. Jarrahi, "Principles of impedance matching in photoconductive antennas," *J. Infrared Millim. Terahertz Waves*, vol. 33, no. 12, pp. 1182–1189, 2012.
[104] C. W. Berry and M. Jarrahi, "Plasmonic photoconductive antennas for high power terahertz generation," *IEEE Antennas and Propagation Society, AP-S Int. Symp.*, 2012.
[105] W. Gao et al., "Characteristics of Effective-Medium-Clad Dielectric Waveguides," *IEEE Trans. Terahertz Sci. Technol.*, vol. 11, no. 1, pp. 28–41, Jan. 2021.
[106] L. Chrostowski and M. Hochberg, Silicon Photonics Design. Cambridge University Press, 2015.
[107] T. Nagatsuma, K. Kato, and J. Hesler, "Enabling technologies for real-time 50-Gbit/s wireless transmission at 300 GHz," *Int. Conf. Nanoscale Computing Commun. (ACM NANOCOM)*, 2015.
[108] T. Nagatsuma and G. Carpintero, "Recent progress and future prospect of photonics-enabled terahertz communications research," *IEICE Trans. Electron.*, vol. E98C, no. 12, pp. 1060–1070, 2015.

[109] Y. Dong, L. Chen, and X. Bao, "Time-division multiplexing-based BOTDA over 100km sensing length," *Opt. Lett.*, vol. 36, no. 2, p. 277, 2011.
[110] F. Ren et al., "Three-mode mode-division-multiplexing passive optical network over 12-km low mode-crosstalk FMF using all-fiber mode MUX/DEMUX," *Opt. Commun.*, vol. 383, pp. 525–530, 2017.
[111] N. Wada and K. I. Kitayama, "10 Gb/s optical code division multiplexing using 8-chip optical bipolar code and coherent detection," *J. Lightwave Technol.*, vol. 17, no. 10, pp. 1758–1765, 1999.
[112] K. Kitayama, "Code division multiplexing lightwave networks based upon optical code conversion," *IEEE J. Sel. Areas in Commun.*, vol. 16, no. 7, pp. 1309–1319, 1998.
[113] H. Harada, K. Sato, and M. Fujise, "A Radio-on-Fiber Based Millimeter-Wave Road-Vehicle Communication System by a Code Division Multiplexing Radio Transmission Scheme," *IEEE Trans. Intell. Transp. Sys.*, vol. 2, no. 4, pp. 165–179, 2001.
[114] R. J. Chan and J. C. Guo, "Analytical modeling of proximity and skin effects for millimeter-wave inductors simulation and design in nano Si CMOS," *IEEE MTT-S Int. Microw. Symp.*, 2014.
[115] N. Shibata, Y. Uemura, Y. Kawamoto, L. Yi, M. Fujita, and T. Nagatsuma, "Silicon Dielectric Diplexer Module for 600-GHz-Band Frequency-Division Multiplexing Wireless Communication," *IEEE Trans. Terahertz Sci. Technol*., vol. 12, no. 4, pp. 334–344, 2022.
[116] A. Kumar, M. Gupta, P. Pitchappa, N. Wang, M. Fujita, and R. Singh, "Terahertz topological photonic integrated circuits for 6G and beyond: A Perspective," *J. Appl. Phys*., vol. 132, no. 14, 2022.
[117] A. v. Krishnamoorthy et al., "Progress in low-power switched optical interconnects," *IEEE J. Sel. Top. Quantum Electron.*, vol. 17, no. 2, pp. 357–376, 2011.
[118] Q. J. Gu, "THz interconnect: The last centimeter communication," *IEEE Commun. Mag.*, vol. 53, no. 4, pp. 206–215, 2015.
[119] X. Yu et al., "Terahertz fibre transmission link using resonant tunnelling diodes integrated with photonic-crystal waveguides," *Electron. Lett*., vol. 55, no. 7, pp. 398–400.
[120] J. Vaes, K. Dens, G. Ducournau, and P. Reynaert, "Plastic Microwave Fibers at Millimeter-wave and THz Frequencies as a Low Cost Data Link," IEEE *MTT-S Int. Microw. Symp.*, vol. 2021, pp. 589–591, 2021.
[121] T. Ito, Y. Matsuura, M. Miyagi, H. Minamide, and H. Ito, "Flexible terahertz fiber optics with low bend-induced losses," *J. Opt. Soc. Am. B*, vol. 24, no. 5, p. 1230, 2007.
[122] M. Yata, M. Fujita, and T. Nagatsuma, "Photonic-crystal diplexers for terahertz-wave applications," *Opt. Express*, vol. 24, no. 7, p. 7835, 2016.
[123] D. M. Pozar, Microwave Engineering, 4th Ed., Wiley, 2011.
[124] G. Xu and M. Skorobogatiy, "Wired THz Communications," *J. Infrared Milli. Terahertz Waves*, vol. 43, pp. 728-778, 2022.
[125] B. J. Mangan et al., "First Demonstration of Hollow-Core Fiber for Intra Data Center Low Latency Connectivity with a Commercial 100Gb/s Interface," *Opt. Fiber Commun. Conf.*, 2015, p. M3D.4.
[126] X. Yu et al., "Terahertz fibre transmission link using resonant tunnelling diodes integrated with photonic-crystal waveguides," *Electron. Lett.*, vol. 55, no. 7, pp. 398–400, 2019.
[127] W. Y. Ali-Ahmad, W. L. Bishop, T. W. Crowe, and G. M. Rebeiz, "An 86-106 GHz quasi-integrated low noise Schottky receiver," *IEEE Trans. Microw. Theory Tech.*, vol. 41, no. 4, pp. 558–564, 1993.
[128] S. S. Gearhart, C. C. Ling, and G. M. Rebeiz, "Integrated millimeter-wave corner-cube antennas," *IEEE Trans. Antennas Propag.*, vol. 39, no. 7, pp. 1000–1006, 1991.

[129] D. F. Filipovic, W. Y. Ali-Ahmad, and G. M. Rebeiz, "Millimeter-wave double-dipole antennas for high-gain integrated reflector illumination," *IEEE Trans. Microw. Theory Tech.*, vol. 40, no. 5, pp. 962–967, 1992.
[130] G. M. Rebeiz, "Millimeter-wave and terahertz integrated circuit antennas," *IEEE*, vol. 80, no. 11, pp. 1748–1770, 1992.
[131] Online. Available at: www.newport.com (Accessed: January 2023).
[132] Q. Huang, Y. Zhang, J. Tang, and J. Sun, "The Design, Fabrication and Characterization of Grating Couplers for SiGe Photonic Integration Employing a Reflective Back Mirror," *Nanomaterials*, vol. 12, no. 21, p. 3789, 2022.
[133] B. Chmielak et al., "High-efficiency grating coupler for an ultralow-loss Si 3 N 4 -based platform ," *Opt. Lett.*, vol. 47, no. 10, p. 2498, 2022.
[134] H. Gehring et al., "Low-loss fiber-to-chip couplers with ultrawide optical bandwidth," *APL Photonics*, vol. 4, 010801 (2019).
[135] Güçlü, A. F. Özdemir, A. Karabulut, A. Kökce, and Altındal, "Investigation of temperature dependent negative capacitance in the forward bias C-V characteristics of (Au/Ti)/Al2O3/n-GaAs Schottky barrier diodes (SBDs*)," Mater Sci. Semicond. Process*, vol. 89, pp. 26–31, 2019.
[136] W. Q. Malik, D. J. Edwards, and C. J. Stevens, "Frequency-dependent pathloss in the ultrawideband indoor channel," *IEEE Int. Conf. Commun.*, 2006, vol. 12, pp. 5546–5551, 2006.
[137] G. A. Siles, J. M. Riera, and P. García-Del-Pino, "Atmospheric attenuation in wireless communication systems at millimeter and THz frequencies [Wireless Corner]," *IEEE Antennas Propag. Mag.*, vol. 57, no. 1, pp. 48–61, 2015.
[138] M. Jacob, S. Priebe, R. Dickhoff, T. Kleine-Ostmann, T. Schrader, and T. Kürner, "Diffraction in mm and sub-mm wave indoor propagation channels," *IEEE Trans. Microw. Theory Tech.*, vol. 60, no. 3 PART 2, pp. 833–844, 2012.
[139] C. Jansen, R. Piesiewicz, D. Mittleman, T. Kürner, and M. Koch, "The impact of reflections from stratified building materials on the wave propagation in future indoor terahertz communication systems," *IEEE Trans. Antennas Propag.*, vol. 56, no. 5, pp. 1413–1419, 2008.
[140] J. Kokkoniemi, P. Rintanen, J. Lehtomäki, and M. Juntti, "Diffraction effects in terahertz band - Measurements and analysis," *IEEE Global Commun. Conf. (GLOBECOM)*, 2016.
[141] C. Jansen et al., "Diffuse scattering from rough surfaces in THz communication channels," *IEEE Trans. Terahertz Sci. Technol.*, vol. 1, no. 2, pp. 462–472, 2011.
[142] H. Wu et al., "A 60GHz on-chip RF-Interconnect with λ/4 coupler for 5Gbps bi-directional communication and multi-drop arbitration," *Custom Integrated Circuits Conf.*, 2012.
[143] J. D. Park, S. Kang, S. v. Thyagarajan, E. Alon, and A. M. Niknejad, "A 260 GHz fully integrated CMOS transceiver for wireless chip-to-chip communication," *IEEE Symposium on VLSI Circuits*, pp. 48–49, 2012.
[144] W. H. Chen et al., "A 6-Gb/s wireless inter-chip data link using 43-GHz transceivers and bond-wire antennas," *IEEE J. Solid-State Circuits*, vol. 44, no. 10, pp. 2711–2721, 2009.
[145] C. W. Byeon, C. H. Yoon, and C. S. Park, "A 67-mW 10.7-Gb/s 60-GHz OOK CMOS transceiver for short-range wireless communications," *IEEE Trans. Microw. Theory Tech.*, vol. 61, no. 9, pp. 3391–3401, 2013.
[146] F. Zhu et al., "A low-power low-cost 45-GHz ook transceiver system in 90-nm CMOS for multi-Gb/s transmission," *IEEE Trans. Microw. Theory Tech.*, vol. 62, no. 9, pp. 2105–2117, 2014.
[147] S. Mishra, N. K. Chaudhary, and K. Singh, "Overview of Optical Interconnect Technology," 2013, Available: http://arxiv.org/abs/1303.3954.

[148] F. E. Doany et al., “Terabit/Sec VCSEL-based 48-channel optical module based on holey CMOS transceiver IC,” *J. Lightwave Technol.*, vol. 31, no. 4, pp. 672–680, 2013.
[149] M. A. Green, J. Zhao, A. Wang, P. J. Reece, and M. Gal, “Efficient silicon light-emitting diodes,” *Nature*, vol. 412, no. 6849, pp. 805–808, 2001.
[150] X. Yu, “Terahertz Integrated Circuits Based on Photonic-crystal Waveguide Platform,” Doctoral dissertation, Osaka University, 2020.
[151] X. Yu et al., “Direct terahertz communications with wireless and fiber links,” *Int. Conf. Infrared Mill. Terahertz Waves (IRMMW-THz)*, vol. 2019, pp. 3–4, 2019.
[152] X. Yu et al., “Terahertz fibre transmission link using resonant tunnelling diodes integrated with photonic-crystal waveguides,” *Electron. Lett.*, vol. 55, no. 7, pp. 398–400, 2019.
[153] R. Koala, D. Headland, X. Yu, Y. Nishida, M. Fujita, and T. Nagatsuma, “Terahertz RTD Chip Backside-coupled to Photonic-crystal Waveguide,” *Int. Conference Infrared Milli. Terahertz Waves (IRMMW-THz),* pp. 1–2, 2021.
[154] Y. Horst et al., “Transparent Optical-THz-Optical Link at 240/192 Gbit/s over 5/115 m Enabled by Plasmonics,” *J. Lightwave Technol.*, vol. 40, no. 6, pp. 1690–1697, 2022.
[155] X. Li et al., “1-Tb/s Millimeter-Wave Signal Wireless Delivery at D-Band,” *J. Lightwave Technol.*, vol. 37, no. 1, pp. 196–204, 2019.
[156] S. Koenig et al., “Wireless sub-THz communication system with high data rate,” *Nat. Photonics*, vol. 7, no. 12, pp. 977–981, 2013.
[157] X. Pang et al., “260 Gbit/s photonic-wireless link in the THz band,” *IEEE Photonics Conference (IPC)*, pp. 1-2, 2017.
[158] S. Jia et al., “2 × 300 Gbit/s Line Rate PS-64QAM-OFDM THz Photonic-Wireless Transmission,” *J. Lightwave Technol.*, vol. 38, no. 17, pp. 4715–4721, 2020.
[159] T. P. McKenna, J. A. Nanzer, and T. R. Clark, “Photonic downconverting receiver using optical phase modulation,” *IEEE MTT-S International Microwave Symposium*, 2014.
[160] P. T. Dat et al., "Transparent Fiber–Radio–Fiber Bridge at 101 GHz using Optical Modulator and Direct Photonic Down-Conversion," *Opt. Fiber Commun. Conf. Exhib. (OFC)*, pp. 1-3, 2021.
[161] C. Yang, X. Li, J. Xiao, N. Chi, and J. Yu, “Fiber-wireless integration for 80 Gbps polarization division multiplexing -16QAM signal transmission at W-band without rf down conversion,” *Microw. Opt. Technol. Lett*., vol. 57, no. 1, pp. 9–13, 2015.
[162] A. J. Seeds, H. Shams, M. J. Fice, and C. C. Renaud, “TeraHertz photonics for wireless communications,” *J. Lightwave Technol*., vol. 33, no. 3, pp. 579–587, 2015.
[163] Y. Salamin et al., “Direct Conversion of Free Space Millimeter Waves to Optical Domain by Plasmonic Modulator Antenna,” *Nano Lett.*, vol. 15, no. 12, pp. 8342–8346, 2015.
[164] S. Choi, “Efficient Antennas for Terahertz and Optical Frequencies,” Doctoral dissertation, University of Michigan, 2014.
[165] M. Shiraishi, S. Suzuki, and M. Asada, “High-power operation of terahertz oscillators with resonant tunneling diodes using offset-fed slot antennas and array configuration,” *Int. Conf. Infrared Milli. Terahertz Waves (IRMMW-THz),* pp. 1-2, 2012.
[166] K. Kasagi, S. Suzuki, and M. Asada, “Large-scale array of resonant-tunneling-diode terahertz oscillators for high output power at 1 THz,” *J. Appl. Phys.*, vol. 125, no. 15, 2019.
[167] Y. Koyama et al., “A High-Power Terahertz Source Over 10 mW at 0.45 THz Using an Active Antenna Array With Integrated Patch Antennas and Resonant-Tunneling Diodes,” *IEEE Trans. Terahertz Sci. Technol*., vol. 12, no. 5, pp. 510–519, 2022.
[168] M. Fujishima, M. Motoyoshi, K. Katayama, K. Takano, N. Ono, and R. Fujimoto, “98 mW 10 Gbps wireless transceiver chipset with d-band COMS circuits,” *IEEE J. Solid-State Circuits*, vol. 48, no. 10, pp. 2273–2284, 2013.

[169] Y. Chen et al., “A 25Gb/s hybrid integrated silicon photonic transceiver in 28nm CMOS and SOI,” *IEEE Int. Solid-State Circuits Conf.*, 2015, vol. 58, pp. 402–403.
[170] Online. Available at: www.aimphotonics.com (accessed: February 2023).
[171] Online. Available at: www.leti-cea.com (accessed: February 2023).
[172] Online. Available at www.imec-int.com (accessed: February 2023).
[173] X. Yu et al., “Orthogonally polarized terahertz wave imaging with real-time capability for food inspection,” *Asia-Pacific Microw. Conf, (APMC)*, pp. 1–3, 2015.
[174] H. Ito and T. Ishibashi, “InP/InGaAs Fermi-level managed barrier diode for broadband and low-noise terahertz-wave detection,” *Jpn. J. Appl. Phys*., vol. 56, no. 1, 2017.
[175] T. Shiode, T. Mukai, M. Kawamura, and T. Nagatsuma, “Giga-bit wireless communication at 300 GHz using resonant tunneling diode detector,” *Asia-Pacific Microw, Conf. (APMC)*, pp. 1122–1125, 2011.

Acknowledgements

I would like to express my profound gratitude to Professor Masayuki Fujita and Professor Tadao Nagatsuma, of the Graduate school of Engineering Science of Osaka university for being incredible mentors during my Ph.D. journey. You have allowed me to be part of an amazing team and conduct pioneering research, for which I will forever be grateful. You were a good shoulder for every failed experiment, and a listening ear when I was talking about my career aspirations, my dreams and hopes for the future. You have left an impact on me and helped me become a better scientist and a better version of myself. Thank you. I am very grateful to Professor Li Yi, for welcoming me in the group, and for the fruitful comments that made a big difference in the trajectory of so many of my experiments. Thank you for your kindness. I only wish we had gotten closer over the years.

I would like to express my gratitude to Professor Atsushi Sanada and Professor Takashi Mukaiyama, for reviewing this thesis, for the fruitful discussions, edits, and for helping me further hone my critical thinking. I am immensely grateful for your time, encouragement, and input. I am a better scientist thanks to you, and my thesis is a better scientific manuscript thanks to you.

I would like to offer a token of gratitude to Dr. Murakami at the Osaka research institute for supporting my research by providing timely manufacturing of my devices, but also welcoming me in their offices, and teaching me about their device fabrication process. I would also like to express my gratitude to Professor Yuji Matsuura at Tohoku University, for his time and constant support. Matsuura-Sensei, thank you very much for supplying the fibers I employed in my research, but also for all the fruitful discussions.

I am incredible grateful to Professor Safumi Suzuki of the Tokyo Institute of Technology for discussions on RTD work, but also for his advice on career and life. Suzuki-Sensei, I was always happy to meet you at conference venues. Thank you for the nice conversations, and for being a role model.

I would like to express my gratitude to my lab mates, particularly to Mr. Kei Iyoda. Kei, thank you for being a great friend and partner during my years at the information

photonics group. I admire your brilliance, but also your humility and kindness. I was inspired by you every time we worked together. I am sure the future holds nothing but great things for you. Thank you. To my dear fiend Weijie Gao, we started to work together at the end of my degree but in a short time, I have learned a lot from you, and we have grown very close. You gave me the best present on my 28th birthday. Thank you for being a great mentor and friend. I would also like to express my gratitude to the imaging team, specifically Ms. Ryoko Mizuno and Mr. Yosuke Koyabu for their help performing the imaging experiments. Your insights and contributions helped get good imaging results. Thank you. I am also grateful to Mr. Yuichiro Yamagami at ROHM, for his time and patience during my training period. Yamagami, thank you for being a great teacher and a friend. We have gotten closer for all the time we spent working on antenna transmission experiments, and you remain one of the few friends I have made during my time in Japan. Thank you. My additional thanks go to Mr. Naoki Nishigami, Mr. Shuya Iwamatsu and Mr. Yosuke Nishida at ROHM for teaching me about RTDs. I have learned a great deal on RTDs from design, simulation, wire bonding, to experiments from you. Thank you for your patience, and for your time.

Finally, I would like to express my immense gratitude to my support network including my friends and family. I could not have done it without you. You have been my biggest fans, and always supported me. You were there in my stressful times to listen to me and offer your encouragements. To my big sister Estelle Koala, you have been my number one cheerleader since I was little, and I couldn't thank you enough. To my father Jericho Koala, when I was five, I told you I wanted to be a singer and you said, "we'll see". Look how I turned out! From an early age, you ignited and fostered a fire in me, that has been a compass in my darkest times, and it is the best gift a father can make. I hope to do the same someday. To my mother Rose Kanyili, you gifted me your big heart. I owe it to you that I am a scientist who thinks with my heart. I found my life mission of using technology to improve the lives of the less fortunate thanks to you. Thank you!

Osaka, March 2023

Alex Koala

List of publications

Journal articles

[1] R. Koala, M. Fujita, and T. Nagatsuma, "Nanophotonics-inspired all-silicon waveguide platforms for terahertz integrated systems," *Nanophotonics*, vol. 11, no. 9, pp. 1741-1759, 2022. [**Published**]

[2] R. Koala, R. Maru, K. Iyoda, Y. Li, M. Fujita, and T. Nagatsuma, "Ultra-low-loss and broadband all-silicon dielectric waveguides for WR-1 band (0.75 – 1.1 THz)," *Photonics*, vol. 9, no. 8:515, 2022. [**Published**]

[3] R. Koala, K. Iyoda, Weijie Gao, Yuji Matsuura, M. Fujita, and T. Nagatsuma, "Terahertz fiber link using dielectric silicon waveguide interface," *Opt. Express*, vol. 31, no. 5, pp. 7351-7362, 2023. [**Published**]

[4] R. Koala, K. Iyoda, M. Fujita, and T. Nagatsuma, "Terahertz link with orthogonal polarization over silicon dielectric waveguide," *Electron. Lett.* [**Under review**]

[5] X. Yu, D. Headland, Y. Nishida, R. Koala, J. Kim, M. Fujita, and T. Nagatsuma, "Hybrid Integration Between Resonant Tunneling Diodes and Unclad Microphotonics Diplexer for Dual-Channel Coherent Terahertz Receiver," *J. sel. Top. Quantum Electron.*, vol 28, no. 3, pp.1-10, 2020. [**Published**]

Conference talks

[1] R. Koala, M. Fujita, and T. Nagatsuma, "Dual polarization operation in silicon terahertz diplexer," *Symp. Frontier Terahertz Technol. (FTT2022)*, Fukui, Japan, 2022 [**Poster presentation**]

[2] R. Koala, S. Norihiko, M. Fujita, and T. Nagatsuma, "WR-1 band packaged low-loss unclad silicon waveguide module," *Int. Conf. Infrared Milli. Terahertz Waves (IRRMW-THz)*, Delft, The Netherlands, 2022 [**Keynote**]

[3] R. Koala, D. Headland, X. Yu, Y. Nishida, M. Fujita, and T. Nagatsuma, "Terahertz RTD chip backside-coupled to Photonic-crystal waveguide," *Int. Conf. Infrared Milli. Terahertz Waves (IRRMW-THz)*, Chengdu, China, 2021 [**Keynote**]

[4] R. Koala, D. Headland, M. Fujita, and T. Nagatsuma, "Dish-antenna-integrated resonant tunneling diode module for terahertz wireless applications," *URSI-GASS*, Rome, Italy, 2021 [**Oral presentation**]

[5] R. Koala, D. Headland, M. Fujita, and T. Nagatsuma, "Broadband terahertz dielectric rod antenna array with integrated half-Maxwell fisheye lens," *Int. Topical Meeting Microw. Photonics (MWP)*, 2020 [**Oral presentation**]